Incorporation of mixed metal sulfides in a porous matrix for efficient water reduction

Joos, B.

Award date:
2015

Incorporation of mixed metal sulfides in a porous matrix for efficient water reduction

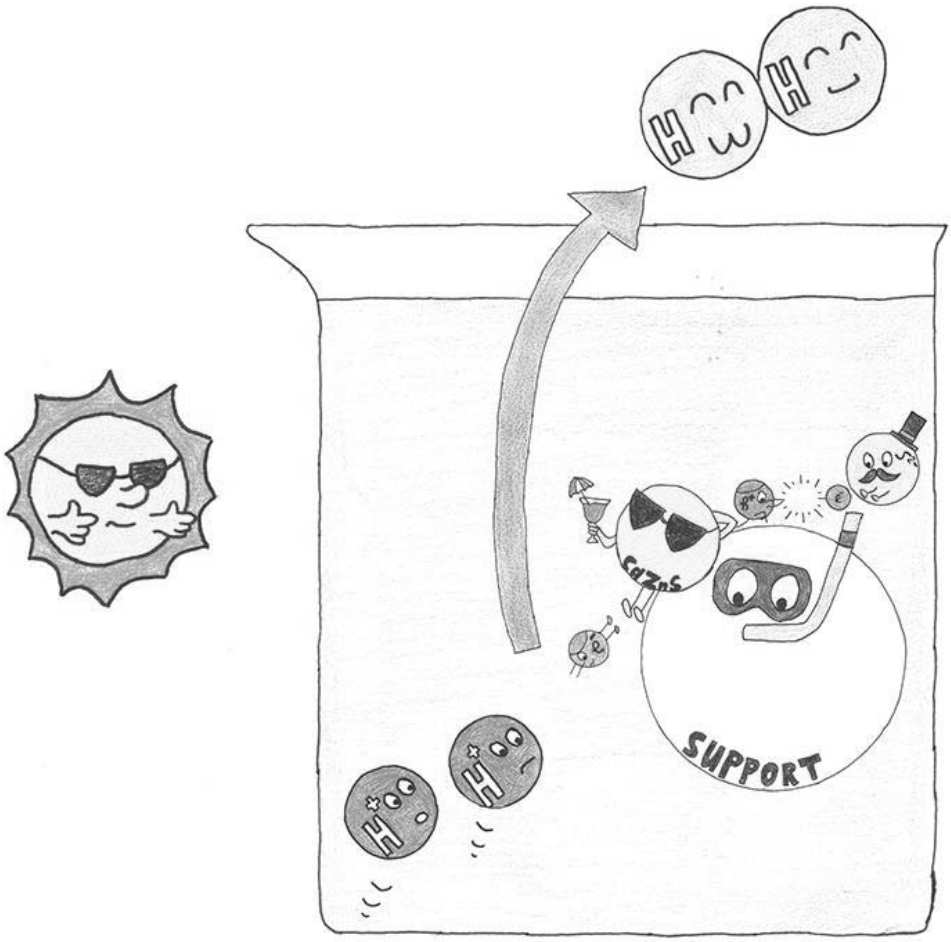

Master Thesis
Bjorn Joos BSc.
Department of Chemical Engineering and Chemistry
Eindhoven University of Technology
Supervisors: A. Litke, Dr. rer. nat. J.P. Hofmann, and Prof. Dr. E. J. M. Hensen

Abstract

In the present work we studied photocatalytic water reduction on the supported $Cd_{0.5}Zn_{0.5}S$. We found that the aggregation of the photocatalyst particles, which decreases its activity, can be addressed by anchoring them on a support. A comparison between a dielectric (SiO_2) and semiconducting (TiO_2) supports was done. The deposition of the Cd-Zn sulfide on the silica-based supports by co-precipitation increased the activity up to 93% in comparison with the unsupported sample. However the silica-based supports cannot sustain the harsh hydrothermal conditions required for the synthesis of highly active sulfides.

The hydrothermal synthesis route was used to load $Cd_{0.5}Zn_{0.5}S$ photocatalyst on the titania-based supports. Surprisingly, these composites were found to be less active than the unsupported photocatalyst. We suggest that the strong light scattering by the titania particles caused this loss of the activity. Platinization of the (un)supported sulfide enhanced the activity of the photocatalyst up to 8 times but the unsupported platinized sulfide was found to be the most active among all samples. This can be explained by the fact that no efficient transfer of the photogenerated electrons from the sulfide to the titania particles took place. This finding was opposite to numerous reports on the synergetic effect of the coupling of CdS and TiO_2 semiconductors. Although the reason of this controversy was unclear we assume that it might be a result of a mismatch of the energy levels of the conduction band of two semiconductors.

Table of Contents

Chapter 1: General introduction

1.1 Thesis outline

This thesis is focused on the use of a porous support to increase the photocatalytic activity of the $Cd_xZn_{1-x}S$ nanoparticles. The aim of the project is to improve and maintain dispersion of the nanoparticles of the photocatalyst by mean of porous supports. Anchoring of the nanoparticles on a support can circumvent the aggregation of the $Cd_xZn_{1-x}S$ suspensions and maintain high photocatalytic activity over long period of time. To achieve this goal we first selected model mesoporous silica (SiO_2) supports (i.e. SBA-15 and MCM-41). The use of these supports in photocatalytic water reduction has been previously reported in literature.[1-3] Then we used titania (TiO_2) supports – mesoporous TiO_2 beads and nanocrystalline Degussa P25 – as a more chemically stable material.[4-6] Later the $Cd_xZn_{1-x}S$@titania composites were loaded with platinum to further increase the photocatalytic activity.

A general background to the field of photocatalysis is given in chapter 1 while a literature study of the mixed metal sulfide is given in chapter 2 to provide the latest development and a more in-depth background to this thesis. Chapter 3 describes experimental details. This includes synthesis of the supports, their loading under hydrothermal conditions, co-precipitation and incipient wetness impregnation. Sample preparation for characterization, short summaries of the key principles of each technique and the parameters used during the measurements are also given in that chapter. The results of $Cd_xZn_{1-x}S$ loaded on silica supports are given and discussed in chapter 4. Analogously the results for the TiO_2 supports are given and discussed in chapter 5. Chapter 6 is devoted to the discussion of the most important findings of this thesis together with an outlook for future projects.

1.2 The energy problem

The modern civilization is based upon the use of fossil fuels to satisfy the energy demand. The energy content of fossil fuels is released by combustion and utilized for heating, transportation, or conversion into electricity (i.e. fossil fuel driven power plants). Besides the energy content, they are also vital feedstock for chemical industry and are used to produce drugs, fine chemicals, plastics, synthetic fibers, etc. Consumption of these finite resources has been rising during the last decades and is predicted to increase even further. After the energy crisis in 1973, society has acknowledged the risks posed by the dependence on fossil fuels. The global energy demand will continue to raise due to the fast growth of the human population and industrialization of the emerging economies (e.g. Brazil, China, and India). More than 85% of the global energy demand increase is predicted to originate from nations outside the Organization for Economic Cooperation and Development (non-OECD) from 2010 until 2040. OECD member states suffer from low population and economic growth, therefore a minor energy consumption increase is expected.[7] Estimates indicate an increase of the global energy demand by 56 % from 13.5 TW to 40.8 TW by 2050.[8] Currently, oil (33%), coal (30%) and natural gas (24%) supply 87 % of the global energy demand, see Figure 1.[9, 10] Nuclear, wind and hydropower mainly fill the remaining 13%. Solar energy contributes only a negligibly small 0.04%.[11]

The harvesting of the solar energy is key to the development of a sustainable economy as it is considered the only renewable energy source that could potentially satisfy the ever growing energy demand.[12] The Sun annually supplies a tremendous amount of energy to the Earth's surface, i.e. 3×10^{24} J, about ten thousand times the annual global energy consumption.[13] Hypothetically, covering 1% of the Earth's surface by photovoltaics could produce 105 TW of electrical energy

annually (assuming 10% efficiency). For comparison, some studies estimate the total potential output by wind power to be 2-4 TW, by hydropower 2-3 TW, by biomass 5-7 TW, and by geothermal energy 3-6 TW. [11] To reduce the pressure on the fossil fuels reserves and environment it is imperative to shift the energy production towards renewables like hydropower, wind power and solar energy. However, a major issue of the solar energy is that it has to be converted into another form for the effective use because it is inconvenient to utilize and impossible to store photons. The most well-established technology is the conversion of solar energy into electricity by use of photovoltaics. However electrical energy suffers from storage issues as well because up to date there are no efficient ways to store it. Solar energy can play an important role in the future if it can be harvested and stored into some energy carrier. The scientific community has been undertaking great efforts to develop both light harvesting materials and storage methods. Energy-dense fuels (e.g. hydrogen, methanol, formic acid) can be produced upon capturing solar light and act as storage media.[14-17] Therefore these energy carriers are referred to as solar fuels hereafter.

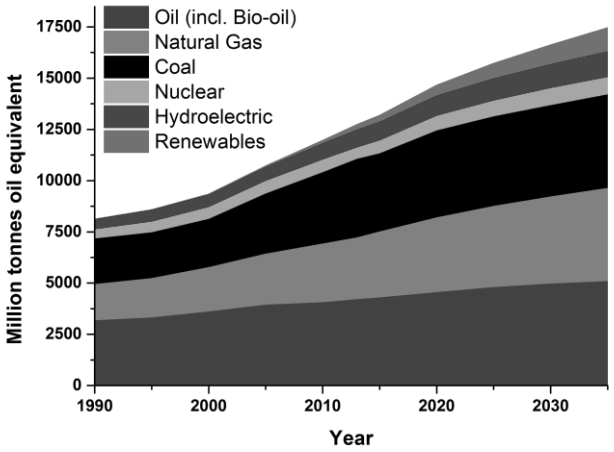

Figure 1: World primary energy consumption per energy source in million barrels of oil equivalent.[10]

Among solar fuels, hydrogen is the easiest to produce and can be used either directly as a fuel or as a raw material to produce, for instance, higher alkanes in the Fischer-Tropsch process or methanol and formic acid by hydrogenation of CO and CO_2.[18-20] Hydrogen can be generated in various processes but currently about 96% of hydrogen is produced from fossil fuels.[21] Evidently, this results in the emission of greenhouse-gasses and nullifies the intention to lower it. For example, naphtha steam reforming yields up to 10.5 tons of CO_2 per ton of the produced H_2.[22] It is imperative to produce hydrogen via a renewable and greenhouse-gas-free technology to achieve a sustainable hydrogen economy. These conditions can be satisfied when the solar energy is utilized to split water. This can be achieved for instance, by powering an electrolyser with a PV system (modular system). If the catalytic sites and light harvesting material are spatially combined we speak of photocatalytic materials. These materials (i.e. photocatalysts) can generate hydrogen by absorbing incident solar light and reducing water at the particle/electrolyte interface. Common photocatalysts are inorganic semiconductors like oxides (e.g. TiO_2, Fe_2O_3, SnO_2, Cu_2O), sulfides (e.g. CdS, ZnS, $CuInS_2$), nitrides (GaN, InN), and others.

1.3 A concept of the hydrogen economy

1.3.1 Hydrogen, a promising energy carrier

Throughout history, many philosophers and scientists have realized the potential of an economy based on water and hydrogen rather than fossil fuels. In 1923, Haldane proposed an alternative economy to reduce the dependency on dwindling fossil fuel reserves. He realized that the energy problem could be resolved if the fossil fuels – our primary energy source – were replaced with a renewable energy supply. Unfortunately, renewable energy sources are not as convenient as fossil fuels in terms of use, storage and transportation. He wrote, "The problem is simply one of storing their energy in a form as convenient as coal or petrol."[23] Thereby he realized that a successful implementation of a fossil fuel substitute can only be achieved when a minimal change of the current infrastructure is needed. Therefore a substitute for fossil fuels has to fulfill certain requirements: it should have high energy density, be easy to store and be utilizable in a well-established consumption technique (e.g. combustion).

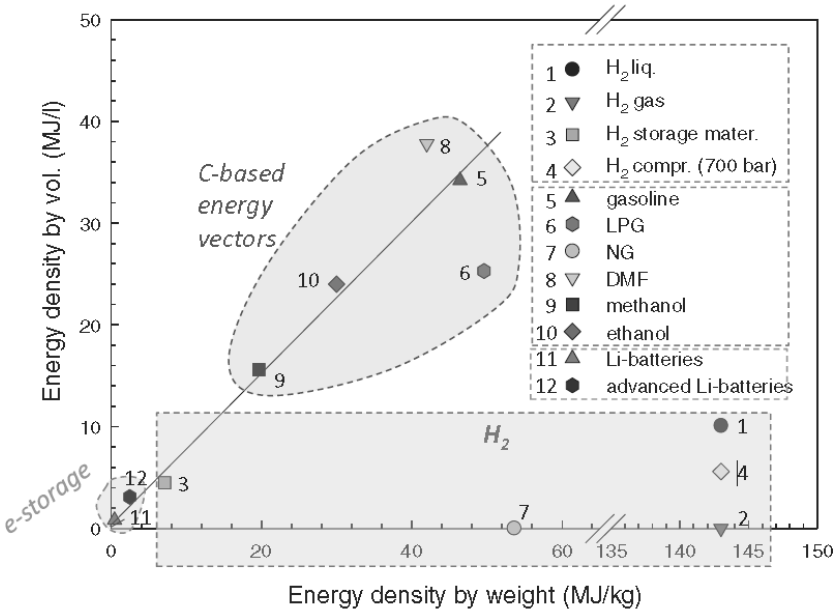

Figure 2: Energy Density per weight vs. per volume for liquid and gaseous fuels (from fossil sources or renewables such as ethanol and DMF), H_2 (liquid, gas, compressed at 700 bar, and stored in advanced nanomaterial) and electrical energy (Li batteries, conventional and advanced). (NG: natural gas; DMF: dimethyl furan; LPG: liquefied petroleum gas.)[24]

In this sense hydrogen is a suitable candidate either in its pure form or being stored in an energy carrier. Olah, Ferenc and Leitner proposed to store hydrogen in methanol or formic acid as an alternative to the elementary substance.[18, 19, 25] These carbon carriers can then be used in an alternative methanol or formic acid economy. However, in these alternative economies hydrogen still plays a central role as it is needed to reduce carbon monoxide and/or carbon dioxide to obtain these energy carriers. Storage of hydrogen in carbon carriers manipulates the energy density, which is a crucial factor for a successful implementation in the economy.

Molecular hydrogen has a high gravimetric density surpassing the carbon-based energy carriers found in fossil fuels, see Figure 2.[24] This creates possibilities with respect to the utilization of

hydrocarbons in conventional internal combustion engines (ICE). For instance, the same amount of energy is stored in only one-third of the fossil fuel mass. Hydrogen combustion in a conventional ICE (Otto cycle) is about 8% more efficient in comparison to gasoline (38% vs 30%).[26] Even higher efficiencies can be reached – up to 83% – if a fuel cell is used in combination with an electric motor.[27] Besides the higher efficiencies, hydrogen offers another important advantage: in contrary to the fossil fuels, hydrogen oxidation – described by the reaction (1.1) – yields only water as a product, eliminating emission of greenhouse gasses or harmful volatile organic compounds (VOC's).

$$H_2 + \frac{1}{2}O_2 \rightleftharpoons H_2O; \quad \Delta H = -237\ kJ/mol \tag{1.1}$$

1.3.2 Storage of hydrogen: challenges and approaches

Despite the fact that hydrogen has very high gravimetric energy density, its volumetric energy density is the main issue as it is about 14 to 40 times lower than carbon-based energy carriers, see Figure 2.[24, 28] To reach the economic viability, hydrogen's volumetric energy density needs to be drastically improved by ways of storage. Liquefaction of hydrogen is a well-known technique. However it imposes several technological challenges as the boiling point of hydrogen is -259°C, only 14 °C above absolute zero. Maintenance of this temperature over an extended period time requires a super-insulated cryogenic tank. Liquefaction on itself is very energy demanding and approximately 40% of the energy content is used up for this process.[18, 21, 28, 29] Another option is to compress hydrogen to 700 bar, which requires about 10-15% of the energy content.[24, 29] Safety aspects of such setups are questionable because hydrogen is highly flammable and explosive, rendering leakages very dangerous. In recent years the storage of molecular hydrogen in different organic and inorganic structures received a lot of attention. These systems include metal hydrides (MH_x), metal-organic frameworks (MOF's), doped polymers, carbon nanotubes, amine boranes etc.[21, 28] Unfortunately both gravimetric and volumetric energy densities in these approaches are low and lie in the same region with batteries, see Figure 2. Besides this, high temperature is needed to release the stored hydrogen, severely lowering the overall efficiency.[28] The third approach to store hydrogen is the formation of high energy density liquids like methanol or formic acid by reducing CO and/or CO_2 with hydrogen. This chemical storage approach resolves the issue of the low volumetric energy density of molecular hydrogen while its high gravimetric energy density is maintained. In conclusion, to reach economic viability these storage techniques need high capacity, good ad/desorption kinetics, lightness, stability and low cost. [28]

1.3.3 Overview of the hydrogen production technologies

In contrary to the fossil fuels, molecular hydrogen cannot be found in natural reservoirs. It is always bound in different compounds (e.g. water, ammonia, hydrocarbons). Thus hydrogen has to be extracted from these compounds as schematically shown in Figure 3.[30] Several technologies are used for the large-scale hydrogen production. As it is not the scope of this project to provide a complete review of all hydrogen production processes, I will discuss only conversion of fossil fuels and biomass and electrolysis.

Hydrogen is produced primarily by chemical conversion of fossil fuels. Steam methane reforming (SMR), partial oxidation and autothermal oxidation of natural gas, or oil/coal gasification make up about 96% of the total production.[21] Natural gas can be converted into synthesis gas by a combination of the methane reforming and water-gas shift reactions. Subsequently hydrogen can be

separated from the synthesis gas. The chemical equations and enthalpy values are given for methane because it is the main component of the natural gas (i.e. ~95% for North Sea gas, globally ~87-97%).[20, 31] The methane reforming reaction – described by equation (1.2) – is endothermic and carried out under elevated pressure of 25-35 bar and temperatures of 700-1000°C. The water-gas shift reaction (1.3) in which CO is further oxidized to CO_2, yielding extra hydrogen, is an exothermic one. The overall reaction (1.4) represents the ideal case in which four hydrogen molecules are produced per methane molecule. [20, 32, 33]

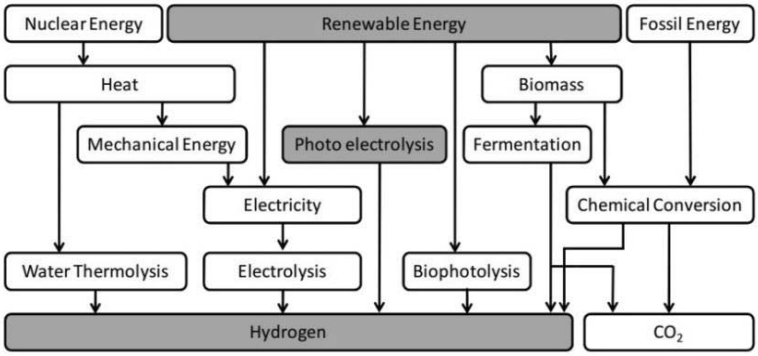

Figure 3: Schematic illustration of hydrogen generation from different energy sources and the correspondent conversion processes. Adapted from Enache et al.[30]

Steam methane reforming

$$CH_4 + H_2O \rightleftarrows CO + 3H_2 \quad \Delta H = +206 \text{ kJ/mole} \tag{1.2}$$

Water gas shift

$$CO + H_2O \rightleftharpoons CO_2 + H_2 \quad \Delta H = -42 \text{ kJ/mole} \tag{1.3}$$

Overall reaction

$$CH_4 + 2H_2O \rightleftharpoons CO_2 + 4H_2 \quad \Delta H = +164 \text{ kJ/mole} \tag{1.4}$$

Partial oxidation, autothermal reforming of fossil fuels and gasification of coal are other viable routes towards hydrogen as it can be seen in equations (1.5), (1.6) and (1.7). These technologies require oxygen which is very costly because the cryogenic distillation is needed to extract it from air. However these reactions are exothermic and lower the need for the external heating. Ultimately it comes down to the scale of the operation. For small plants an SMR setup is preferred as cryogenic distillation costs are higher than the costs of the furnace heating, while large plants generally use autothermal reforming. In the latter case the cost of the cryogenic distillation is overcome by the savings made on heating.[34] Autothermal reforming can be seen as a combination of the steam reforming and partial oxidation as both H_2O and O_2 are supplied.[35]

Partial oxidation of methane

$$CH_4 + \frac{1}{2}O_2 \rightleftharpoons CO + 2H_2 \quad \Delta H = -38 \text{ kJ/mole} \tag{1.5}$$

Autothermal reforming of methane

$$CH_4 + \frac{1}{2}H_2O + \frac{1}{4}O_2 \rightleftharpoons CO + \frac{5}{2}H_2 \quad \Delta H = +85 \text{ kJ/mole} \tag{1.6}$$

Coal gasification (unbalanced)

$$CH_{0.8} + O_2 + H_2O \rightleftharpoons CO + CO_2 + H_2 + \text{other products} \tag{1.7}$$

As one can notice, the processes described above still utilize fossil fuels and result in greenhouse-gasses emission thereby neglecting the goal to reduce the fossil fuel consumption. Carbon monoxide is yet another problem posed by these hydrogen generation processes. This molecule can easily poison the Pt-based catalysts employed in fuel cells by blocking the active sites, rendering CO free hydrogen feeds imperative.[36] However, CO-free hydrogen is difficult and expensive to produce via these routes. Due to these reasons a lot of effort is put towards the development of environmentally benign technologies to generate molecular hydrogen. One option which (from the technological point of view) is closely related to the fossil–fuel-based processes is the gasification and reforming of biofuels, e.g. bio-ethanol, oils. This approach uses renewable feedstock (i.e. biomass) to generate hydrogen which results in no carbon emission in the ideal case. However the high molecular complexity of biomass impedes the reforming process and results in the formation of byproducts like tar.[35, 37] It should be noted that the fuel generation from biomass reforming competes (in)directly with the food production via the used cultivated area. This inevitably results in a large number of debates.

Another contributor of hydrogen generation, albeit only around 4% of the total production, is the electrolysis of water. In this process water is split directly into hydrogen and oxygen by means of electrical energy.[38] This process has several advantages in comparison to the ones described above. First of all, the produced hydrogen is of high purity and can be directly used in fuel cells. Secondly, water is a convenient and abundant raw material and the only byproduct is oxygen. The overall reaction is shown in equation (1.8).

Electrolysis of water

$$H_2O \rightleftharpoons H_2 + \frac{1}{2}O_2 \quad \Delta H = +237 \text{ kJ/mole} \tag{1.8}$$

This process requires electrical energy which can be supplied by fossil-fuel-based power plants, nuclear power plants or renewable energy sources like wind farms, hydropower plants or photovoltaic systems.[30] The overall efficiency is the main issue. The primary energy (solar light, wind, or chemical energy of fossil fuels) is converted into an intermediate form (i.e. electricity), which is then converted and stored in the form of molecular hydrogen. Each stage has its efficiency which is always below 100% and the overall efficiency is the product of the efficiencies of all individual steps. For example, using a combination of a commercial (i.e. Si-based) photovoltaic system as an energy supply and an electrolyser, an overall efficiency of 8% is a realistic value.[39] Another issue is the relatively short lifespan of electrolysers: approximately 5 years.[40] Large scale implementation of electrolysis also requires a tremendous amount of scarce and expensive metals like iridium and platinum.[40]

A convenient system for water electrolysis which is described above is a modular one with spatially separated energy supplying unit and an electrolyser. If the light-absorbing material and water reducing/oxidizing catalytic centers are combined in a single particle, we speak of photocatalysis. In this approach the solar energy can be captured and converted into hydrogen directly by means of photocatalysts. Photocatalysts are usually composed of inorganic semiconductors (e.g. oxides, sulfides, nitrides, selenides or phosphides) in combination with (metallic) co-catalysts deposited on their surface. These semiconductors act as light absorbing material capturing the photon energy that can then be used to drive reduction/oxidation of water. How these materials can be used to generate hydrogen is discussed later.

1.4 Semiconductor-based photocatalysts

Semiconductors can be considered as important as fossil fuels for modern civilization since they form the backbone of the digital revolution. This prominent role originates from the electronic structure of these materials. This electronic structure also determines their photocatalytic properties. The following sections describe in detail the phenomena related to the photocatalytic hydrogen production.

1.4.1 Energy bands, Fermi level and types of semiconductors

Three types of solid materials can be differentiated based on their conductivity: metals, insulators and semiconductors. In metals the conduction and valence bands overlap, allowing free transport of electrons which results in high electrical and thermal conductivity. In contrast to metals, insulators display a large energy difference (>4 eV) between the bottom of the conduction and the top of the valence bands. This energy difference is called a band gap. The wide band gap of insulators prohibits transport of electrons from valence band (VB) to the conduction band (CB). Semiconductors have intermediate band gaps to these two systems. A band gap between 1 and 4 eV allows thermal and optical excitation of electrons from the valence band to the conduction band.[41] The band diagrams of all three types of materials are schematically shown in Figure 4.[30]

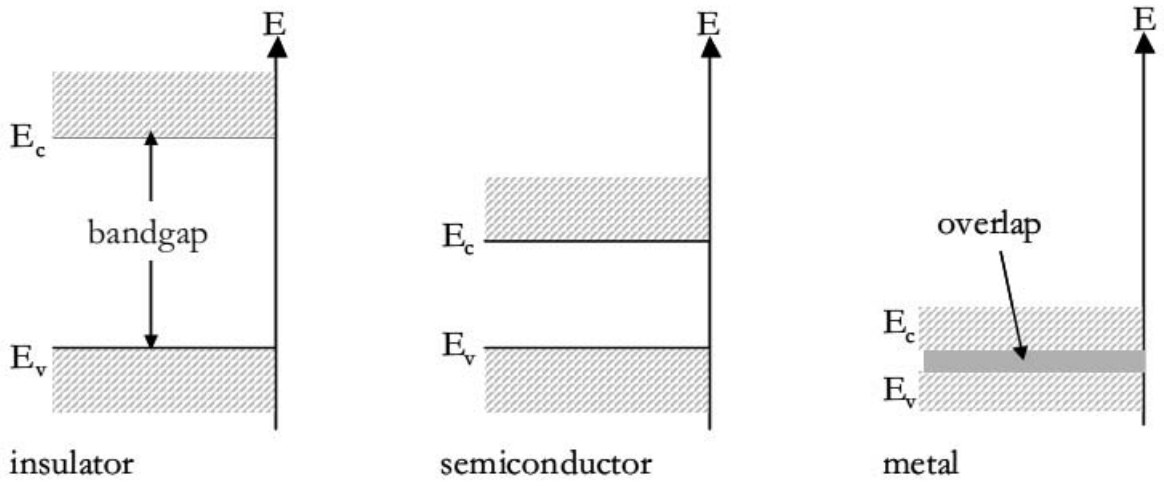

Figure 4: Band diagrams for insulator (large E_g), semiconductor (small E_g) and metals (overlap). E_C and E_V denote the conduction and valence band edge energies.[30]

An important characteristic of a semiconductor is the Fermi level position because it determines the type of the semiconducting material: either i-, n- or p-type. In solid state physics, the Fermi level is

defined as the energy level at which the chance of occupation of a state is exactly 50%. The Fermi level of a semiconductor can be calculated using equation (1.9). N_V, E_V, N_C and E_C are the effective Density of States and edge energies of the VB and CB, respectively. T is temperature in Kelvin and k is the Boltzmann constant. [42]

$$E_F = \frac{1}{2}(E_V + E_C) + \frac{1}{2}(kT \ln \frac{N_V}{N_C}) \quad (1.9)$$

In intrinsic semiconductors (e.g. i-Si), the Fermi level lies exactly in the middle of the conduction and valence bands. Extrinsic semiconductors are obtained when defects or impurities alter the electronic structure (e.g. by doping). When electron donors are added to form an n-type semiconductor, donor states are formed below the conduction band. Excitation, either thermal or optical, of these donor state electrons into the conduction band is easy. This allows the electrons to move freely through the crystal lattice in the delocalized CB while a bound hole is left at the dopant atom. The Fermi level shifts towards the conduction band since electrons occupy higher energy levels, see Figure 5 left. When electron acceptors are added to form a p-type semiconductor, acceptor states are formed above the valence band and accept valence band electrons, effectively bounding them. Free holes are then formed in the valance band and thus the Fermi level lowers toward the valence band, see Figure 5 left. In semiconductors, these electrons and holes can move freely and are therefore called charge carriers. For n-type semiconductors, electrons are the majority of the free charge carriers while a small amount of free holes is present in the system. Therefore electrons and holes are referred to as the majority and minority charge carriers respectively. For the p-type semiconductors the situation is opposite: holes are the majority charge carriers while small amount of free electrons are the minority charge carriers. In this thesis $Cd_xZn_{1-x}S$ ($0 \leq x \leq 1$) – an n-type semiconductor – is used. Therefore we will focus on n-type semiconductors and refer to electrons as majority charge carriers while holes will be referred to as minority charge carriers.

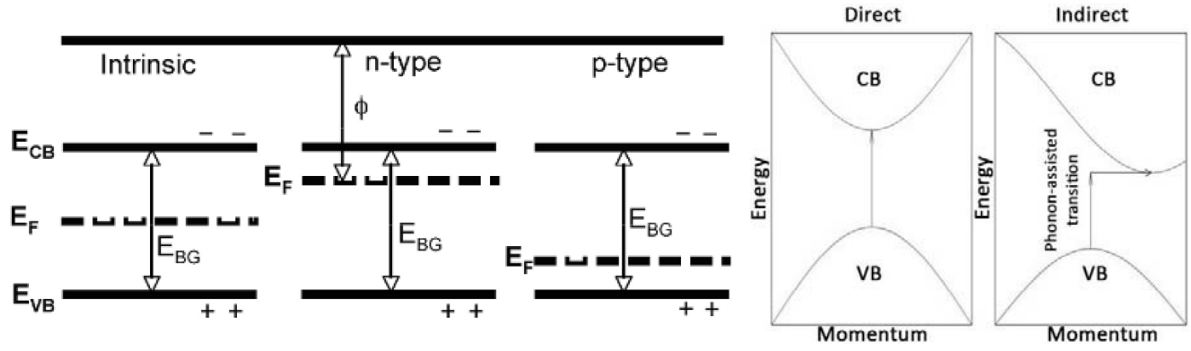

Figure 5: (left) Fermi levels, conduction and valence band edges for an intrinsic, n-type and p-type semiconductor.[42] (Right) Direct and indirect transition of electrons. Adapted from Kitai et al.[43]

Semiconductors differ not only by the type of the majority charge carriers (n- and p-type materials) but also by the type of the band gap: direct and indirect band gaps.[43] The type of the band gap depends on the electronic band structure. Indirect band gap materials have the maximum of the VB and the minimum of the CB at different electron momenta, see Figure 5 right. Thus coupling with a phonon (a crystal lattice vibration) is needed to allow optical excitation. In the direct band gap materials the maximum of the VB and minimum of the CB are positioned at the same electron momentum, eliminating the need for phonons, see Figure 5 right. Thus the direct transitions are

more probable and the absorption coefficients for the direct band gap semiconductors are higher. The semiconductor that was used in this work, i.e. $Cd_xZn_{1-x}S$, is an example of a direct band gap semiconductor.[44-46] For indirect band gap semiconductors absorption coefficients are much lower hence thicker material is needed for optimum absorption. This can be seen from the Lambert-Beer law, which states that the photon flux after passing a distance *x* through a material with an absorption coefficient *α* is lowered by a factor of $e^{-\alpha x}$, see equation (1.10). The absorption coefficients of direct and indirect transitions depend differently on the wavelength of exciting quanta. Equation (1.11) is valid for direct transitions, while equation (1.12) is for indirect transitions; *A'* is a proportionality constant:

$$I(x) = I_0 e^{-\alpha x} \tag{1.10}$$

$$\alpha = A'(h\nu - E_g)^{1/2} \tag{1.11}$$

$$\alpha = A'(h\nu - E_g)^{2} \tag{1.12}$$

When photons with energy higher than the bad gap are absorbed by the photocatalyst, an electron is excited from the VB to the CB leaving a hole. These charge carriers form an electron hole pair (EHP) held together by coulombic forces. Inorganic materials in general have a high dielectric constant, lowering the strength of this interaction. Therefore EHPs can be separated relatively easy. These processes are described in greater detail in the coming sections.

1.4.2. Semiconductor/electrolyte interface in dark conditions

The photogenerated EHPs have to be separated into electrons and holes which can then reach the photocatalyst/electrolyte interface to drive the redox reactions. This separation occurs due to the formation of an electric field in the semiconductor. This electric field stems from equilibration of the Fermi levels at the photocatalyst/electrolyte interface. The electrochemical potential of electrons E_{redox} in the electrolyte can be described by the Nernst equation (1.13). C_{ox} and C_{red} stand for the concentration of oxidized and reduced species, respectively, *R* – is the gas constant, *n* – the number of electrons involved in the reaction, *T* – the temperature in Kelvin, and *F* – the Faraday constant.

$$E_{redox} = E^0{}_{redox} + \frac{RT}{nF}\ln\left(\frac{C_{ox}}{C_{red}}\right) \tag{1.13}$$

Conventionally the E_{redox} values are determined with respect to the Standard Hydrogen Electrode (SHE) which is arbitrarily set as zero volts. The Fermi level of the electrolyte can then be deduced using the Nernst equation. E_{redox} of the SHE lies at -4.5 eV with respect to the vacuum level.[40] Thus the position of the Fermi level with respect to the vacuum can be determined via the equation (1.14).

$$E_{F,redox} = -4.5eV - eE_{redox} \tag{1.14}$$

When the photocatalyst is immersed in the liquid electrolyte, the Fermi levels of the two will equilibrate by charge carrier transfer at the interface. The Fermi level of a n-type semiconductor is usually higher than the $E_{F,redox}$ of an electrolyte, although this is not always the case. For consistency we will assume that the semiconductor Fermi level is the higher of the two. During equilibration electrons are transferred from the semiconductor to the electrolyte through the interface. The Fermi

levels equilibrate until $E_F=E_{F,redox}=E_{F,equil}$. Hence a net positive charge is left in the semiconductor near the interface, inducing the bending of the conduction and valance bands, see Figure 6 middle. This results in the formation of a built-in potential V_{SC} and a depletion region in the semiconductor with the thickness W.

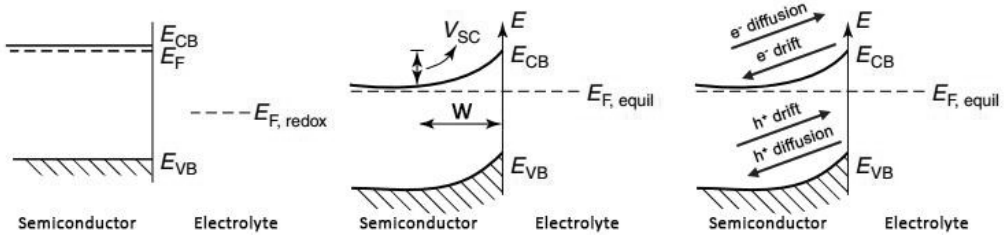

Figure 6: Energy levels of an n-type semiconductor in contact with an electrolyte solution: before (left) and after equilibration (middle). Drift and diffusion of majority and minority charge carriers (right). Adapted from Krishnan et al.[41]

After the Fermi levels equilibrate, EHPs are generated and recombine continuously. The build in potential V_{SC} separates these EHPs by sweeping the majority charge carriers (i.e. electrons) away from the interface to the semiconductor interior, see Figure 6 right. This is called drift transport. Transport towards the interface is induced by diffusion due to the charge carrier concentration gradient. The opposite behavior is observed for the minority charge carriers (i.e. holes). In this way a dynamic equilibrium is established with a zero net current flowing through the interface. Hence this built-in potential V_{SC} effectively separates the thermal EHPs, as we are describing dark conditions. The charge carrier concentrations can be calculated by equations (1.15) and (1.16).[43] The difference in the energy between the CB and the Fermi level is higher near the interface which lowers the majority charge carrier concentration *n* near the interface, see equation (1.15). Meanwhile the difference in energy between the VB and the Fermi level is lowered which raises the minority charge carrier concentration *p* near the interface, see equation (1.16). This illustrates the charge carrier separation due to the built-in potential V_{SC}.

$$n = N_c \exp\left(-\frac{Ec - E_F}{kT}\right) \tag{1.15}$$

$$p = N_v \exp\left(-\frac{E_F - E_V}{kT}\right) \tag{1.16}$$

Here *n* and *p* represents the electron and hole charge carrier concentration, N_C *and* N_V the Density of States in the conduction and valence band edges, E_C *and* E_V the energy of the conduction and valence band edges, E_F the energy of the Fermi level; *k* and *T* are the Boltzmann constant the temperature in Kelvin, respectively.

1.4.3. Semiconductor under illumination

Illumination of the photocatalyst will result in the generation of charge carriers if the energy of the photons is higher than the semiconductor band gap energy E_g. The generated charge carriers need to be separated by the built-in potential before redox reactions can occur. This separation is not perfect and losses are inevitable. The efficiency of the photocatalyst may be expressed in several ways but the most widely accepted one is the quantum yield. The quantum yield (Φ) is defined as the number

of specific events per absorbed photon. In our case these specific events can be defined as the reduction of a proton to a hydrogen atom. Other definitions of the specific events also exist like emission of photons in the case of fluorescence. Another, more important, parameter of a photocatalytic system is the energy conversion efficiency (η) that is defined as the output of energy divided by the invested energy. This value can be calculated by dividing the power output P (W) of the system by the intensity of the incident light I_{sun} (W/m²) and illuminated area A (m²), see equation (1.17).

$$\eta = \frac{P}{I_{sun} \bullet A} \tag{1.17}$$

The efficiency of the photocatalytic hydrogen generation, or any light induced process in general, is lowered by different energy losses. Firstly, red losses are possible if the energy of the incident photons is too low for the excitation (i.e. smaller than the band gap). This energy is lost as the photocatalyst cannot absorb the photons. If the photons' energy is higher than the semiconductor band gap E_g, blue losses occur. These high energy photons excite electrons into higher energy states of the CB from which they relax back to the energy states near the CB edge and the excess of energy is lost in the form of heat. The energy losses do not originate only from the mismatch between the photon energy and the semiconductor band gap but also from the intrinsic behavior of the charge carriers. As the charge carriers have only a limited lifetime, some of them cannot reach the surface and take part in the redox processes, undergoing (non-)radiative recombination in bulk. They might also recombine on the surface if the redox process is not fast enough or if species that can be reduced or oxidized cannot reach these charge carriers. Thus recombination substantially lowers quantum and energy conversion efficiencies. In some cases the recombination can be suppressed (for instance via optimization of the semiconductor thickness or by applying an external electric potential) but this process can never be eliminated completely as it is inherent to the charge carrier behavior. All three types of losses are illustrated in the Figure 7.[47]

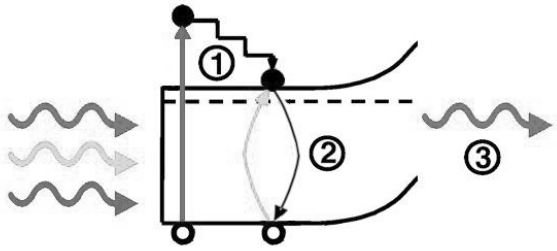

Figure 7: Loss pathways in a semiconductor: 1) blue loss of high energy photons, 2) recombination of the charge carriers, 3) red loss of low energy photons. Adapted from Conibeer.[47]

Charge carrier separation by the build-in potential V_{SC} is key to prevent recombination of the generated charge carriers. Thus the physical distance between the region where the charge carriers are generated and the depletion zone is an important parameter. If the diffusion length L_D is large enough to let them reach the depletion zone, separation of the charge carriers can occur. The diffusion length L_D depends both on the lifetime τ and diffusion coefficient D of the charge carrier and is defined as follows

$$L_D = \sqrt{D\tau} \tag{1.18}$$

Charge carrier separation and recombination are illustrated in the Figure 8. Excitation of an electron in the depletion region (I) can result in the charge carrier separation by the built-in potential V_{SC}. Charge carriers generated in the second region (II) at a maximum distance of L_D+W away from the interface may reach the depletion zone and be separated by the built-in potential before recombination. While generation of the EHPs in the third region (III) will result in the recombination as the charge carriers cannot reach the depletion zone. Hence recombination depends on the region of generation of the charge carriers in the bulk semiconductor.[12]

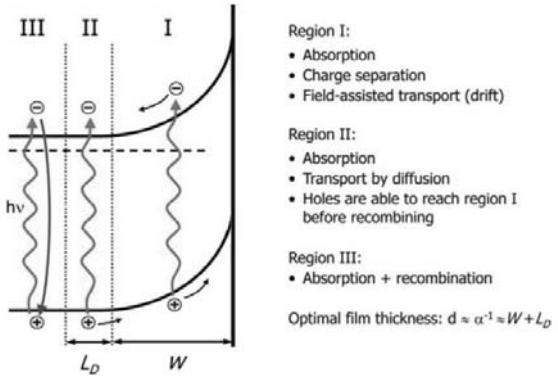

Figure 8: Generation of charge carriers in the three regions of an equilibrated n-type semiconductor-electrolyte interface. Region I with the width W is the depletion zone where efficient charge carrier separation takes place. In region II, with the diffusion length L_D as width, charge carriers may reach the depletion zone and be separated. All charge carriers generated in region III will recombine.[12, 40]

1.4.4 Photocatalytic production of H_2

Charge carriers are generated when photons of appropriate wavelength are absorbed by the photocatalyst. These charge carriers can be separated by the built in potential V_{SC} or by electron/hole traps in the bulk or surface states. Once being separated, they can be used to reduce/oxidize water when the position of the photocatalyst band edges are properly positioned with respect to the redox potentials of water. The electrons in the CB of the photocatalyst can reduce water to molecular hydrogen, if the CB potential is negative enough with respect to the reduction potential of water. The holes in the VB can oxidize water to form oxygen if the VB potential is positive enough with respect to the oxidation potential of water. This is illustrated in the Figure 9 (left) on the example of TiO_2 (anatase) as the photocatalyst.[40]

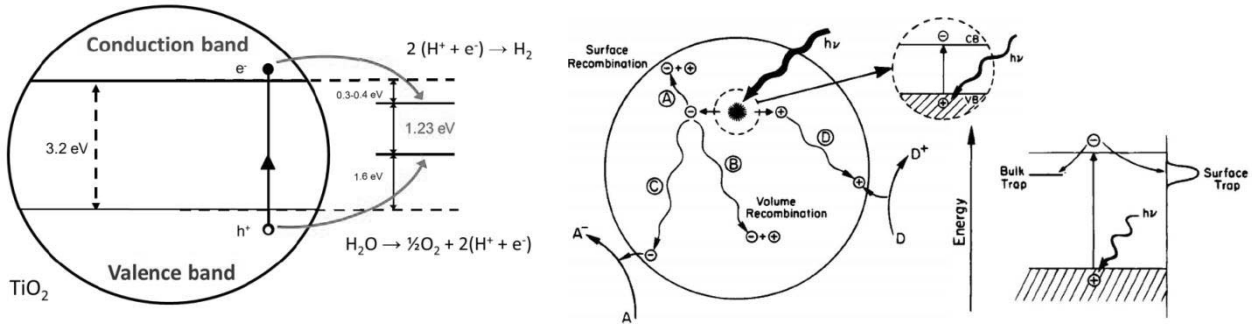

Figure 9: (Left) Energy diagram of a TiO_2 (anatase) photocatalyst in combination with half reaction redox potentials of water. (Right) Illustration of charge carrier generation, their transport to the photocatalyst/electrolyte interface for oxidation and reduction of the electrolyte, and trapping of an electron in a bulk and surface trapping site. [40, 48, 49]

To describe this phenomenon in more detail we have to look at the behavior of the charge carriers in a particle of a photocatalyst, see Figure 9 right.[48, 49] First, free charge carriers are formed upon the separation of the generated EHPs. These charge carriers can migrate towards the photocatalyst/electrolyte interface and participate in the reduction (electrons) and oxidation (holes) reactions of the electrolyte via pathways C and D respectively. However some of the charge carriers that reach the interface can still recombine on the surface trap states if the reaction with the electrolyte is slow, see pathway A. At the same time not all charge carriers can reach the interface and some of them recombine in the bulk before ever reaching the surface of the particle, see pathway B. Bulk recombination centers can be faults in the crystal lattice of the photocatalyst, while the surface states can be formed by the disruption of the crystal lattice, which are also called "dangling bonds".[43] Impurities and dopants can also create different trapping sites. The nature of the surface states and bulk recombination centers determines the activity of the photocatalyst. They can suppress recombination by enhancing charge carrier separation, but they can also enhance the recombination rate if the concentration of (bulk) defects is too high. Thus efficient trapping of the charge carriers in surface states with a low quantum efficiency for (non)-radiative surface recombination is desirable to obtain a highly active photocatalyst.

The reactions occurring at the photocatalyst/electrolyte interface can be summarized as equation (1.20) and (1.21). Their redox potential E_{redox} can be determined with the Nernst equation (1.19) (assuming the activity coefficients being equal to 1), where R is the gas constant, T – the temperature in Kelvin, F – the faraday constant, n – the number of electrons involved, and $C_{ox/red}$ – the oxidant and reductant concentrations respectively. These potentials are valid for P_{H2}=P_{O2}= 1 bar, pH= 14 and T= 25°C. At other pH the values can be calculated by increasing the potential by 59.2mV per pH unit decrease (e.g. for pH= 0, $E_{H+/H2}$= 0V and $E_{H2O/O2}$ = +1.23V).

$$\mathrm{E}_{redox} = \mathrm{E}^0 + \frac{RT}{nF}\ln(\frac{C_{ox}}{C_{red}}) \tag{1.19}$$

$$\text{Reduction: } 2H_2O + 2e^- \rightleftharpoons H_2 + 2OH^- \quad \mathrm{E}_{H+/H_2} = -0.83\mathrm{V} \tag{1.20}$$

$$\text{Oxidation: } 4\mathrm{OH}^- \rightleftharpoons O_2 + 2H_2O + 4e^- \quad \mathrm{E}_{H_2O/O_2} = +0.40\mathrm{V} \tag{1.21}$$

1.4.5 Photocorrosion

Photocorrosion is the main issue of many semiconductor-based photocatalysts. For instance, the semiconductor that we used in this work ($Cd_xZn_{1-x}S$) is deteriorated by this phenomenon. Therefore we discuss photocorrosion on the example of CdS. Oxidation of water is a complicated process requiring transfer of 4 electrons and a break of two O-H bonds to generate one O_2 molecule (in comparison only 2 electrons and no bond cleavage are involved in the formation of H_2). Hence the oxidation of water is slow and the generated holes do not oxidize the electrolyte fast enough at the semiconductor-electrolyte interface. Subsequently the holes in the valence band at the interface oxidize the S^{2-} anions in the semiconductor lattice instead, see equation (1.22). This corrosion releases Cd^{2+} into the solution and forms elemental sulphur.[50]

$$CdS + 2h^+ \rightleftharpoons Cd^{2+}_{(aq)} + S\downarrow \tag{1.22}$$

This process can be counteracted by two approaches. The first is described in more detail later in this report and makes use of OER co-catalysts like RuO_2 or RhO_3. The potential difference between the valence band edge of $Cd_xZn_{1-x}S$ and the H_2O/O_2 redox potential is large enough to drive the reaction. However a large overpotential is seen for the OER and stops the reaction from occurring. These OER co-catalysts lower the overpotential for O_2 production and thereby enabling reaction (1.23). [50-52]

$$4h^+ + 2H_2O \xrightleftharpoons{RuO2} 4H^+ + O_2 \quad (1.23)$$

A second approach is the use of sacrificial reactants. These reactants act as hole scavengers and donate electrons to the VB of the photocatalyst effectively suppressing the photocorrosion, see equations (1.24), (1.25), and (1.26).[50] Usually for sulfide photocatalysts a combination of Na_2S and Na_2SO_3 is used. Sulfide forms S_2^{2-} upon oxidation by the holes. This disulfide ion absorbs light on itself and interferes with the light absorption by the photocatalyst. The disulfide can also compete with protons for the electrons and be reduced back to $2S^{2-}$, lowering the photocatalytic efficiency.[53] Sodium sulfite is added to decompose the disulfide to sulfide and thiosulfate.[52] One can see that a continuous feed of sulfide is needed to reduce the optically generated holes and keep the HER reaction going over a long period of time.[53]

$$SO_3^{2-} + H_2O + 2h^+ \rightleftarrows SO_4^{2-} + 2H^+ \quad (1.24)$$

$$2S^{2-} + 2h^+ \rightleftharpoons S_2^{2-} \quad (1.25)$$

$$S_2^{2-} + SO_3^{2-} \rightleftharpoons S^{2-} + S_2O_3^{2-} \quad (1.26)$$

1.5 Summary

Due to the extensive consumption of finite fossil resources, we can face an energy crisis in the near future. Steady emission of greenhouse gasses and VOCs also imposes detrimental effects on the climate and living environment. Therefore a shift from the finite fossil fuel resources to a renewable energy source is needed to safeguard the future of the modern civilization. However this renewable source should be compatible with the current energy infrastructure for a smooth transition. Our ever increasing energy demands could be met if we were using hydrogen or a hydrogen carrier as a substitute fuel. Transition to this model can lower the pressure on the fossil fuel reserves and the emission of greenhouse gases. However several issues have to be dealt with before this fossil fuel substitute can be implemented. Most importantly, for the sustainable economy, the production of hydrogen must involve only renewable energy sources and greenhouse-gas-neutral processes. Meanwhile about 96% percent of hydrogen nowadays is produced from fossil fuels by hydrocarbon reforming and gasification. The photocatalytic production of hydrogen by reduction of water on semiconducting materials under solar light is seen as an innovative route towards green hydrogen. However extensive research in this area is required because many factors (e.g. band gap, overpotentials, and stability) influence the activity of a particular photocatalytic system.

Development of the photocatalytic hydrogen production highlighted the use of mixed cadmium-zinc sulfides ($Cd_xZn_{1-x}S$; $0 \leq x \leq 1$) as a promising material.[54, 55] Its band gap (2.4-3.6 eV depending on x) can be tuned to absorb a large fraction of the solar spectrum while the potential of its conduction band edge is negative to reduce water. In order to evaluate the potential of this system in the

photocatalytic hydrogen production thorough research is required. A more in-depth introduction to the mixed Cd-Zn sulfide photocatalyst is given in chapter 2.

Chapter 2: $Cd_xZn_{1-x}S$ – a "*solid solution*" for hydrogen production?

2.1 $Cd_xZn_{1-x}S$ properties

Cadmium sulfide is a prominent example of the II-VI semiconductors. It has a distinct yellow color due to its band gap of 2.4 eV and is insoluble in aqueous solutions.[44] In nature the chalcogenide can be found in two polymorphs: either a cubic or a hexagonal crystal structure. The cubic zinc blende crystal structure is found in the mineral Hawleyite. It is build up by sulfur atoms in an fcc unit cell while cadmium atoms occupy half of the tetrahedral sites.[56] It can be seen as an "AaBbCc"-layered structure in which Aa, Bb and Cc each represent one bilayer (Capital letter = S, small letter = Cd).[57] Hexagonal cadmium sulfide, found in Greenockite mineral, adopts a wurtzite crystal structure. It can be divided into two sublattices, each adopting a hexagonal closed packed crystal (hcp) structure.[58] Hereby an "AaBbAa" layered structure is formed.[57] In both polymorphs both the cation and anion are tetrahedrally coordinated, see Figure 10.

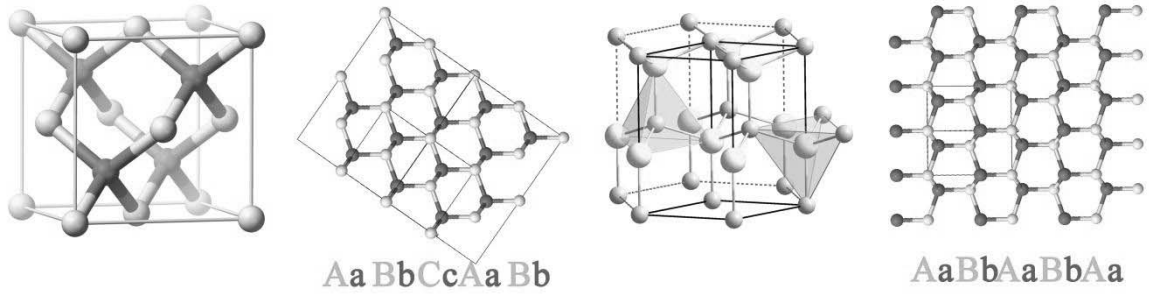

Figure 10: (Left) Cubic zinc blende crystal structure with sulfur in an fcc lattice and cadmium in ½ of the tetrahedral holes. (Right) Hexagonal wurtzite crystal structure with sulfur and cadmium each in a hcp sub-lattice.

The band structure of either cubic or hexagonal cadmium sulfide reveals a direct transition, thereby resulting in the strong optical absorption. The band gap of the cubic phase is 2.4 eV while the hexagonal phase is reported to have the bandgap of 2.3 eV.[44-46] The band gap is small enough to absorb a large fraction of the solar spectrum. The band edges of the CB and VB also align with the redox potentials of the hydrogen evolution reaction (HER) and oxygen evolution reaction (OER) respectively to allow the overall photocatalytic water splitting, see Figure 11 left. However overpotentials – the electrochemical counterpart of activation energies in catalysis – lower the hydrogen production rates. This can be overcome by shifting the conduction band to a more negative position.

Zinc sulfide is also a II-VI semiconductor with a direct band gap of 3.6 eV (cubic phase) or 3.9 eV (hexagonal phase). [46, 59, 60] Its valence band is positioned at approximately the same energy level as the one of cadmium sulfide, while its conduction band is positioned more negatively with respect to the CB of CdS, see Figure 11 left.[61] This difference results in a larger driving force for the reduction of protons to molecular hydrogen in comparison to CdS. On the other hand the large band gap limits the useable fraction of the solar spectrum to UV region only. Interestingly, cadmium sulfide and zinc sulfide can form solid solutions that obey Vegard's law not only for the crystal lattice parameters but also for the semiconductor band gap energies.[46, 54, 62] The band gap can be tuned by varying the cadmium to zinc ratio. The band gap and CB energy level raise with the increase of the zinc fraction,

see Figure 11 right.[54] As the electrons in the CB get more energy to overcome the overpotentials of the water reduction reaction the photocatalytic activity towards hydrogen production increases as a result of the higher driving force.[63] This effect has an optimum in respect to the zinc fraction. A more negatively placed CB enhances the HER, but on the other hand the widening of the band gap results in the decrease of the part of the solar spectrum that can be absorbed by the material. This results in the optimum of the x value in $Cd_xZn_{1-x}S$. Unfortunately a solid value is hard to define but in many cases in literature authors find it to be close to 0.5.[55, 64]

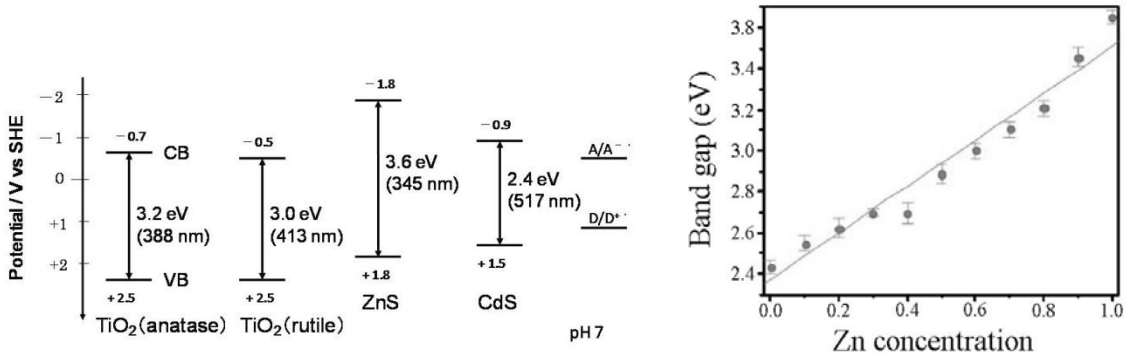

Figure 11: (left) Band gap and band edge positions of anatase TiO_2, rutile TiO_2, CdS and ZnS at pH=7. (right) Band gap of cadmium zinc sulfide solid solution in function of the zinc fraction. A linear trend is seen from 2.4 eV (pure CdS) to 3.6 eV (pure ZnS).[54, 61]

Recently a two-step synthetic approach has been developed for the synthesis of the highly active Cd-Zn sulfide.[57] Authors ascribed the enhanced photocatalytic activity of these chalcogenide solid solutions to the formation of the so-called nano-twinned particles. These particles contain twin planes which form along the (111) direction during the crystal growth of zinc blende phase. If a stacking fault induces twinning plane formation, the crystal growth continues mirrorwise in respect to the twin plane, see Figure 12. The bilayer in the twinning plane can then be seen as a thin layer of the Wurtzite crystal structure, creating a homojunction within the particles. Schematically this is illustrated as AaBbCcAaBbCc (ZB-ZB-ZB, no twinning) converting to AaBb[CcAaCc]BbAa (ZB-[WZ]-ZB, twinning) in Figure 12. These homojunctions have been claimed to effectively separate the photogenerated charge carriers to drive the HER and oxidation of the sacrificial reactants.[57] Although research conducted in our group has found an opposite correlation between the number of twinned $Cd_xZn_{1-x}S$ particles and the photocatalytic activity. [65]

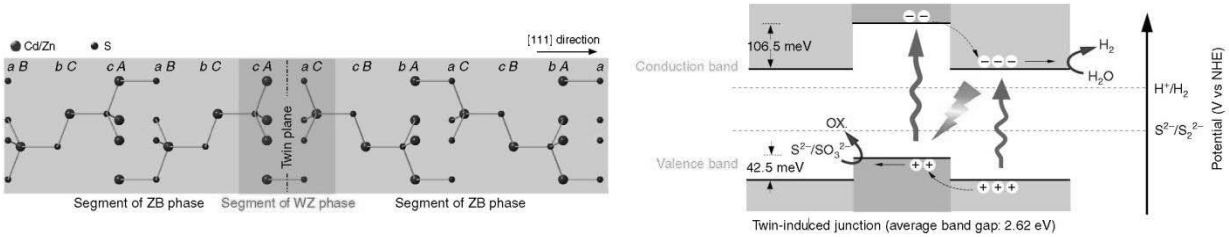

Figure 12: (Left) Ball&stick representation of twinning in $Cd_xZn_{1-x}S$, a ZB-WZ-ZB homojunction is formed. (Right) Separation of charge carriers at the twinning planes, subsequent proton reduction and sacrificial reactant oxidation.[57]

2.2 Improving the hydrogen generation rate of $Cd_xZn_{1-x}S$

The chalcogenides are a promising photocatalytic material for the HER. However there are certain problems that need to be addressed. First of all, hydrogen production rates require improvement and this can be achieved through various methods. Doping of the mixed metal sulfide can induce formation of the energy levels within the band gap decreasing its value. On one hand introduction of the dopants can improve light absorption and improve charge carrier separation but when the amount of dopant reaches a certain level it can enhance recombination rate. Besides addressing inherent recombination, the overpotentials can be lowered by means of co-catalysts resulting in higher HER rates. Among promising non-noble-metal-based co-catalyst other transition metal chalcogenides like MoS_2 and WS_2 should be mentioned.[66, 67] Research conducted in our group indicates that nanoparticles Cd-Zn sulfides tend to agglomerate and high dispersion is crucial for high photocatalytic activity. This agglomeration is likely to be caused by a low ζ-potential of the particles.[65] Therefore anchoring of the photocatalyst nanoparticles on a support could increase the hydrogen production by maintaining high dispersion. Besides mere anchoring, the support can form a heterojunction with the chalcogenide if a semiconducting support with an appropriate band position is used (e.g. TiO_2).[16, 68, 69] Such composite systems have been reported to have enhanced charge carrier separation. The aforementioned approaches are briefly described in the coming sections. Most emphasis is put on the supported photocatalyst as this is the focus of the thesis. I would like to point out that the direct comparison of the reported hydrogen production rates is a very difficult task because many parameters of the photocatalytic activity tests can be different (e.g. the concentration of the active photocatalyst in the testing cell, testing cell geometry, optics, power output of the lamp, longpass filter). The absence of a linear correlation between the power of the lamp and the hydrogen generation rate further complicates comparison.

2.2.1 Doping of the chalcogenide

Doping is one possibility to improve the photocatalytic activity of $Cd_xZn_{1-x}S$. The dopants introduce energy levels in the band gap.[43] This can improve the charge carrier separation. Wang et al. investigated the effect of Ni^{2+} doping by addition of $Ni(Ac)_2$ into the chalcogenide precursor solutions.[63] The hydrogen production rate was improved by 86% by doping 1.56wt% of Ni^{2+} in $Cd_{0.6}Zn_{0.4}S$. Other ions were also tested but did not increase the photocatalytic activity. Another paper reports an increase of 200% by doping $Cd_{0.1}Zn_{0.9}S$ with 1wt% of Cu^{2+}. Further optimization by Zhang and coworkers of the Cu^{2+} doped system increased the hydrogen production rate for $Cd_{0.33}(Zn_{0.95}Cu_{0.05})_{0.66}S$ by 45% compared to the $Cd_{0.1}Cu_{0.01}Zn_{0.89}$.[70] Another element that can be used for doping of $Cd_xZn_{1-x}S$ is Ag. Yuliati and coworkers optimized the Ag content to $Ag_{0.01}$-$(Cd_{0.1}Zn_{0.9}S)_{0.99}$, increasing the hydrogen production rate by 70% with respect to the undoped mixed metal sulfide. The authors assumed that the presence of Ag^+ leads to an increase in crystallinity, improved visible spectrum response and enhanced charge carrier separation.[71] In literature, it is proposed that Ag^+/Ag^0 species could be responsible for the charge carrier separation as well: holes oxidize metallic Ag to Ag^+ while electrons reduce it back to the metallic state. When small amounts of the dopant are used this can suppress recombination while high concentration of these sites promotes recombination and has a detrimental effect on the photocatalytic activity.[72, 73] Many other metals have been utilized as dopants in other works, among them Co^{2+}, Mn^{2+}, Sr^{2+} etc.[15, 63, 70, 74]

2.2.2 Co-catalysts

Besides the charge recombination there are other processes which decrease efficiency of the photocatalytic processes. Redox reactions occurring on the surface of the semiconducting particles (i.e. water oxidation and reduction reactions) are hindered by overpotentials. These can be seen as the electrochemical analogy of activation energies in chemical kinetics. Increasing the difference between oxidant's and reductant's electrochemical potential can speed up the electrochemical reaction (e.g. by addition of Zn in CdS), analogous to raising the temperature in thermally-activated chemical reactions. An electrochemical reaction can also be sped up by lowering the overpotential by means of a co-catalyst.

In general, noble metals have the lowest overpotentials and are widely used as electrocatalyst for the HER. Among noble metals Pt is used the most because of its high work function and chemical stability.[75] Platinum can be *in-situ* deposited by photogenerated electrons on the surface of sulfide particles. For that the sulfide is dispersed in a solution of H_2PtCl_6, and $PtCl_6^{2-}$ is reduced to metallic Pt^0 at the surface by the generated electrons. However, this method of photodeposition can lead to the formation of PtS and/or $Pt(OH)_2$ according to literature.[76] An extra step of heat treatment (>400°C) is then needed to complete the platinization. Metallic platinum acts as a trap for the generated electrons. Protons adsorb on the Pt surface, get reduced by electrons, recombine, and desorb as molecular hydrogen.[76] Other noble metals applicable for HER are Pd, Rh, Ru and Au.[52]

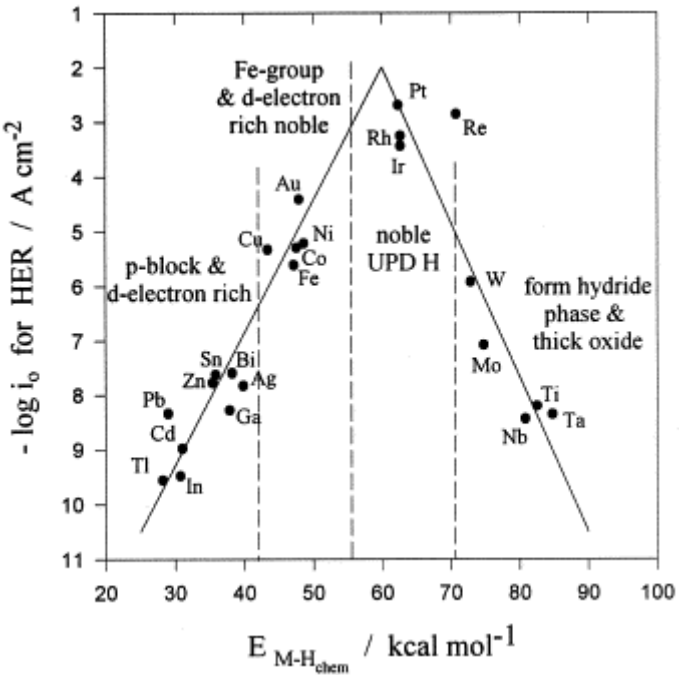

Figure 13: Exchange current density in function of the heat of hydrogen adsorption on the metal. A clear volcano plot is observed, showing that platinum has the lowest overpotential for hydrogen evolution.[77-79]

Overpotentials of the electrochemical reactions depend on the current density as found by Tafel et al. He showed that there is a logarithmic relation between the two.[80] This relation is described in the Butler-Volmer equation (2.1).[81] The Tafel slope is b=2.303RT/(1-α)nF, where the number of the involved electrons *n*, the Faraday constant *F*, an asymmetry parameter *α*, the current density *j* (A/cm²) and the exchange current density j_0 (A/cm²).

$$\eta = a + b\log(j) = -b\log(j_0) + b\log(j) \quad (2.1)$$

Upon irradiation the overpotential increases as the current density *j* raises. A trend among metals can be found as the exchange current density j_0 is unique for each. Trasatti and coworkers found a clear correlation between the exchange current j_0 and the heat of adsorption of hydrogen on the metal, see Figure 13[77-79] This explains the efficiency of Pt as it displays the lowest overpotential for the HER. The overpotential of the HER rises in the following order: Pt < Re < Rh < Ir < Au < Ni < ….

Some noble metals can also be used to catalyze the oxygen evolution reaction. Usually these metals are used in the form of oxides rather than in the metallic state. RuO_2 loaded on CdS has been reported to act as an OER co-catalyst by trapping holes and oxidizing water.[50, 51] The oxidation reaction is sped up enough to counter photocorrosion, which is a main issue of CdS (and $Cd_xZn_{1-x}S$). The authors state that even in the absence of a sacrificial electron donor, no corrosion was observed under illumination for over 44 hours.[50] The Rh_2O_3 has the same influence on the stability of the sulfide photocatalyst as RuO_2.[52] As a reference, we observed a complete loss of photocatalytic activity within 2 hours in the absence of sacrificial reactant.

Use of noble metals as co-catalysts raises questions due to their scarcity and high price. An advantage of $Cd_xZn_{1-x}S$ is its compatibility with other transition metal sulfides that are good HER co-catalysts. Molybdenum disulfide has been reported to be active and robust over a wide range of pH values, which makes it an attractive alternative. Nguyen and co-workers decorated $Cd_{0.8}Zn_{0.2}S$ with MoS_2 (3 wt%) which resulted in the 210-fold increase of the hydrogen evolution rate in comparison to the bare sulfide.[67] Zong et al. reported an increase by a factor of 36 with 2 wt% of MoS_2 loaded on pure CdS. In the latter case authors also loaded Pt, Ru, Rh, Au and Pd on CdS for the comparison but found MoS_2 to be the most efficient co-catalyst for HER. They suggest that matching electronic configurations and the formation of a heterojunction between the photocatalyst and the MoS_2 co-catalyst resulted in a higher hydrogen generation rate. The formation of this heterojunction can enhance charge carrier separation.[14, 82] Similar results were reported for the use of WS_2 as a co-catalyst.[66] Other transition metal sulfide co-catalysts are also proposed in literature e.g. NiS, SrS, CuS_2 etc.[83-86]

2.2.3 (Composite) supported $Cd_xZn_{1-x}S$

The suspensions of $Cd_xZn_{1-x}S$ are not colloidally stable and the nanoparticles tend to aggregate, most likely due to a low ζ-potential value.[65] This aggregation decreases the surface area exposed to the electrolyte and imposes mass transfer limitations of water molecules and/or sacrificial reagents into the voids between the particles. Inevitably this leads to loss of activity, see Figure 14. Thus maintenance of the dispersion of the photocatalytic particles is required for high photocatalytic activity. For this purpose different research groups deposited $Cd_xZn_{1-x}S$ on various supports. This does not only prevent aggregation of the photocatalyst but makes the separation of the photocatalyst from the reaction mixture easier (i.e. by filtration instead of centrifugation) if relatively big support particles are used (>0.1μm). Many systems have been reported in literature and here we briefly summarize different approaches.

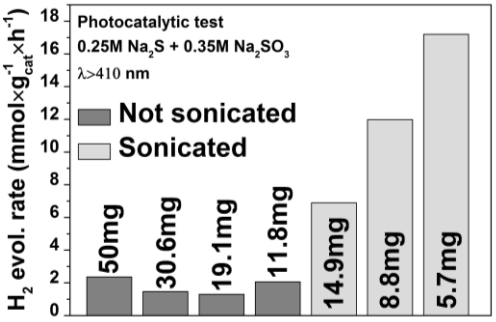

Figure 14: Normalized hydrogen evolution rates of different loadings of the unsupported $Cd_{0.5}Zn_{0.5}S$ in the test cell. Sonicated photocatalyst dispersions are substantially more active, even at lower loading.

SiO_2 is an insulator and does not participate in the redox reactions or form a heterojunction with the chalcogenide. Therefore it functions merely as a physical support. Macías-Sánchez and co-workers used ordered mesoporous SiO_2 (SBA-15; hexagonally ordered cylindrical pores) as a support for the mixed Cd-Zn sulfides in their work.[3] In this work authors utilized a simple co-precipitation technique to deposit the photocatalyst on the support. They suspended SBA-15 in the mixed aqueous solution of $CdAc_2{\times}2H_2O$ and $ZnAc_2{\times}2H_2O$ and then added Na_2S as the source of sulfur. Small angle XRD indicated that SBA-15 was stable under the conditions of the photocatalytic tests (visible light illumination, mixed solution of 0.35M Na_2S and 0.25M Na_2SO_3 as sacrificial reactants). The hydrogen production rate of $Cd_{0.8}Zn_{0.2}S$/SBA-15 was reported to be higher than one of the unsupported particles but no value for the unsupported sulfide was given. Later the same group of authors used an identical approach to deposit $Cd_{0.8}Zn_{0.2}S$ on SBA-16 (mesoporous SiO_2 with square channels).[64] The $Cd_{0.8}Zn_{0.2}S$/SBA-16 was reported to be the most active sample in the series with the hydrogen production rates equal to $Cd_{0.8}Zn_{0.2}S$/SBA-15. Another mesoporous SiO_2 used as support for Cd-Zn sulfides is MCM-41 (hexagonally ordered cylindrical pores). Hirai et al. prepared CdS/MCM-41 via surface modification of MCM-41. The silica was modified by 3-mercaptopropyltrimethoxysilane to introduce thiol functionalities at the surface. Cadmium sulfide nanoparticles were then prepared via an inverse micellar method with the subsequent introduction of the support. The sulfide nanoparticles were loaded using the MCM-41 molecular sieve properties.[1] Even though silica is an insulator and cannot participate in the redox reactions, it shows electronic interactions with the photocatalyst via the surface bonds: Weiß et al. suggested that these so-called “semiconductor-support interactions” (SEMSI) alter the band gap energy and flatband potential.[87] In their work authors loaded mesoporous silica with various amounts of CdS. Diffuse reflectance UV-VIS spectroscopy indicated a higher band gap energy for the lower loadings. Comparison of the XRD and TEM data indicated that this effect did not originate from quantum confinement effects as the size of the nanocrystallites was independent of the loading and identical in all cases. Interaction between the silica support and CdS nanoparticles results in the formation of Si-O-Cd bonds, which can alter the electronic structure of the latter. As the loading of the nanoparticles decreases, the electronic effect becomes stronger. This can be explained by the fact that at lower loadings the aggregates of CdS decrease in size. Therefore the fraction of the surface-bonded CdS particles increases with the decrease of the loading, which results in the increase of the apparent band gap. The authors proposed that an anodic shift of the valence band edge lies at the core of this effect. Other $Cd_xZn_{1-x}S/SiO_2$ composite systems that can be found in literature are CdS on Al-HMS, CdS in zinc doped SBA-15, CdS in MCM-48. [1, 2, 88]

The most extensively studied support for $Cd_xZn_{1-x}S$ by far is TiO_2.[68, 69, 89] Titanium dioxide is a photocatalyst on itself which has a wide band gap of 3.0 or 3.2 eV (for rutile or anatase phase respectively) and can therefore absorb only UV light.[61] The conduction band of TiO_2 is positioned more positively with respect to the CB of $Cd_xZn_{1-x}S$, which means that the oxide can accept electrons from the sulfide by forming a heterojunction, see Figure 15. This can promote charge carrier separation and enhance the hydrogen generation rates. Besides the positive effect of such a coupling there are possible drawbacks that should be noted. The VB of TiO_2 is positioned more positively with respect to the VB of $Cd_xZn_{1-x}S$ and may result in the accumulation of the holes on the sulfide as there is an electrical barrier which prohibits their transfer to the titania. This accumulation of the holes can enhance photocorrosion of the sulfide which is known to be the main stability issue of $Cd_xZn_{1-x}S$. Another drawback could be the diffusion length of the charge carriers. As the support has larger dimensions, the generated majority charge carriers can be trapped in the titania bulk before they reach the TiO_2-electrolyte interface. One last aspect is the overpotential of the HER. The electrochemical driving force of the electrons decreases when they are transferred from the sulfide to the titania CB as the CB of the latter is more positive in potential. Consequently the hydrogen generation rate could be lowered by the lack of driving force. However, to the best of our knowledge, all published $Cd_xZn_{1-x}S/TiO_2$ composites show higher hydrogen generation rates thus the charge carrier separation by the heterojunction outweighs the possible drawbacks.[68, 69, 89]

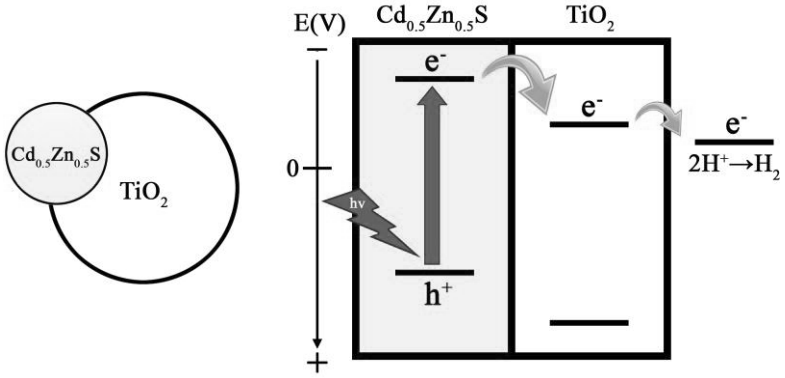

Figure 15: Charge carrier separation over a heterojunction between $Cd_{0.5}Zn_{0.5}S$ and titania (anatase). Adapted from Kohtani et al.[61]

Chen and coworkers reported the synthesis of the $Cd_{0.5}Zn_{0.5}S$@titania nanotubes composite.[68] They prepared the nanocomposite in a one pot synthesis. $CdAc_2{\times}2H_2O$ and $ZnAc_2{\times}2H_2O$ were added to a rutile dispersion (in 10M NaOH), later thioacetamide was added as the sulfur source. The mixture was then hydrothermally treated at 150 °C for 48 hours to synthesize both the sulfide and the titania nanotubes simultaneously. This resulted in $Cd_{0.5}Zn_{0.5}S$ nanoparticles of ca. 90 nm enwrapped by titania nanotubes. The activity of the $Cd_{0.5}Zn_{0.5}S@TiO_2$ nanotubes towards the hydrogen evolution reaction was found to be about 13 times higher compared to the unsupported sulfides. The high activity was attributed to the high dispersity of the sulfide nanoparticles in the titania nanotube network and the multipoint contact between the sulfide and the titania which resulted in enhanced charge carrier separation. Also activity of the nanocomposite towards the hydrogen evolution reaction was found to be stable for at least 6 days. Later, Li and coworkers reported the synthesis of the $Cd_{0.65}Zn_{0.35}S$@titania nanotubes nanocomposite.[89] First they prepared the titania nanotubes consisting of highly crystalline anatase phase. These nanotubes were dispersed in a metal-ammonia

complex ($Cd(NH_3)_4^{2+}$ and $Zn(NH_3)_4^{2+}$) solution for ion exchange. The Cd^{2+}/Zn^{2+}-TiO_2 composite was then hydrothermally treated at 120°C with thiourea as the sulfur source to sulfidize the metal ions into a $Cd_{0.65}Zn_{0.35}S$ solid solution. The $Cd_{0.65}Zn_{0.35}S$@titania nanotubes composite was found to be about 8 times more active towards the hydrogen evolution reaction compared to CdS@TiO_2 nanotubes after photoplatinization (2 wt% Pt). They claimed that a strong interphase interaction between the $Cd_{0.65}Zn_{0.35}S$ and the titania nanotubes is the cause of this high hydrogen evolution reaction. The one dimensional tubular structure of the nanotubes provides an effective charge transfer channel for the electrons to efficiently reduce water. It is interesting to note that the hydrogen evolution rate of the $Cd_{0.65}Zn_{0.35}S$@titania nanotubes reaches a maximum after 2.5 hours of irradiation and then stabilized at a lower level. Park and coworkers investigated the effect of platinum loading on the CdS/TiO_2 composites.[90] The hybrid composite was synthesized by dissolving $CdAc_2 \times 2H_2O$ in a Degussa P25 titania dispersion. The Cd^{2+} was then co-precipitated by addition of Na_2S. Later the composite was platinized by photodeposition. Alternatively, the titania was platinized prior to the sulfide deposition. The authors found that platinization of the titania prior to sulfide deposition increased the activity towards the hydrogen evolution reaction by six times in comparison to the platinization of the CdS@TiO_2 hybrid. This is explained by the vectorial transfer of electrons along the pathway $CB_{CdS} \rightarrow CB_{TiO2} \rightarrow Pt$, platinization of the bare titania facilitates this transport of electrons. While platinization of the CdS@TiO_2 composite causes multi directional electron transfer, resulting in losses of the charge carriers and thus hydrogen evolution rate.

Chapter 3: Methodology and theory

3.1 Introduction

In this chapter all the experimental procedures used throughout this thesis are described. These include the synthesis of the silica (SiO_2) and titania (TiO_2) supports and the deposition of the $Cd_xZn_{1-x}S$ by different techniques.

All (loaded) supports were thoroughly characterized. X-ray photoelectron spectroscopy (XPS), nitrogen physisorption, Transmission and Scanning electron microscopy (TEM/SEM), X-ray diffraction (XRD), inductively coupled plasma atomic emission spectroscopy (ICP-AES), and UV-VIS diffuse reflectance spectroscopy (DRS) were employed to characterize the (loaded) supports. In the second part of this chapter a short introduction to the theory of these methods, their relevance to the thesis and the sample preparation for each technique are given.

3.2 Support synthesis procedures

Despite the high activity of the $Cd_xZn_{1-x}S$ photocatalyst under visible light, their suspensions are not stable over a long period of time. The dispersed photocatalyst tends to aggregate which decreases the area exposed to the electrolyte and lowers the hydrogen evolution activity.[65] Therefore several materials were chosen as supports to anchor the $Cd_xZn_{1-x}S$ nanoparticles on the surface and suppress their aggregation. Two types of commonly used support materials were chosen. Firstly silica, which is an insulator that cannot participate in the photocatalytic cycle on itself. More specifically SBA-15 and MCM-41 were chosen as they are highly ordered model mesoporous supports. Secondly, titania was chosen because of its semiconducting properties and high chemical stability.[4-6] Coupling of titania with transition metal sulfides results in a hybrid system in which charge carrier separation can be enhanced through the formed heterojunction.[69, 89, 91, 92] A mesoporous titania support, further referred to as the mesoporous beads, with high surface area was chosen and prepared in accordance to literature.[93] Its high surface area can offer abundant active sites for the hydrogen evolution reaction. Commercially available TiO_2 – Degussa P25 – was used for the comparison with the mesoporous beads.

3.2.1 SBA-15 mesoporous support

Mesoporous SBA-15 was synthesized by three different synthetic routes published in literature. [94-97] The hydrothermal method was applied to synthesize SBA-15 with a mean pore size of ±7 nm. The procedure was adapted to increase the mean pore size to approximately 10 nm by adding 1,3,5-trimethylbenzene (TMB) as a swelling agent. SBA-15 was also prepared by microwave-assisted synthesis to substantially decrease the synthesis time as the convenient hydrothermal treatment requires 48 hours.

Hydrothermal synthesis in the absence of a swelling agent was done according to published procedures.[94, 95] First Pluronic P123 block co-polymer (1.7 g) and NaCl (8.8 g) were dissolved in a 1.6 M HCl solution (75 ml) overnight under vigorous stirring. Subsequently tetramethyl orthosilicate (TMOS; 3.3 g) was added dropwise to the solution under magnetic stirring. Hydrolysis of the silica precursor was immediately observed. The suspension was stirred overnight and then transferred into a Polytetrafluoroethylene(PTFE)-lined stainless steel autoclave and hydrothermally treated at 100 °C for 48 hours. The solid product was separated by centrifugation, washed three times with

demineralized water, once with ethanol, and dried overnight at 110°C. The P123 template was removed by calcination at 600 °C for 6 hours (5 °C/min heating ramp) in O_2/He flow (1:1 ratio).

Hydrothermal synthesis in the presence of 1,3,5-trimethylbenzene was adapted from the procedure reported in literature and was mostly similar to the synthesis described above.[96] Pluronic P123 block co-polymer (4 g) was dissolved in 1.5 M HCl (150 ml) overnight under vigorous stirring at 40 °C without addition of NaCl. To increase the pore sizes, the swelling agent 1,3,5-trimethylbenzene (TMB; 0.42 g) was added and stirred for 4 hours at 40 °C. Subsequently tetraethyl orthosilicate (TEOS; 8.50 g) was added dropwise to the solution and stirred at 40 °C for another 20 hours. Then the mixture was transferred into a PTFE-lined stainless steel autoclave and kept at 100 °C for 24 hours. The product was separated, washed, dried and calcined analogously to the SBA-15 without swelling agent.

Microwave-assisted synthesis was done according to the published procedure.[97] Pluronic P123 block co-polymer (1 g) was dissolved in 1.6 M HCl (37 ml) solution under magnetic stirring overnight. Subsequently TEOS (2.15 ml) was added into the solution under stirring and the obtained mixture was transferred immediately to microwave-compatible high pressure PTFE vessels. The mixture was subjected to several thermal steps by a continuous temperature program. At first, it was heated to 40 °C in 7 minutes (150 W) and kept at that temperature for 2 hours (400 W). Then the temperature was increased to 160 °C in 7 minutes (400 W) and kept for 1 hour (400 W). MW-assisted hydrothermal synthesis was carried out under magnetic stirring. Separation, drying and calcination of the product were identical to the ones for the convenient hydrothermal synthesis described above. The entire synthesis was carried out in a microwave oven (Microsynth, 1.5 kW maximum, by Milestone). The temperature inside the reference vessel was measured with a fiber optical thermometer.

3.2.2 MCM-41 mesoporous support

Mesoporous MCM-41 was synthesized by two different synthetic procedures described in literature. Hydrothermal synthesis was used to synthesize MCM-41 with a mean pore size of approx. 3 nm.[98, 99] A simple co-precipitation under ambient conditions was used to synthesize MCM-41 with a mean pore size of 2 nm.[100]

Hydrothermal synthesis of MCM-41 was adopted from literature.[98, 99] Cetyl trimethylammonium bromide (CTAB; 6 g) was dissolved in demineralized water (37.7 g). When the template (CTAB) was dissolved, tetramethylammonium hydroxide (TMAOH; 9.75 g) was added to the solution under magnetic stirring. Subsequently, silica gel (6.18 g) was added to the solution under vigorous stirring. The dispersion was then transferred into PTFE-lined autoclaves and kept at 135 °C for 48 hours. The precipitate was separated by centrifugation, washed three times with demineralized water and once with ethanol, and dried overnight at 110 °C. The CTAB template was removed by calcination in the O_2/He flow (1:1 ratio): first, the powder was heated up to 270°C (5 °C/min heating ramp) and kept at that temperature for 2 hours; then the temperature was increased to 600°C (5 °C/min heating ramp) and kept for 6 hours.

Co-precipitation synthesis of MCM-41 was done in accordance to the published procedure.[100] CTAB (0.5 g) was dissolved in demineralized water (96 ml) under stirring until a homogeneous solution was obtained. Then ethanol (34 ml) and ammonia (10 ml of 25% solution) were added and stirred for five

more minutes. Subsequently TEOS (2 ml) was added and the mixture was stirred for three hours. The solid was filtered, washed three times with demineralized water, once with ethanol, and dried overnight at 110 °C. The template was then removed by calcination in O_2 flow at 600 °C (5°C/min heating ramp) for six hours.

3.2.3 Mesoporous TiO_2

Mesoporous titania beads were synthesized according to the following procedure.[93] First, hexadecylamine (4.8714 g; HDA) was dissolved in ethanol (800 ml) under magnetic stirring. Then 3.2 ml of 0.1 M aqueous KCl were added. Subsequently titanium tetraisopropoxide (TTIP; 18.10 ml) was added. The mixture was left for 18 hours for aging without stirring. The titania precipitate was filtered off, thoroughly washed with ethanol and dried overnight in a desiccator under vacuum. The obtained HDA+TiO_2 beads underwent a following hydrothermal treatment: 1.6 g of the beads were dispersed in a mixture of ethanol (20 ml) and 0.45 M $NH_{3\,(aq)}$ (10 ml), the suspension was transferred into a PTFE-lined stainless steel autoclave and heated to 160 °C for 18 hours. The solid precipitate was washed three times with demineralized water and once with ethanol and then dried overnight in a desiccator under vacuum. The HDA template was then removed by calcination at 500 °C (2 °C/min heating ramp) for two hours in O_2 flow.

3.3 Loading procedures

We based our initial loading procedures on the hydrothermal synthesis (180°C; 24h; 1M NaAc) of the most active unsupported $Cd_xZn_{1-x}S$. However silica was found not to be stable under the harsh reaction conditions. Hence milder routes were developed for silica-based supports. As titania has a higher chemical stability, it was loaded by the initial loading sequence nonetheless.[4-6]

3.3.1 $Cd_xZn_{1-x}S$ loading by hydrothermal synthesis

In a typical two-step loading about 0.5 g of the titania support was used and loaded by 50 wt% of the $Cd_xZn_{1-x}S$. First $CdAc_2{\times}2H_2O$ (0.55 g) and $ZnAc_2{\times}2H_2O$ (0.46 g) were dissolved in 15 ml of demineralized water. Then 0.5 g of the titania support was dispersed in the solution and evacuated in a desiccator for 30 minutes to remove air from the pores. Subsequently NaOH was used to increase the pH of the solution (up to ≈11) to precipitate Cd^{2+} and Zn^{2+} in the form of $Cd(OH)_2$ and $Zn(OH)_2$. The solid precipitate was washed three times with demineralized water and once with ethanol. Subsequently the $Cd(OH)_2$+$Zn(OH)_2$+support was dispersed in 1M $NaAc_{aq}$ (35 ml) and transferred into a PTFE-lined stainless steel autoclave. Then thioacetamide (0.34 g) was added as the sulfur source. The autoclave was heated to 180°C for 24 hours under tumbling. After the hydrothermal treatment the solid product was separated by centrifugation and the $Cd_xZn_{1-x}S@TiO_2$ particles were washed three times with demineralized water, once with ethanol and dried at 110 °C overnight.

The silica-based supports were found to be unstable during this loading procedure. Therefore the procedure was adapted for these supports. In the adapted procedure, first, about 0.5 g of the silica-based support was dispersed in 15 ml solution of $CdAc_2x2H_2O$ (0.55g) and $ZnAc_2x2H_2O$ (0.46g). The hydroxide step was omitted and the dispersion was hydrothermally treated at 100°C for 5 days under tumbling with thioacetamide (0.34 g) as the sulfur source. After the hydrothermal treatment the solid product was separated by centrifugation and the $Cd_xZn_{1-x}S@SiO_2$ particles were washed three times with demineralized water, once with ethanol and dried at 110 °C overnight.

3.3.2 $Cd_xZn_{1-x}S$ loading of silica by co-precipitation

Due to the chemical instability of the silica-based supports, another mild loading of the photocatalyst by means of co-precipitation of the sulfide was done. During a typical loading about 0.3 g of the silica support was used and loaded by 50 wt% of $Cd_xZn_{1-x}S$. First $CdAc_2{\times}2H_2O$ (0.33 g) and $ZnAc_2{\times}2H_2O$ (0.28 g) were dissolved in demineralized water (30 ml) under magnetic stirring. Then the SiO_2 support (0.3 g) was dispersed in the solution. Subsequently Na_2S (0.71 g dissolved in 10 ml H_2O) was added to the dispersion under vigorous stirring and left for aging for 24 hours. The precipitate was separated by centrifugation, washed three times with demineralized water, once with ethanol and dried overnight at 110 °C.

3.3.3 $Cd_xZn_{1-x}S$ loading via incipient wetness impregnation

To incorporate the loaded photocatalyst in the pores of the support, incipient wetness impregnation of a Cd and Zn precursor in the support was carried out. The supports were impregnated with a solution containing an amount of $CdAc_2{\times}2H_2O$ and $ZnAc_2{\times}2H_2O$. Due to the limited water capacity of the supports and solubility of the metal acetates, 50 wt% loading of $Cd_xZn_{1-x}S$ could not be reached. Therefore a loading of 25 wt% was chosen instead. The impregnated supports were dried overnight at 110 °C. The metal precursor was converted into $Cd_xZn_{1-x}S$ by three different synthetic procedures depending on the support. The impregnated silica supports (0.2 g) were dispersed in a Na_2S aqueous solution (0.1 g Na_2S in 5 ml H_2O) to convert the precursor into the sulfide, similarly to the co-precipitation procedure. Therefore this technique will be further referred to as "IWI co-precipitation". The impregnated titania supports (0.2 g) were dispersed in a 1M NaAc aqueous solution (35 ml) containing thioacetamide (0.1 g) as the sulfur source. The suspension was then hydrothermally treated at 180 °C under tumbling. This technique is similar to the hydrothermal procedure used for the titania supports, therefore we will refer to it as "IWI hydrothermal" hereafter. The precursor impregnated in the supports (both silica and titania; 0.2 g) was also converted to the sulfide by *in-situ* generated H_2S. A PTFE-lined stainless steel autoclave was therefore divided into two compartments, one containing the impregnated support, the other a small amount of water (5 ml) and thioacetamide (0.5 g), see appendix A.1. The autoclave was then heated to 100 °C to hydrolyse the thioacetamide and form a H_2S-rich atmosphere that can sulfidize the metal precursor. This technique is referred to as "IWI H_2S" hereafter. All loaded supports were separated by centrifugation, washed three times with demineralized water, once with ethanol and dried at 110°C overnight.

3.4 Catalyst characterization

3.4.1 Transmission and Scanning electron microscopy (TEM & SEM)

3.4.1.1 Transmission and Scanning electron microscopy (TEM & SEM) theory

Electron microscopy is a powerful technique to visualize materials at the nanoscale. It can be used to determine the particle size, shape, spatial distribution of elements and phases (in the case of composites), etc. The basic principles of electron microscopy are quite simple to understand. An electron beam is generated by accelerating electrons from a filament (usually W or LaB_6) in an electric field (for TEM around 100-300kV, for SEM around 20kV). The beam is led through a set of electromagnetic lenses to create a parallel bundle which is then directed towards the sample. The interaction of the incident electrons with the sample may result in several phenomena. The electrons can pass through the sample (transmission), diffract, backscatter, or generate secondary electrons.

Heavier elements interact more intense with the incident beam and can thus be differentiated from lighter elements in the generated images. [20, 101]

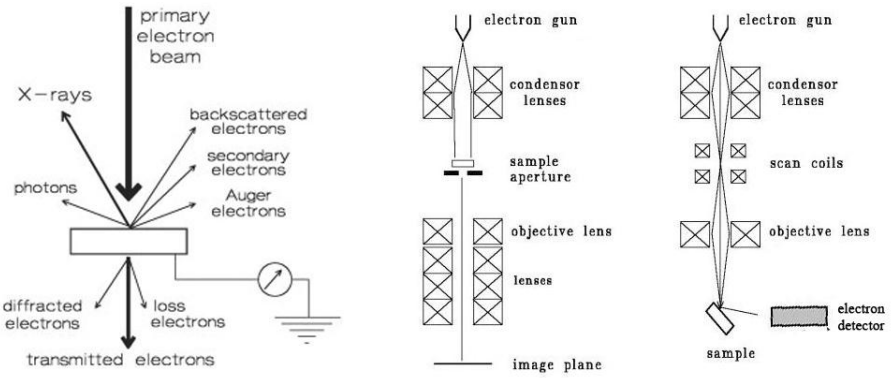

Figure 16: (left) Interaction of the primary electron beam with the sample. (middle) Schematic representation of a TEM setup. (right) Schematic representation of a SEM setup.[20]

Transmission electron microscopy is based upon the transmission of incident electrons. Contrast in bright field TEM images is generated by the attenuation of the transmitted beam. Heavier elements or thicker sections of the sample backscatter more electrons resulting in a darker coloration. Dark field TEM is based upon the diffraction of the incident electrons and thus shows heavier elements as brighter spots on the image. The TEM generates an image of the two dimensional projection of the sample. Limitation of TEM is that it requires thin samples or small particles to allow transmission.[20]

In contrast to TEM, scanning electron microscopy (SEM) is based on the backscattered or secondary electrons and provides information over the morphology and topology of the samples. The backscattered electrons are elastically scattered high energy electrons. The heavier elements in the sample can backscatter the incident electrons more intensively in comparison to the light ones, which results in a contrast in the image. When the secondary electrons are detected, an image of the surface can be generated. Contrast of the image arises from the orientation and the position of the scattering surfaces: sections of the sample closer to the detector appear brighter and further sections become gradually darker. Therefore the surface morphology can be studied in more detail.[20]

3.4.1.2 TEM & SEM sample preparation

TEM images were acquired to investigate particle size, morphology and spatial distribution of the photocatalyst on the support. The samples were suspended in ethanol by sonication and dispersed over a copper grid with a holey carbon film. TEM images were recorded on a FEI Tecnai 20 (type Sphera) electron microscope equipped with a LaB_6 filament and operated at 200kV.

SEM images were taken to study the morphology of the supports and photocatalysts on the support on the FEI Quanta Scanning Electron Microscope (ESEM) equipped with the secondary electron detector and operated at 5 kV acceleration voltage. The samples were prepared by applying a dry powder on an aluminium stopper with attached conducting carbon tape or by drop-casting a suspension of polystyrene beads with the subsequent evaporation of the solvent.

3.4.2 Powder XRD

3.4.2.1 Powder XRD theory

Powder X-Ray diffraction is a technique utilized to study the crystallinity, particle size, shape, crystal phases of materials. It can provide information on the crystal structure, interplanar distances, structure on the mesoscale (small angle XRD). X-ray diffractometers are used to collect diffraction patterns of the powder samples. X-ray tubes are usually used as the X-ray source in the laboratory instruments. In these tubes the X-rays are generated upon (in)elastic scattering of high-energy electrons (30-50kV range) on a metal plate (anode). Fast deceleration of the electrons and their interaction with the core electrons of the atoms comprising the anode results in generation of bremsstrahlung and strong spectral lines respectively. Copper and molybdenum are common anode materials used in the laboratory X-ray tubes. Typically the Cu K_α ($K_{\alpha1}$ and $K_{\alpha2}$) spectral line is used and Cu K_β is removed by means of a monochromator or a Ni filter. The X-ray beam passes through the optical elements (primary Soller slit, Divergence slit) and is then directed on the sample. The beam can be diffracted by the sample depending on its crystallinity and phase composition. For a certain set of Bragg planes with indices [hkl] diffraction can occur when the Bragg's law (3.1) is satisfied, with the interplanar distance of the diffracting plane d_{hkl}, the wavelength of the incident X-ray λ, a constant n and the angle of incidence of the X-rays Θ.[102]

$$2d_{hkl}\sin\Theta = n\lambda \tag{3.1}$$

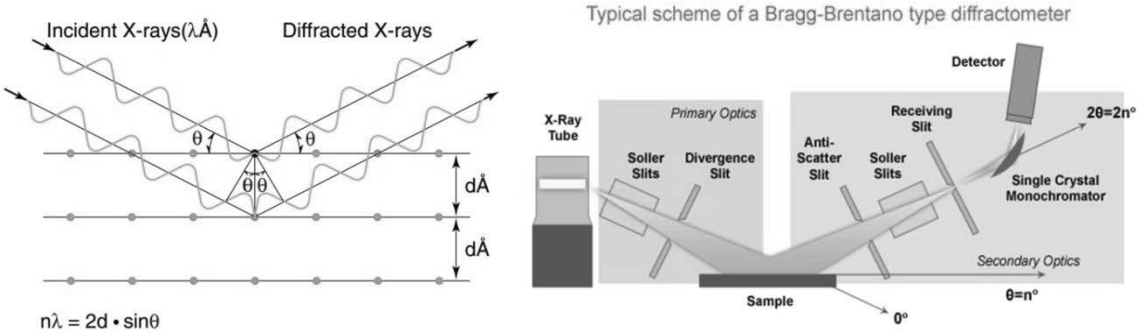

Figure 17: (left) Illustration of Bragg's law by diffraction of the incident X-rays. (right) Schematical setup of a Bragg-Brentano type diffractometer.[103]

In a Bragg-Brentano type diffractometer both the X-ray tube and the detector are placed on a goniometer and precisely move in steps with regard to the sample. The primary beam makes an angle of 2Θ with respect to the diffracted X-rays to the detector. The measured intensity is plotted versus the 2Θ angle in the diffractogram. XRD is a fingerprint technique, based on the experimental diffraction pattern, the crystal phase and substance can be identified. The interplanar distances can be derived from the Bragg's law and ascribed to the crystal planes.

3.4.2.2 Powder XRD sample preparation

Samples for powder XRD were prepared as follows. First, they were carefully grinded in the mortar if the powder was too coarse. The fine sample powder was then pressed into the cavity of a standard stainless steel sample holder. A zero background etched silicon wafer was used only if a small amount of sample was available. The XRD diffractograms were measured on a Bruker Phaser D2 diffractometer using Cu K_α line. Wide angle diffractograms were measured in the region from

10 to 60° using a 3 mm anti-scatter slit and 1 mm divergence slit. A step size of 0.032° and 0.5 s/step were used. Small angle diffractograms were measured using a 0.5 mm anti-scatter slit and 0.1 mm divergence slit. A 2Θ range of 0.7 to 4.5° or 0.7 to 10° was recorded with 0.002° step size and 0.5 s/step acquisition time. The reference patterns of the $Cd_{0.5}Zn_{0.5}S$ phase were not available in the PDF database (PDF-2) thus we calculated the interplanar distances for the cubic and hexagonal phases of the solid solution based on the Vegard's law: by averaging the interplanar distances of pure CdS and ZnS hexagonal and cubic phases. The following PDF files were used: cubic CdS - 01-089-0440, hexagonal CdS - 01-074-9663, cubic ZnS - 00-005-0566, and hexagonal ZnS – 00-010-0434.

3.4.3 Physisorption

3.4.3.1 Physisorption theory

Physisorption is a technique used to determine the surface area, pore diameter, pore volume, type of pores, etc. of porous materials.[104] It is based upon the adsorption of gas molecules onto the material's surface. Nitrogen is typically used as the adsorbate to probe the properties of mesoporous materials (2-50 nm pores). First the adsorbates (water, alcohols, hydrocarbons etc.) are removed from the sample surface via a thermal treatment at elevated temperature under nitrogen gas flow. Afterwards, the sample tube was placed in the device, evacuated, and cooled by liquid nitrogen to -196 °C. Then N_2 gas is supplied to the sample through the manifold in small steps (to allow equilibration). At each step the amount of adsorbed nitrogen is determined as well as the pressure in the sample tube. Physisorption isotherms are then generated by plotting the amount of adsorbed nitrogen against the relative pressure (the absolute pressure divided by the saturation pressure). The surface area, pore volume and pore size distribution was determined from the isotherms by the BET (Brunnauer-Emmett-Teller) and BJH (Barret-Joyner-Halenda) methods respectively.[105, 106]

3.4.3.2 Physisorption sample preparation

First 100-200 mg of the sample was loaded in a sample tube. Then the sample was treated at 120°C for 3 or more hours under N_2 flow. Subsequently the sample tubes were placed in the device for analysis. Surface area, pore volume and pore sizes were determined on a Micromeretics Tristar II 3020 V1.03 system with N_2 physisorption at -196 °C. Analysis of the isotherms was performed using the BET method for the surface area and the BJH method for the pore volume. The mean pore size was determined from the pore size distribution.

3.4.4 UV/VIS diffuse reflectance spectroscopy

3.4.4.1 UV/VIS diffuse reflectance spectroscopy theory

UV/VIS diffuse reflectance spectroscopy (DRS) can be used to determine the band gap of solid materials and is closely related to UV/VIS absorption spectroscopy. In diffuse reflectance spectroscopy, a material is irradiated with a beam of light and the relative amount of light that is reflected by the surface is measured. Semiconducting powders can absorb a fraction of the incident photons depending on the band gap of the material. Therefore the reflectance at particular wavelengths decreases with respect to a reference with reflectance close to 1 (e.g. $BaSO_4$) and a DRS spectrum is recorded.

UV/VIS DRS spectra are measured on a UV/VIS spectrophotometer with a diffuse reflectance accessory. Usually an integrating sphere (a sphere internally coated with a reference material, typically $BaSO_4$, with the reflectance close to 1) is used to measure the diffuse reflected flux.

Measurements are usually conducted under the so-called "directional-specific hemispherical reflectance" geometry, see Figure 18.[107] The sample is directly illuminated by the incident light and the reflected light is directed towards the detector by the integrated sphere. Other geometries are possible as well. A DRS spectrum is recorded by plotting the reflectance against the photon energy. The band gap can be determined by converting the DRS spectrum with the Kubelka-Munk function, see formula (3.2) with *R* defined as the reflectance (fraction). Then $(h\nu F(R_\infty))^{1/n}$ is plotted against the photon energy hν in the Tauc plot. The value for n depends on the nature of the transition. It takes values of 0.5 and 1.5 for the direct allowed and forbidden transitions or 2 and 3 for indirect allowed and forbidden transitions respectively.[108] The linear region of the Tauc plot can be extrapolated and the intersect with the horizontal axis yields the band gap E_g.[108, 109]

$$F(R_\infty(\lambda)) = \frac{(1-R(\lambda))^2}{2R(\lambda)} \tag{3.2}$$

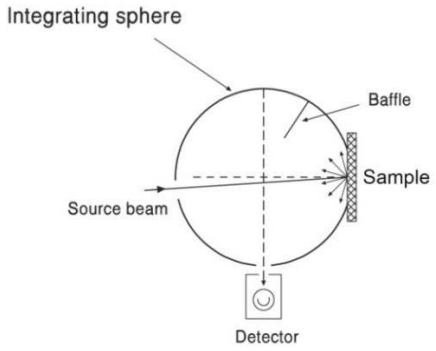

Figure 18: Integrating sphere and light flux pathway in a directional-specific hemispherical reflectance geometry.[107]

3.4.4.2 UV/VIS diffuse reflectance spectroscopy sample preparation

We prepared samples for UV/VIS diffuse reflectance spectroscopy (UV/VIS DRS) by pressing the powder in the cavity of the sample holder to obtain a flat surface. The DRS spectra were measured on a Shimadzu UV-2401PC spectrophotometer equipped with an integrating sphere. The spectra were recorded in the spectral range from 190 to 600 nm using D_2 and a halogen lamps as the light source, a slit size was set to the value which corresponded to the 2 nm region of the optical spectrum, and 0.5 nm/step. When the amount of powder was insufficient to do measurements on Shimadzu UV-2401PC, an Avaspec-2048 fiber optics spectrophotometer and an integrating sphere accessory were used. An Avalight-DHS light source was used for these measurements. The powder was flattened between two microscope slides with the integrating sphere placed on top. $BaSO_4$ was used as a reference for all DRS measurements. The obtained DRS spectra were converted into the Kubelka-Munk function and used for the Tauc plot to determine the band gap of the sample.

3.4.5 X-ray photoelectron spectroscopy

3.4.5.1 X-ray photoelectron spectroscopy theory

X-ray photoelectron spectroscopy (XPS) is a surface-sensitive technique that provides information over the elements present in the sample, i.e. their relative amounts and oxidation states. The technique is based on the photoelectric effect. A monochromated X-ray source is used to irradiate the sample with X-ray photons with energy hν under ultra-high vacuum conditions. Interaction of the

incident X-rays are with the core-level and valance electrons in the top 0-10 nm of the material results in emission of photo and Auger electrons from the sample. In the case of photoelectrons their kinetic energy E_{kin} can be converted into the binding energy of the electrons E_{bin} (which is element and chemical environment specific). The relationship between the kinetic (E_{kin}) and binding (E_{bin}) energy of the photoelectrons, work function of the detector (ϕ), and energy of incidents photons $h\nu$ is given by equation (3.3).[20]

$$E_{bin} = h\nu - E_{kin} - \varphi \tag{3.3}$$

These binding energies are characteristic for the elements and chemical environment and can be used for elemental analysis of the surface. The intensity of the emitted photoelectrons of a specific element is measured which is proportional to the surface concentration of the element. The surface composition can thus be estimated by integration of the area under the XPS peaks. As heavier elements interact more intensively with the incident X-ray beam, sensitivity factors are needed to correct the integrated intensities and obtain the correct surface concentrations.[110] A higher oxidation state results in a higher binding energy in most cases.[20]

3.4.5.2 X-ray photoelectron spectroscopy sample preparation

XPS measurements were carried out to determine the surface composition and the binding energies of the elements of the samples. The (loaded) supports were analyzed using a K-Alpha XPS spectrometer by Thermo Scientific equipped with an aluminum anode (Al-Kα = 1486.68 eV) and a monochromator. The spectra were measured with 15 scans and 0.1 eV resolution in the Si, Ti, O, Cd, Zn, S, Pt regions depending on the used support. The binding energies of all spectra were calibrated using the C 1s (C-C) 284.8 eV peak of adventitious carbon and fitted using a Shirley background in CasaXPS (v.2.3.16 PR 1.6). The binding models used for each element are given in appendix A.2.

3.4.6 Inductively coupled plasma atomic emission spectroscopy

3.4.6.1 Inductively coupled plasma atomic emission spectroscopy theory

Inductively coupled plasma atomic emission spectroscopy (ICP-AES) is a technique used to analyze the elemental composition of the materials. For analysis, the materials are dissolved. The obtained solutions are nebulized and then led through an argon plasma (6000-10000 K). The plasma is generated through electromagnetic induction with a copper coil and a radio frequency (RF) generator. The plasma atomizes the sample and excites the atoms. The excited atoms relax back by releasing photons with specific energies that are detected by the optical system. These energies are characteristic for each element. The emission intensity scales with the concentration of the element in the sample and can be used to determine its content in the sample after calibration with solutions of known concentrations.[111]

3.4.6.2 Inductively coupled plasma atomic emission spectroscopy sample preparation

For the analysis, the materials were treated with 65% HNO_3 at elevated temperatures (70°C) under magnetic stirring to dissolve the deposited mixed sulfides. The reference samples were prepared by dissolving silica-supported samples in a mixture of HF and HNO_3 and smelting TiO_2-supported sample with sodium peroxodisulfate. The metal content of the reference was in good agreement with the content of metals found in the samples treated with HNO_3 only. Thus the latter was considered as a treatment suitable for the complete dissolution of the mixed sulfides. The platinized samples were treated with aqua regia under magnetic stirring at elevated temperatures. Calibration curves of the

Cd and Zn were measured by diluting the standard solution (100 mg/l) and addition of HNO_3, HF, or HCl in the amounts equivalent to the samples. Signals were recorded for the following spectral lines: 214.438 and 226.502 nm for Cd, 213.856 and 206.200 nm for Zn, and 177.708 and 299.797 nm for Pt on a SPECTRO BLUE ICP-AES system. For the calculation of the sulfide loading, we assumed that the ratio of metals (cadmium+zinc) to sulfur was 1.

3.5 Photocatalytic test

Photocatalytic tests were conducted to determine the activities of the (un)supported photocatalysts towards the hydrogen evolution reaction. Typically 10 mg of unsupported, 20 mg of supported (50 wt%), or 40 mg of supported (25 wt%) $Cd_xZn_{1-x}S$ was dispersed by sonication in 50 ml of sacrificial reactant solution (0.25 M Na_2S and 0.35 M Na_2SO_3) to obtain a 0.2 g/l photocatalyst concentration based on nominal loading. The dispersion was transferred into the test cell and magnetically stirred at 500 rpm during the photocatalytic test. The dissolved air was removed by evacuation for 10-15 minutes prior to each test. The test cell was illuminated by a collimated UV/VIS light beam from a Hg(Xe) DC arc lamp (500W, Newport). The infrared and UV spectral regions were removed by a water filter and long-pass (420 nm cut-on wavelength) filter respectively. A controller unit was used to keep the power output of the lamp constant during and in between experiments. The gaseous products were sampled by an automated valve system from the headspace (every 12 or 4 minutes depending on the activity of the samples) and were injected to the GC-TCD-unit (ATI Unicam 600 series, Shin carbon Column (Restek), N_2 carrier gas). Initial hydrogen evolution rates were determined for the (un)supported photocatalyst by plotting the produced amount against time. The GC-unit was calibrated with H_2 prior to experiments. A schematic of the photocatalytic setup is given in appendix B.

Chapter 4: $Cd_xZn_{1-x}S$ on silica supports

4.1 Results & discussion

4.1.1 Characterization of SiO_2 supports

Support	Synthetic route	Swelling Agent	Mean $Ø_{pore}$ (nm)	V_{BJH} (cm^3/g)	S_{BET} (m^2/g)
SBA-15	Microwave	/	10.9	1.04	482
	Hydrothermal	/	6.6	0.77	662
			7.8	0.90	774
			7.6	0.76	503
			6.7	0.71	546
	Hydrothermal	TMB	9.8	0.99	866
			10.0	0.82	871
MCM-41	Co-precipitation	/	2.1	0.89	1347
	Hydrothermal	/	3.1	0.53	529
			3.3	0.78	814
			2.7	0.95	1089

Table 1: Summary of N_2 physisorption data for all SBA-15 and MCM-41 supports. Mean pore diameters are determined based on pore size distribution, pore volume was determined by the Barret-Joyner-Halenda (BJH) method and surface area was determined by the Brunauer-Emmet-Teller (BET) method. The adsorption branch was used for all values. Multiple rows indicate values for different batches of the material prepared by the same synthesis procedure.

Table 1 summarizes the results of physisorption measurements of all silica supports. First, the SBA-15 prepared without swelling agent (TMB) displayed a mean pore diameter of 7.2±0.6 nm, 0.79±0.08 cm^3/g pore volume and a BET surface area of 621±122 m^2/g. Introduction of TMB as a swelling agent increased the mean pore diameter of the SBA-15 by almost 3 nm. The pore volume was found to be slightly higher (0.91±0.12 cm^3/g), while the surface area increased to 869±4 cm^2/g. Microwave-assisted synthesis yielded the largest mean pore size of 10.9 nm and pore volume of 1.04 cm^3/g but lower BET surface areas of 482 m^2/g. MCM-41 is, like SBA-15, typically synthesized via a hydrothermal route.[94, 112, 113] The pore volume of 0.75±0.21 cm^3/g and surface area of 810±280 m^2/g are comparable to SBA-15. The mean pore diameter was much smaller, around 3.0±0.3 nm. Synthesis of MCM-41 by co-precipitation yielded the highest BET surface area of 1347 m^2/g and a pore volume of 0.89 cm^3, comparable to the hydrothermal synthesis. The mean pore diameter was found to be 2.1 nm, which is close to the detection limit of the Micromeretics Tristar II 3020 V1.03 system.

Pore size distributions and nitrogen adsorption/desorption isotherms of the SBA-15 and MCM-41 supports are given in Figure 19. We observed that pore size distributions of all the samples were quite narrow which indicated a well-defined mesoporous structure. The pore size distribution of MCM-41 prepared by co-precipitation cannot be fully shown being at the detection limit of the instrument. This is also reflected in the absence of hysteresis in the corresponding isotherm. For this sample argon physisorption may be more suitable. The other isotherms displayed a typical type IV isotherms shape characteristic for mesoporous materials with high adsorption energy (e.g. silica).[104]

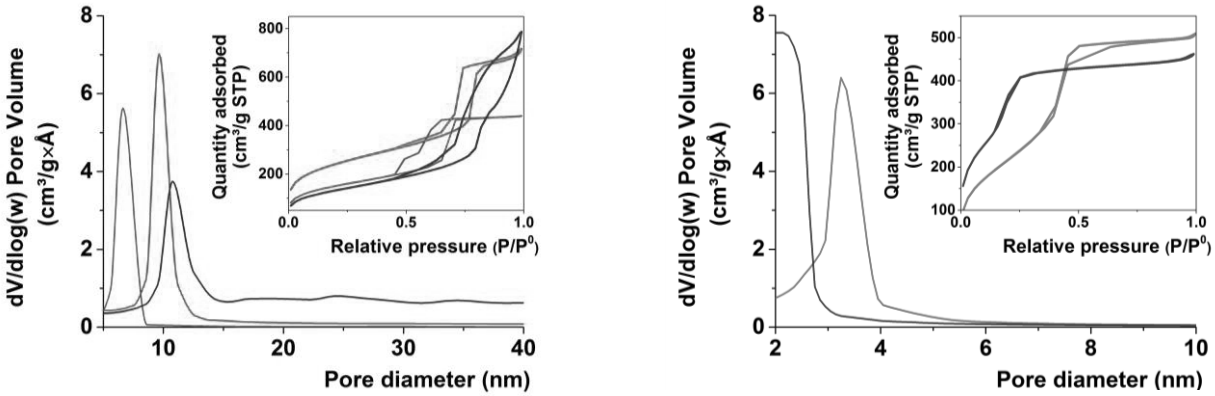

Figure 19: (left) Pore size distributions and N_2 physisorption isotherms of SBA-15 prepared by ***microwave assisted***, ***hydrothermal*** and ***TMB-hydrothermal*** synthesis. (right) Pore size distributions and N_2 physisorption isotherms of MCM-41 prepared by ***co-precipitation*** and ***hydrothermal*** synthesis.

Small angle XRD was conducted to confirm the formation of long range ordered SBA-15 and MCM-41. Due to their hexagonal porous structure, both supports belong to the hexagonal P6mm space group. [94, 95, 114-116] All SBA-15 XRD patterns showed the primary (100), secondary (110) and tertiary (200) reflections, see Figure 20. From these reflections we could extract the lattice constant '*a*' by applying formula (4.1) (Miller index l=0).[117] The position of higher (hkl) reflections can be estimated by inserting the miller indices in formula (4.2). The 2Θ values of the (210) and (300) reflections were calculated and compared with the obtained XRD pattern. Careful analysis of the XRD patterns revealed the presence, albeit very weakly, of these higher reflections, see Table 2 and Figure 20. This indicated the formation of well-defined long range ordered SBA-15. Both MCM-41 supports clearly displayed first three reflections as well. The position of the higher reflections – (210) and (300) – were also estimated but could not be clearly seen in the diffractogram. The signal-to-noise ratio was too low to assign the reflections with high certainty.

$$a = \sqrt{\frac{4}{3}\left(\frac{h^2+hk+k^2}{\frac{1}{d^2}-\frac{l^2}{c^2}}\right)} = \sqrt{\frac{4}{3}(h^2+hk+k^2)\cdot d^2} \qquad (4.1)$$

$$2\theta_{hkl} = 2\sin^{-1}\left(\frac{0.15418}{2\sqrt{\frac{3}{4}\frac{a^2}{(h^2+hk+k^2)}}}\right) \qquad (4.2)$$

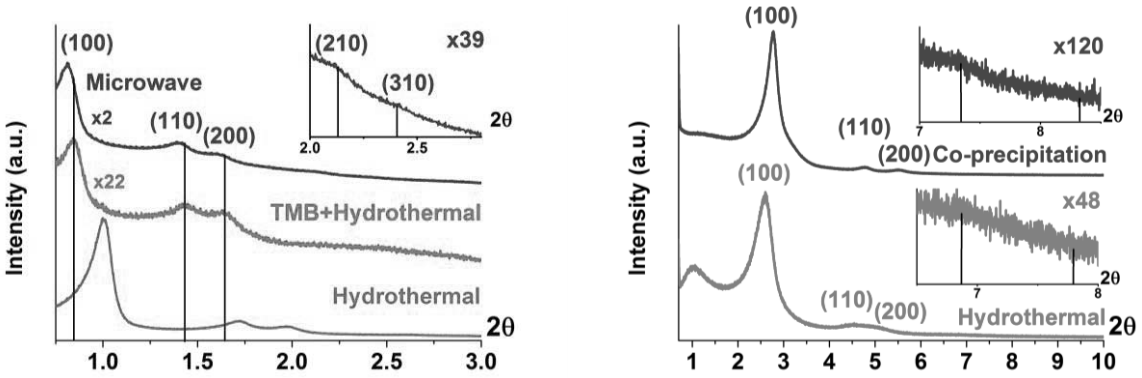

Figure 20: Small angle XRD patterns of (left) SBA-15 synthesized by ***microwave assisted***, ***hydrothermal,*** and ***TMB + hydrothermal*** synthesis. Inset of microwave assisted synthesis between 2 and 2.8 degrees. The signals were normalized to the intensity of the main reflection of the hydrothermal sample. (right) MCM-41 synthesized by ***co-precipitation*** and ***hydrothermal*** synthesis.

	Synthetic procedure	**$2\theta_{(100)}$**	**$2\theta_{(110)}$**	**$2\theta_{(200)}$**	**$a_{(100)}$**	**$2\theta_{(210)}$ Predicted**	**$2\theta_{(210)}$ Experimental**	**$2\theta_{(300)}$ Predicted**	**$2\theta_{(300)}$ Experimental**
SBA-15	Microwave	0.813	1.403	1.606	12.547	2.151	2.116	2.439	2.411
	Hydrothermal	1.018	1.721	1.975	10.020	2.694	2.603	3.054	2.913
	TMB-Hydothermal	0.856	1.438	1.632	11.917	2.265	2.286	2.568	2.433
MCM-41	Co-precipitation	2.768	4.777	5.519	3.685	7.339	/	8.32	/
	Hydrothermal	2.598	4.541	4.951	3.927	6.877	/	7.799	/

Table 2: Summary of measured and predicted 2θ angles for the first five reflections of hexagonal SBA-15 and MCM-41. The lattice parameter '*a*' is calculated based on the (100) reflection.

The data obtained from the XRD patterns were in good correlation with the results of nitrogen physisorption. Comparison of the lattice constants reveals that $a_{Microwave} > a_{Hydrothermal} > a_{TMB+Hydrothermal}$, and the same sequence was found for the mean pore sizes. For the MCM-41 supports both methods were in good agreement with each other as well.

Finally, TEM images were taken to further confirm the formation of the porous hexagonally structured SBA-15 and MCM-41. Well-ordered 1D straight channels can be easily seen in Figure 21. The distance between the channel walls, corresponding to the lattice constant $a_{(100)}$ determined from the XRD, was also determined. For SBA-15, the distance was found to be 10.7 nm for the microwave assisted synthesis, 8.8 nm for the hydrothermal synthesis, and 10.4 nm for the hydrothermal + TMB synthesis. For MCM-41 this value was found to be 2.9 nm for the co-precipitation and 3.4 nm for the hydrothermal synthesis.

In summary, the results of the XRD, nitrogen physisorption, and TEM analysis were in good agreement. This allowed us to conclude that we synthesized highly ordered SBA-15 and MCM-41.

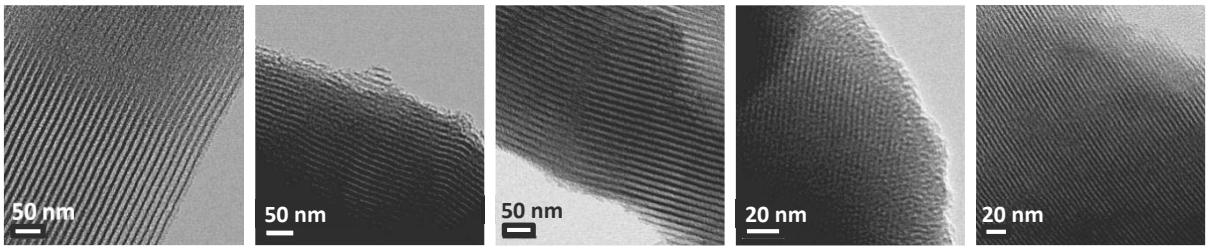

Figure 21: TEM images of SBA-15 and MCM-41. SBA-15 by (1) microwave assisted, (2) hydrothermal, and (3) TMB+hydrothermal synthesis. MCM-41 by (4) co-precipitation, and (5) hydrothermal synthesis.

4.1.2 Loading of SBA-15 and MCM-41 with $Cd_{0.5}Zn_{0.5}S$

4.1.2.1 Two-step hydrothermal loading of SBA-15

Initially we tried to load SBA-15 via a synthetic route that yields the most active unsupported $Cd_{0.5}Zn_{0.5}S$. In this method an aqueous solution of Cd^{2+} and Zn^{2+} acetates was prepared. Subsequently, the support was dispersed in this solution and the pH was adjusted to approximately 11 by addition of NaOH (1 M). This resulted in the precipitation of the mixture of $Cd(OH)_2$ and $Zn(OH)_2$. Then the insoluble hydroxides were converted into sulfides under a hydrothermal treatment (180°C, in 1.0M NaAc, 24 hours) with thioacetamide as the sulfur source. Wide angle XRD showed the presence of well-defined $Cd_{0.5}Zn_{0.5}S$ phase and amorphous silica, see Figure 22 left. Further characterization of this composite indicated the loss of the support's mesostructure. All small angle XRD reflections were gone and the pore size distribution extracted from the physisorption data no longer had the characteristic narrow peak, see Figure 22 left. The shape of the adsorption isotherm of the samples resembled a type II isotherm, characteristic for non-porous or macroporous materials with a high heat of adsorption E_{ad} (e.g. silica).[104] The surface area (S_{BET} = 23 m^2/g) was close to the value obtained for the unsupported $Cd_{0.5}Zn_{0.5}S$ (S_{BET} = 17 m^2/g). All this data indicated a complete loss or the support's mesostructure. Silica on itself was not completely dissolved as the signal arising from the amorphous phase could still be seen in the XRD pattern, see Figure 22 left.

Hence, it was evident that SBA-15 was not stable under the hydrothermal conditions of sulfide deposition. The collapse of the mesostructure may originate from several causes: high pH at the step of the hydroxide precipitation or a lack of hydrothermal stability at 180°C. The intermediate step of the hydroxide precipitation was most certainly one cause. During another experiment, we observed that silica was dissolved when we accidentally added an excess of NaOH. The hydrothermal step may also corrupt the mesostructure. In literature SBA-15 is seen as a relatively stable compound under hydrothermal conditions.[95] Nevertheless we tested the stability of our SBA-15 under the sulfidation conditions. The SBA-15 (TMB + hydrothermal) was dispersed in H_2O, 1M $NaAc_{aq}$, H_2O + thioacetamide, and 1 M $NaAc_{aq}$ + thioacetamide and hydrothermally treated at 180°C. Nitrogen physisorption indicated the loss of the ordered mesoporous structure as the pore size distribution was no longer present in either of the treated supports, see Figure 22 right. Treatment in H_2O broadened the pore size distribution and increased the surface area and pore volume. The remnants of the previously well-ordered pores can still be seen on TEM images, see appendix C.1. Treatment in 1M $NaAc_{aq}$ resulted in a complete disappearance of any distinct features in the pore size distribution. Also the pore volume and surface area decreased substantially in comparison with the H_2O treated support, see appendix C.1. Further degradation of the mesostructure, in either H_2O or 1M $NaAc_{aq}$, was found when thioacetamide was added.

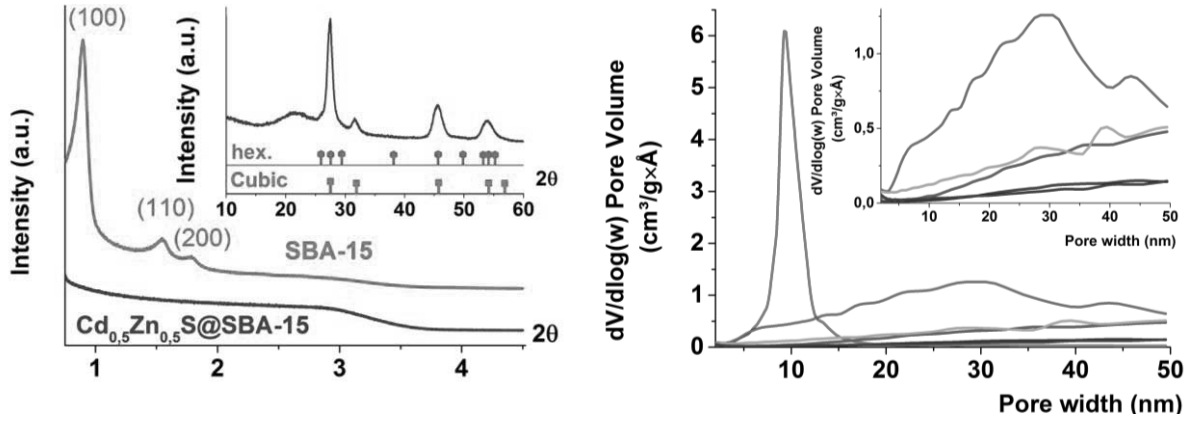

Figure 22: (left) Small and wide angle XRD pattern of ***SBA-15*** and ***$Cd_xZn_{1-x}S$@SBA-15*** by two step hydrothermal synthesis at 180°C. Red and green drop lines indicate the $Cd_{0.5}Zn_{0.5}S$ reflections predicted by Vegards law of cubic and hexagonal phase respectively. (right) Pore size distribution of ***SBA-15***, ***$Cd_{0.5}Zn_{0.5}S$@SBA-15 (Two-step hydrothermal)***, hydrothermally treated SBA-15 in ***H_2O***, ***H_2O+Thioacetamide***, ***1M NaAc***, and ***1M NaAc+Thioacetamide***.

This synthetic procedure was not applied for MCM-41 as it has a lower hydrothermal stability than SBA-15 due to thinner walls.[118] This implies that MCM-41 can be expected not to resist these harsh conditions and loose its mesoporous structure as well. With the abovementioned results we concluded that the two step hydrothermal synthesis of $Cd_xZn_{1-x}S$ is not a viable option for silica supports and milder loading routes are needed to preserve the ordered mesoporous structure.

4.1.2.2 Loading of SBA-15 and MCM-41 by milder synthetic routes

The low stability of SBA-15 and MCM-41 limits possible loading routes for the active photocatalyst. Therefore we developed milder routes to retain the mesostructure of the support during loading. Macías-Sánchez et al. reported the loading of SBA-15 by simple co-precipitation at room temperature without further treatment. In their work the SBA-15 support was dispersed in the mixed solution of cadmium and zinc acetates and Na_2S_{aq} was used as a precipitation agent.[3] We used a similar technique to load the SBA-15 and MCM-41 supports with 50 wt% of the photocatalyst. This synthetic procedure will be referred to as co-precipitation. An alternative incipient wetness impregnation route was implied to ensure deposition of the sulfide phase on the silica support. Due to the solubility of the acetates, 50 wt % loading – used in the other loading procedures – was not possible and 25 wt % was chosen instead. First, the supports were impregnated with the mixed solution of metal acetates and dried to remove the solvent. Then the salts were converted into sulfides by dispersing the impregnated support in a Na_2S solution, this loading procedure is further referred to as IWI co-precipitation.

Besides co-precipitation we developed another mild loading method. As both SBA-15 and MCM-41 are not very stable under hydrothermal conditions, we tried sulfidation of the precursor by *in situ* generated H_2S gas in an autoclave. For this purpose the autoclave was divided in two compartments, one containing the impregnated support, the other a small amount of water and thioacetamide, see appendix A.1. Upon heating, the thioacetamide gets hydrolyzed, releasing H_2S gas that can convert the metal acetates into the sulfide photocatalyst. This can circumvent the hydrothermal instability, however certain amounts of steam are still present.

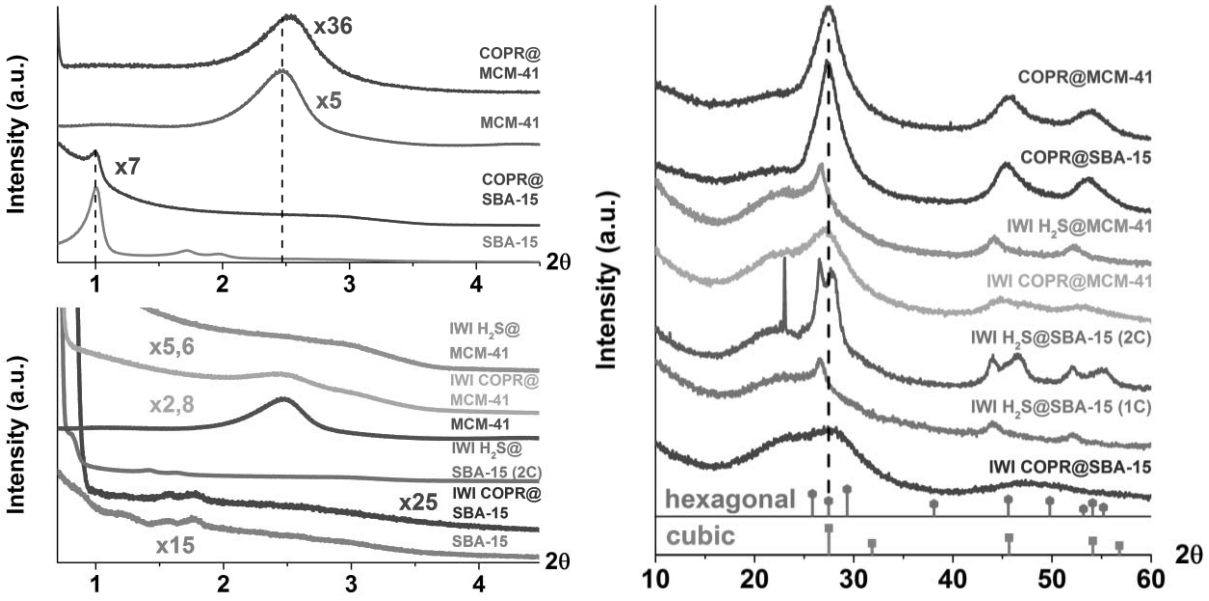

Figure 23 (top left) Small angle XRD patterns of ***SBA-15***, ***MCM-41***, ***COPR@SBA-15***, and ***COPR@MCM-41***. (bottom left) Small angle XRD patterns of ***SBA-15***, ***IWI COPR@SBA-15***, ***IWI H_2S@SBA-15 after 2 cycles***, ***MCM-41***, ***IWI COPR@MCM-41***, and ***IWI H_2S@MCM-41***. (right) Wide angle XRD of the corresponding loaded SBA-15 and MCM-41 by co-precipitation, IWI co-precipitation, and IWI H_2S. The XRD pattern of ***IWI H_2S@SBA-15 after the first cycle*** is also shown. Red and green droplines represent cubic and hexagonal phase of $Cd_{0.5}Zn_{0.5}S$.

Small angle XRD was used to assess the stability of the supports during the sulfide deposition. In the small angle XRD patterns of the supports loaded by the co-precipitation method, the first reflections of the SBA-15 and MCM-41 can still be seen, while the higher reflections of SBA-15 – (110) and (200) – were lost, see Figure 23 left top. The position of the primary reflection was retained, which indicated no further shrinking of the SBA-15 framework. In the case of MCM-41 the primary reflection slightly shifted to a higher angle. MCM-41 was synthesized in high pH solutions so it is possible that the high pH, from a slight excess of Na_2S, induced further shrinkage. Similarly to the co-precipitation, the SBA-15 mesostructure was also retained during the IWI co-precipitation and IWI H_2S procedures, see Figure 23 left bottom. The reflections of the SBA-15 loaded by the IWI H_2S procedure (after a second treatment step) however shifted to lower angles. This finding was in a good agreement with the higher mean pore size estimated from the physisorption data, see Figure 24 left. Therefore the SBA-15 channels must have increased in size as thinning of the wall can explain the higher mean pore size but not the increase of the lattice constant *a*. The mean pore size of the loaded sample (11.4 nm) was also larger than the lattice constant $a_{(100)}$ of the bare support (10.0 nm), see Figure 24 left. The reason for this increase of the framework size is unclear. In the case of MCM-41, the XRD pattern of the IWI co-precipitation sample showed the primary reflection at the same position as the fresh support but no distinct features can be differentiated in the diffractogram of the IWI H_2S loaded support. For all loaded SBA-15 and MCM-41 we saw that the intensity of the signals is weakened – mind the multiplication factor – compared to the bare supports. This can be explained by the presence of heavy elements like cadmium and zinc in the loaded samples. These elements scatter the X-rays stronger due to higher electron density and therefore can lower the signal of the lighter silica support.

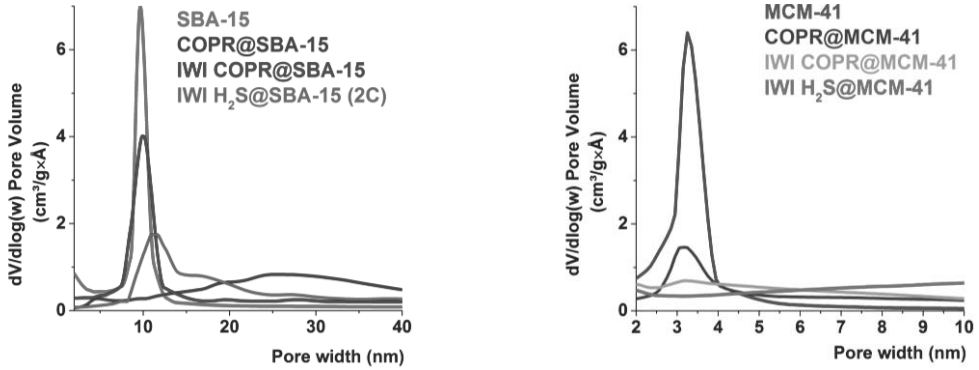

Figure 24: (left) Pore size distribution of ***SBA-15***, ***COPR@SBA-15***, ***IWI COPR@SBA-15***, ***IWI H_2S@SBA-15 after 2 cycles***, ***MCM-41***, ***COPR@MCM-41***, ***IWI COPR@MCM-41***, and ***IWI H_2S@MCM-41***. For nitrogen physisorption isotherms, see appendix C.2.

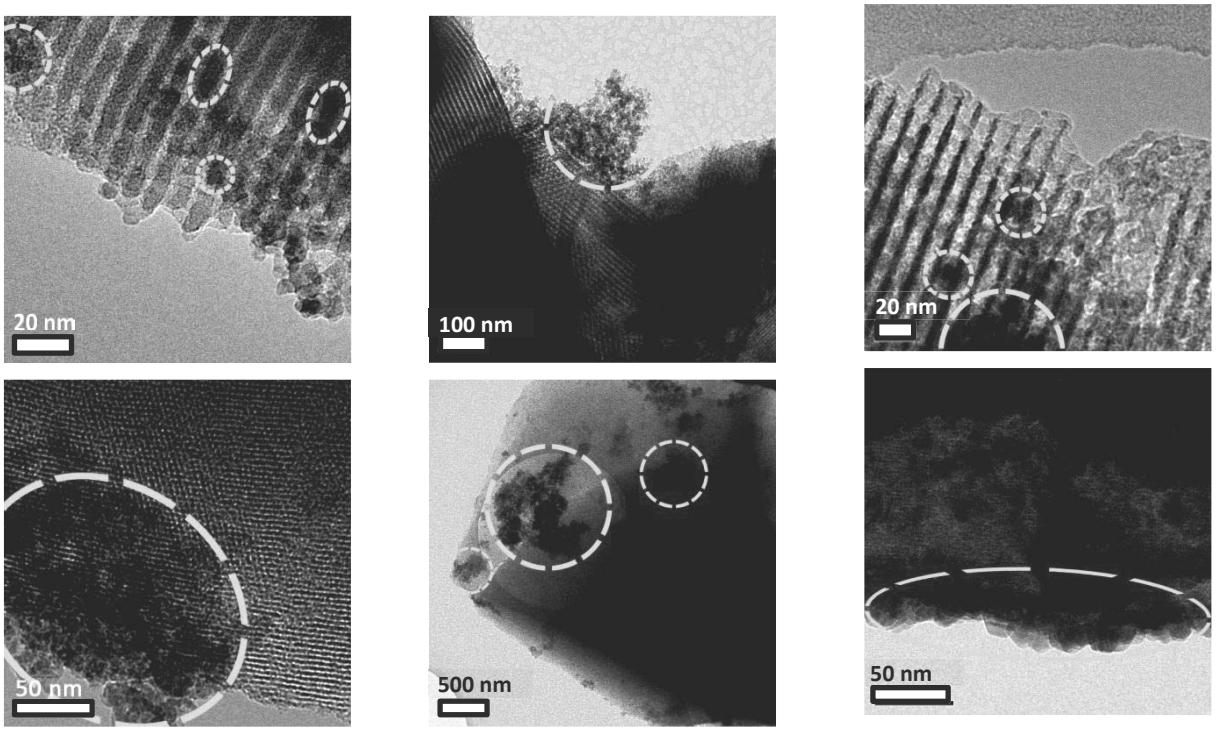

Figure 25: (left) TEM images from left to right: ***COPR@SBA-15***, ***IWI COPR@SBA-15***, and ***IWI H_2S@SBA-15 after 2 cycles*** (top row), ***COPR@MCM-41***, ***IWI COPR@MCM-41***, and ***IWI H_2S@MCM-41*** (bottom row).

The sulfide phases and their crystallinity were examined by wide angle XRD. The XRD reflections of the amorphous silica and sulfides can be distinguished for both supports loaded by co-precipitation, see Figure 23 right. In comparison to the two-step hydrothermal synthesis; the reflections were lower in intensity and much broader. This broadening can originate both from low crystallinity and small crystallites since the sulfide was deposited at room temperature without further thermal treatment or aging. The positions of the maxima of the reflections coincided well with those of $Cd_{0.5}Zn_{0.5}S$. This indicated the formation of a mixed metal sulfide without distinct phase separation. Both supports loaded by IWI co-precipitation formed some ill-defined sulfide, as broad peaks were present in the XRD pattern.

IWI H_2S yields, for both SBA-15 and MCM-41 (both after the first cycle), small sharp peaks positioned at a lower 2θ angle. This indicated the formation of a crystalline cadmium-rich phase while the zinc acetate precursor did not seem to be completely converted. Therefore, the IWI H_2S loaded SBA-15 was subjected to a second treatment which resulted in the formation of a crystalline zinc-rich phase, see Figure 23 right. It seemed that an additional H_2S treatment was needed to convert the zinc acetate precursor. This was contradicted by ICP measurements of the titania mesoporous beads loaded by the IWI H_2S method, see Table 5 (next chapter). The Cd/Zn ratio was found to be 1.01 for this sample, similar to the ratio found after a second H_2S treatment step. Thus based on XRD, ICP, and photocatalytic tests we can conclude that the entire metal precursor is converted in a single H_2S treatment step but highly active mixed metal sulfides could not be formed. Presumably the IWI H_2S route forms crystalline cadmium rich phase and a separate amorphous zinc rich phase. Therefore all IWI H_2S loaded supports were not subjected to additional treatment steps and this procedure was not developed further.

ICP measurements further confirmed that all loading procedures resulted in the deposition of the sulfide phase with a loading close to the nominal, see Table 3. Silica was not dissolved under the deposition conditions of the sulfide. Also the cadmium to zinc ratio was close to one for the measured samples, indicating that all metal precursors are effectively deposited.

			XPS				ICP	
Support	Loading	E_g	Cd%	Zn%	(Cd+Zn)/S	Cd/Zn	Wt% (nom.)	Wt% (exp.)
SBA-15	Copr.	2.70	44.3	55.7	1.73	1.01	50	51.8
	IWI Copr.	2.63	40.8	59.2	2.48	0.91	25	20.4
	IWI H_2S (2C)	2.43	31.5	68.5	1.64	0.98	25	21.5
	Hydrot. 100°C	2.47	29.6	70.4	1.59	N/A	50	N/A
MCM-41	Copr.	2.73	42.4	57.6	2.00	1.03	50	47.7
	IWI Copr.	2.53	57.4	42.6	1.79	N/A	25	N/A
	IWI H_2S	2.43	89.6	10.4	1.61	N/A	25	N/A
$Cd_{0.5}Zn_{0.5}S$ Copr. Ref.		2.58	43.9	56.1	1.67	N/A	/	N/A
$Cd_{0.5}Zn_{0.5}S$ Hydrot. 100 °C Ref.		2.41	12.6	87.4	1.61	N/A	/	N/A

Table 3: Summary of the data obtained by UV/VIS DRS, XPS, and ICP of the loaded SBA-15 and MCM-41 supports. The data for the unsupported sulfide prepared by co-precipitation and hydrothermal synthesis (100°C, 5 days) are also given.

From the nitrogen physisorption measurements we saw that SBA-15 loaded by co-precipitation lost its characteristic pore size distribution, however the channels were still visible in TEM, see Figure 25. The isotherm also resembled more a type II isotherm than type IV, typical for non-porous or macroporous materials with high adsorption energy (e.g. silica), see appendix C.2.[104] This could be an indication that the pores are (partially) filled or blocked by the sulfide. In SBA-15 loaded by IWI co-precipitation the pore size distribution was retained. For SBA-15 loaded by IWI H_2S the mean pore size was shifted to a larger value, in TEM images the pores were still visible and sulfide was found. The pore size distribution and the shape of the isotherm of MCM-41 loaded by co-precipitation were similar to ones of the bare support. In TEM images of this sample the channels were still visible but the sulfide seems to form aggregates on the outer surface, see Figure 25. The MCM-41 loaded by either IWI co-precipitation or IWI H_2S does not display the typical pore size distribution of bare

support, and neither the channels could be seen in TEM. This indicated that the mesostructure was lost, although this was contradicted with the small angle XRD in the case of IWI co-precipitation.

4.1.2.2 Loading of SBA-15 by hydrothermal synthesis at 100°C

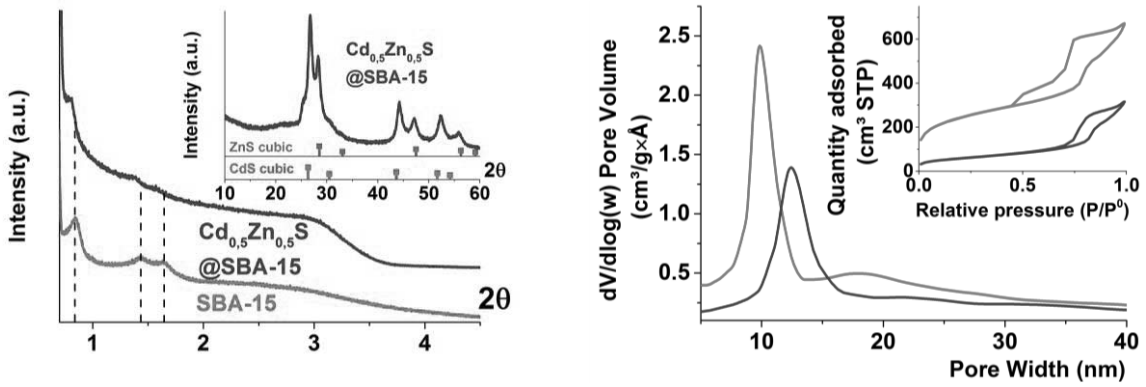

Figure 26: (left) Small and wide angle XRD patterns (right) pore size distribution and isotherms of ***SBA-15*** and ***$Cd_xZn_{1-x}S$@SBA-15*** by hydrothermal loading at 100°C. Red and green droplines represent reflection angles of cubic phase CdS (PDF 01-089-0440) and ZnS (PDF 00-005-0566) respectively.

The two-step hydrothermal loading of the sulfide on SBA-15 at 180°C (which is imperative to synthesize highly active sulfide photocatalysts) destroyed the mesostructure of the support. Therefore the two-step hydrothermal synthesis was adjusted. The first step which utilizes NaOH to precipitate the mixed hydroxide of cadmium and zinc was omitted. The dispersion of the support in the mixed solution of cadmium and zinc acetate was directly hydrothermally treated at 100°C in presence of thioacetamide as the sulfur source.

Small angle XRD indicated that the mesoporous structure of the support was retained as the first three reflections were preserved after the synthesis, see Figure 26 left. The positions of the reflections of the loaded sample were shifted towards lower angles; similarly to the SBA-15 loaded by the IWI H_2S method. Again the mean pore size of the loaded sample (12.7 nm) was larger than the lattice constant $a_{(100)}$ of the bare support (11.9 nm), see Figure 26 right. Thus the framework size must have increased during the sulfide deposition. Although the reason of this increase of the framework size is unclear. The isotherm of the SBA-15 loaded by hydrothermal synthesis retained its typical type IV shape, indicating that the pores were not blocked by deposited sulfide. TEM images however indicated that the photocatalyst was primarily formed on the outer surface or outside of the supports. Small amounts were found inside the pores, see appendix C.3.

The wide angle XRD pattern of the loaded support clearly showed phase separation of the sulfide. Lower angle reflections originated from the cadmium-rich phase while the set of peaks at the higher 2Θ values originated from the zinc-rich phase, as cadmium has a bigger ionic radius than zinc. The phase separation can originate from the difference of solubility product K_{sp} of CdS and ZnS: approx. 10^{-27} and 10^{-25} $\frac{mole^2}{l^2}$ respectively.[119] Cadmium sulfide precipitates first forming a cadmium-rich phase, when the cadmium source is depleted a zinc-rich phase can be formed.

4.1.3 Photocatalytic activity

All loaded samples were subjected to photocatalytic tests to determine their activity towards the hydrogen evolution reaction. Typically 20 or 40 mg of the composite, for

co-precipitation/hydrothermal loading and IWI co-precipitation/H_2S loading respectively, was dispersed in 50 ml of the sacrificial solution (0.25M Na_2S and 0.35M Na_2SO_3) under sonication. The dispersion was illuminated by a DC Hg(Xe) arc lamp (λ > 410 nm). The photogenerated H_2 was collected in a headspace and injected in a GC to determine the amount of the generated hydrogen and the evolution rate. All HER rates were normalized to the mass of active photocatalyst, based on the real loading determined by ICP (50 and 21 wt% for co-precipitation/hydrothermal and IWI co-precipitation/H_2S loading, respectively, see Table 3). The hydrogen evolution rates for silica supported samples are given in Figure 27.

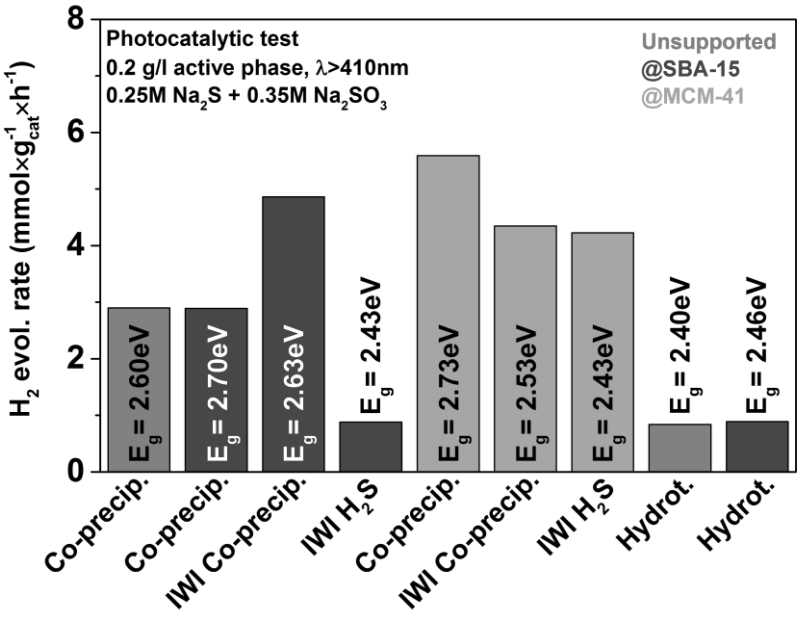

Figure 27: Hydrogen evolution rates ($mmol_{H2}×g_{cat}^{-1}×h^{-1}$) of unsupported $Cd_{0.5}Zn_{0.5}S$ and loaded on silica supports and their corresponding band gap.

The sulfide deposited on SBA-15 by hydrothermal synthesis, the reference unsupported sulfide by hydrothermal synthesis, and the sulfide deposited on SBA-15 by the IWI H_2S after two treatment steps displayed very low photocatalytic activities compared to the reference sulfide prepared by co-precipitation. This loss of activity can be explained by the phase separation evident from the XRD patterns, see Figure 23 right and Figure 26 left. As the cadmium-rich phase has low photocatalytic activity due to its conduction band being more positively positioned while the zinc-rich phase can only absorb UV light, which was removed by a longpass filter. This was in good agreement with the band gaps determined by UV/VIS DRS, all being about 2.4 eV, very close to the value reported for pure CdS. [44-46] Mind that the zinc rich phase is difficult to detect in the UV/VIS DRS spectrum, as CdS has the lowest band gap. Note that ICP indicated that all metal precursors are effectively precipitated by the excess of sulfur during the deposition, see Table 3. The cadmium to zinc ratio was close to 1 and the experimental loading was close to the nominal one. The surface composition determined with XPS gave a further insight in the composition of the sulfide phase, see Table 3. The percentage of zinc (in the mixture of Cd and Zn) on the surface of the sample was determined to be 68.5%, 70.4 % and 87.4% for the IWI H_2S (2C)@SBA-15, Hydrot@SBA-15 and hydrothermally synthesized unsupported sulfide respectively. Based on these results it could be hypothesized that a core-shell structure with cadmium rich phase in the core and zinc rich phase in the shell was formed. We assume that this originates from the difference in solubility product of CdS and ZnS: 10^{-27} and

10^{-25} $\frac{mole^2}{l^2}$ respectively.[119] The cadmium rich phase will precipitate first and form the core while the zinc rich phase if formed on top when the cadmium precursor is exhausted.

The SBA-15 loaded by IWI co-precipitation and all loaded MCM-41 composites showed an enhanced photocatalytic activity towards the HER in comparison to the unsupported sulfide prepared by co-precipitation, see Figure 27. For MCM-41 there seemed to be a correlation between the band gap and the activity. The hydrogen evolution rates dropped when the band gap was lowered for the MCM-41 support loaded by co-precipitation, IWI co-precipitation and IWI H_2S respectively. An additional series of MCM-41 loaded by the co-precipitation method was prepared but with different loadings of the sulfide photocatalyst, i.e. 40, 25, and 10 wt%. In this series a similar correlation was observed as the band gap and the activity towards the HER dropped from 2.54 eV and 3.55 $mmol_{H2}\times g_{cat}^{-1}\times h^{-1}$ for the 40 wt% loaded support to 2.48 eV and 2.27 $mmol_{H2}\times g_{cat}^{-1}\times h^{-1}$ for 10 wt% loading. The correlation between the HER rate and the band gap was in a good agreement with XRD as the loaded sulfides with larger band gaps displayed reflections at higher angles, indicating more zinc being incorporated in the solid solution. XPS results further confirmed that for all loaded MCM-41 composites the cadmium content was around 50%, in contrary to the inactive composites described above, see Table 3. The only exception was MCM-41 loaded by the IWI H_2S method. This sample had high cadmium content – 89.6% – which was in good agreement with the small band gap of 2.43 eV close to the value of pure CdS.[44-46] However ICP analysis of samples loaded by IWI H_2S – silica and titania – revealed that all metal precursor was converted in one treatment step, see Table 5 (next chapter) as the experimental loading was close to the nominal and the cadmium to zinc ratio was close to one. Thus the low surface content of zinc determined with XPS was not caused by the loss of the zinc precursor but rather a cadmium-rich core with zinc-rich shell was formed. Nevertheless it is clear that the difference in activity of the sulfides loaded on MCM-41 originated from the differences in the phase composition. Supporting of the sulfides on MCM-41 increased their activity almost by 93%, 58%, and 53% by co-precipitation, IWI co-precipitation and IWI H_2S respectively.

In contrast to the MCM-41-supported samples, the utilizations of SBA-15 improved the photocatalytic activity of the sulfide loaded with the IWI co-precipitation method only. We saw that this composite followed the trend of the loaded MCM-41 samples. Both the hydrogen evolution rate (4.86 $mmol_{H2}\times g_{cat}^{-1}\times h^{-1}$) and the band gap (2.63 eV) of the SBA-15 loaded by IWI co-precipitation fitted in between of those for MCM-41 loaded by co-precipitation and IWI co-precipitation, see Figure 27. Analogously the reflections of the sulfide in the XRD pattern were similar to those of the MCM-41 loaded by co-precipitation: broad and low in intensity peaks due to the low (25 wt%) loading, see Figure 23 right. XPS revealed that the cadmium content was 41%, matching the values found for the loaded MCM-41 samples. Thus similar photocatalytic activity of SBA-15 loaded by IWI co-precipitation and the series of loaded MCM-41 can be explained by similar phase composition and band gap. However the SBA-15 loaded by co-precipitation did not show enhanced HER rates in comparison to the co-precipitated reference sulfide, see Figure 27. It was not expected because a thorough characterization of this sample by XRD, XPS, ICP, and UV/VIS DRS indicated that a sulfide phase very similar to the more active samples was formed. Thus no evident reason of a detrimental effect on the HER rates could be found, like low band gap or phase separation. Therefore we can hypothesize that the sulfide was not deposited on the SBA-15 but rather two physically separate phases were formed, as the other silica supported sulfides all had enhanced HER rates.

Overall we can hypothesize that the increase of the activity of the sulfides deposited on both the SBA-15 and MCM-41 originated from the dispersion of the sulfide on the support and lower aggregation in comparison to its unsupported counterpart. This can maintain the accessibility of the solvent and incident photons to the photocatalyst and optimize the photocatalytic hydrogen production. The issue with the silica supports turned out to be their instability in the sacrificial solution. The high pH from the Na_2S (0.25M) corrupts the mesostructure, see appendix C.4. The use of an acidic sacrificial reactant, i.e. lactic acid, did not stop the deterioration of the structure and further lowered the activity. Important to note is that the activities were still low in comparison to the sulfides prepared by the two-step hydrothermal synthesis, used in the next chapter.

Chapter 5: $Cd_xZn_{1-x}S$ on titania supports

5.1 Results and discussion

5.1.1 Characterization of TiO_2 supports

A synergistic effect between titania and $Cd_xZn_{1-x}S$, which results in higher photocatalytic activity, is frequently reported in literature.[69, 89, 91, 92] It is hypothesized that this semiconductor forms a heterojunction with the sulfide. This electronic coupling can suppress the charge carrier recombination, resulting in a higher photocatalytic activity. Besides the introduction of a heterojunction by supporting the sulfides on titania, there is another advantage of this material. The silica supports were not compatible with the synthesis of the highly active sulfide photocatalyst while titania is very stable in a wide range of pH even under hydrothermal conditions.[4-6] This allowed us to use the two-step hydrothermal treatment that was developed for the synthesis of highly active unsupported sulfides.[55] In this work we used mesoporous titania beads as a support, this material was synthesized in accordance with the reported procedure.[93] This porous material was chosen due to its relatively high pore volume (0.3 cm^3/g) and high surface area (96 m^2/g) as a model semiconducting support comparable with the mesoporous silica counterparts. This support consists of porous spherical aggregates (about 0.7-1.0 µm in size) which are composed of anatase particles. As silica supports required milder synthetic conditions due to the stability issues, this complicated the direct comparison of the photocatalytic activities of the two sets of samples. At the later stage of the project a commercial white pigment – Degussa P25 – was used as a reference support for the comparison. This commercial material consists of individual titania crystallites (about 20 nm in size) or small aggregates which are composed of 80% anatase and 20% rutile.[120] In Table 4 the results of physisorption and UV-VIS diffuse reflectance analysis of these TiO_2 supports are summarized.

Support	Mean $Ø_{pore}$ (nm)	V_{BJH} (cm^3/g)	S_{BET} (m^2/g)	Eg (eV)
Mesoporous beads	20.8	0.31	91	3.49
	18.8	0.30	93	3.49
	24.2	0.36	104	3.57
Degussa P25	N/A	N/A	54	3.65

Table 4: Nitrogen physisorption data and band gap of mesoporous beads titania and Degussa P25 supports. Multiple rows indicate different batches of the support.

The synthesis of the mesoporous beads yielded samples with an average BET surface area of 96.0 m^2/g. The BJH pore volume was found to be 0.32 cm^3/g, about one third of the values found for the SBA-15 and MCM-41. A broad pore size distribution was observed with a maximum around 21 nm, see Figure 28 right. Spherical particles of about 0.7-1.0 µm in diameter were found by TEM, see Figure 29 middle. Based on the physisorption data Degussa P25 had negligible pore volume and a lower surface area of 54 m^2/g. Wide angle XRD revealed that the mesoporous beads were composed of anatase crystalline phase only, while Degussa P25 consists of 80 % anatase and 20% rutile phase, see Figure 28 left.[120] However the band gaps calculated from the UV/Vis diffuse reflectance spectroscopy did not coincide well with the values found in literature. For mesoporous beads, the band gap was found to be approx. 3.52 eV and for Degussa P25 − 3.65 eV. Anatase phase of TiO_2 is

reported to have a band gap of 3.2 eV, while the value for rutile should be of 3.0 eV.[16, 69, 92, 121, 122] The reason of this discrepancy is unclear and may stem from the accuracy of the instrument.

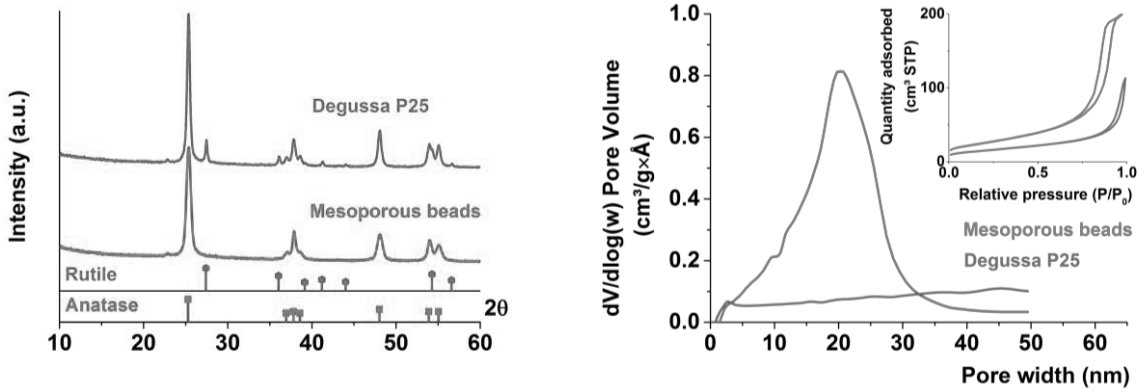

Figure 28: (left) Wide angle XRD of bare ***mesoporous beads*** and ***Degussa P25***. Ticks are reflection angles of rutile (PDF 00-021-1276) and anatase (PDF 00-021-1272) titania crystalline phase. The small peak around 2θ 22.8° in the XRD patterns corresponds to the copper K_β reflection of the (101) anatase plane. (right) Pore size distribution and nitrogen physisorption isotherms of bare titania supports.

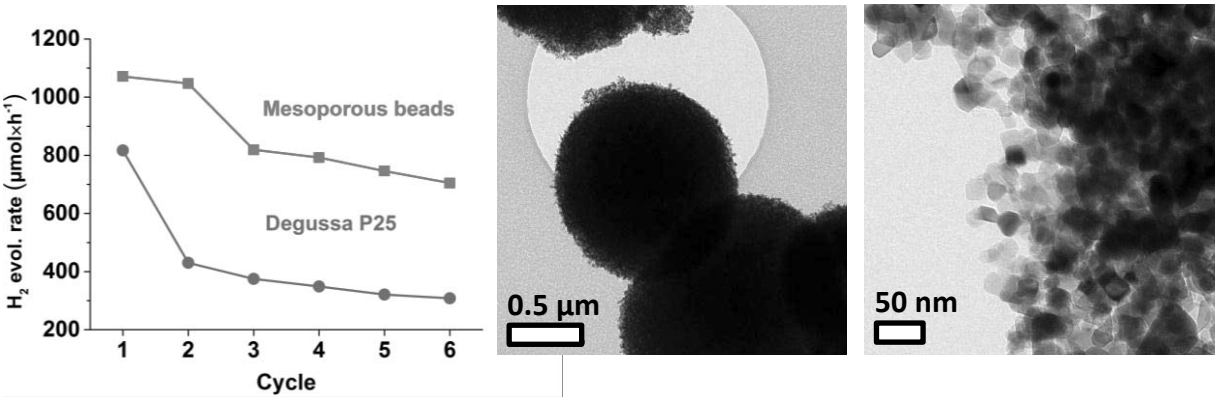

Figure 29: (left) Hydrogen evolution rates (in µmol×h^{-1}) of photoplatinized ***mesoporous beads*** and ***Degussa P25***. (middle) TEM image of spherical mesoporous beads particles of about 0.7-1 µm in size. (right) TEM image of Degussa P25 particles of about 10-20 nm in size.

Titania on itself can facilitate photocatalytic water splitting under UV irradiation.[123] However a co-catalyst is needed to reach high hydrogen evolution rates. Platinum is commonly used for this purpose and is deposited by *in-situ* photoplatinization, i.e. by reduction of $PtCl_6^{2-}$ to Pt^0 on a semiconductor surface under irradiation.[17] Prior to the loading of the sulfides we compared the photocatalytic activities of the bare platinized supports. The photocatalytic tests were carried out under irradiation of the full spectrum of the Hg(Xe) arc lamp in a 10 vol% methanol aqueous solution containing H_2PtCl_6 to achieve a 0.4 wt% loading. The hydrogen evolution rates are presented in Figure 29 left. The first cycle was run for 30 minutes while 15 minutes intervals were used for the rest. In between of the cycles the produced hydrogen was removed from the reactor. We observed that mesoporous beads were about 2-2.5 times more active than commercial Degussa P25. After several consequent runs the photocatalytic activity of both samples leveled off at around 700 and 300 $\mu mol_{H2} \times h^{-1}$ for the mesoporous beads and Degussa P25 respectively. This indicated that pure

anatase mesoporous beads were more active towards the HER than the commercial TiO_2 Degussa P25. Therefore the mesoporous beads were expected to be more active in the combination with the sulfide.

5.1.2 Loading of TiO_2 with $Cd_{0.5}Zn_{0.5}S$

Loading of both titania supports was carried out by the two-step hydrothermal synthesis of sulfides at 180°C described earlier in the silica support section, hereafter denoted as "hydrothermal loading". This synthesis yields the very active unsupported sulfide photocatalysts. In contrary to silica, titania is stable during both the deposition of $Cd(OH)_2$ and $Zn(OH)_2$ from the mixed solution with an alkali and the consequent hydrothermal conversion of the hydroxides into $Cd_xZn_{1-x}S$.[4-6] Besides this procedure two alternative loading routes were used as well. In these synthetic procedures the titania supports were first impregnated with the solutions of the metal acetates. Subsequently the metal precursor was sulfidized by hydrothermal conversion at 180°C with thioacetamide as the sulfur source or by the "H_2S" method (see chapter 4 for details). These procedures are further referred to as "IWI hydrothermal" and "IWI H_2S" respectively.

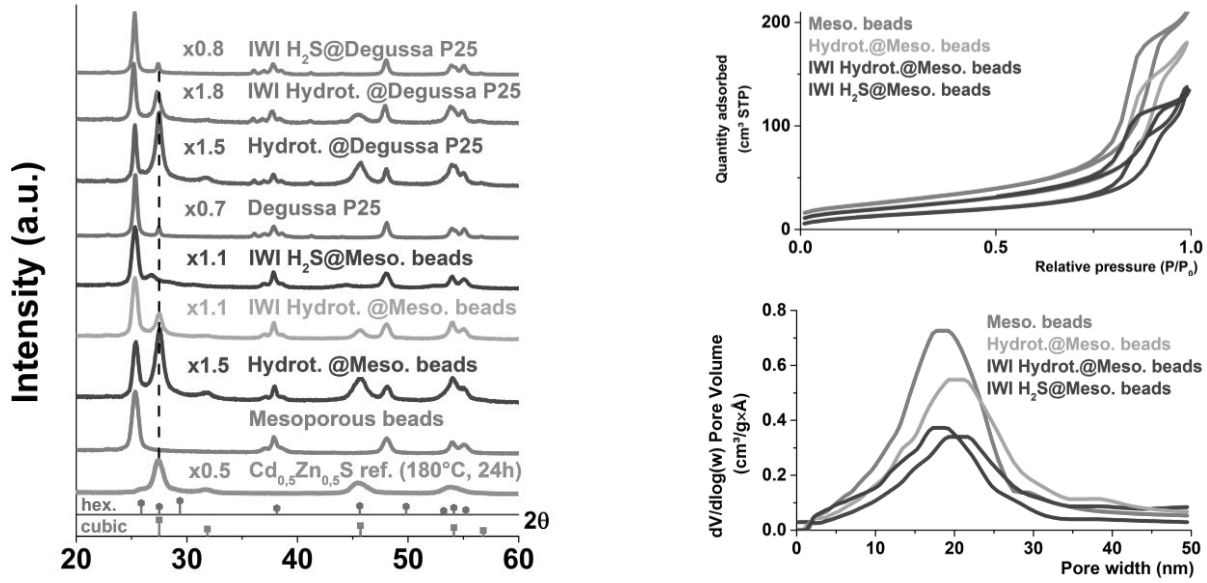

Figure 30: (left) Wide angle XRD and (right) pore size distribution and nitrogen adsorption/desorption isotherms of ***mesoporous beads***, ***Degussa P25***, ***Hydrot@meso. beads***, ***IWI Hydrot@meso. beads***, ***IWI H_2S@meso. beads***, ***Hydrot@Degussa P25***, ***IWI Hydrot@Degussa P25***, ***IWI H_2S@Degussa P25***, and unsupported ***$Cd_{0.5}Zn_{0.5}S$*** (hydrothermal 180°C, 24h). The Intensities of the XRD patterns were normalized to the first anatase (101) reflection of bare mesoporous titania**.** The small peak around 2θ 22.8° in the XRD patterns corresponds to the copper K_β reflection of the (101) anatase plane. The pore size distribution and nitrogen adsorption/desorption of Degussa P25 were left out as this support is not porous.

Wide angle XRD revealed sharp peaks of the anatase phase of TiO_2 and cubic $Cd_{0.5}Zn_{0.5}S$ phases for both (IWI) hydrothermally loaded mesoporous beads and Degussa P25, see Figure 30 left. It is evident that the sulfide is mainly present in the cubic crystal phase. The hexagonal phase cannot be unambiguously excluded as its main reflections overlap with the strong reflections of the cubic phase and the anatase/rutile phases of titania. For Degussa P25 the (110) reflection of rutile (2θ 27.5°)

cannot be distinguished as it overlaps with the much stronger (111) reflection of the cubic phase of the sulfide, but the higher reflections of rutile were present in the XRD pattern. The reflections of sulfide were consistently found at the same diffraction angles for both supports and coincide well with the angles predicted by Vegards law for a solid solution of $Cd_{0.5}Zn_{0.5}S$. The band gaps of the sulfide determined from the diffuse reflectance spectra were around 2.7-2.8 eV for this (IWI) hydrothermal loading. A similar value was found for unsupported sulfide. XPS analysis revealed that the ratio of the surface concentrations of the metals in the sulfide is typically 1, see Table 5. ICP further confirmed this value. Combining all the data obtained from UV-VIS DRS, XRD, ICP, and XPS allowed us to conclude that the (IWI) hydrothermal loading resulted in the formation of a mixed metal sulfide supported on titania. No evident degradation of the mesostructure of the loaded mesoporous beads was found based on the nitrogen physisorption. Both the pore size distribution and isotherms were similar, see Figure 30 right. The BET surface area, pore volume and mean pore size of all the loaded titania supports are given in appendix D.1. The pore size distributions and nitrogen adsorption-desorption isotherms of Degussa P25 were not given as this support is non-porous and no direct comparison can be made between the bare and loaded state. TEM analysis further confirms the formation of the intimate contact between the titania support and the sulfide particles, see Figure 31. The mesoporous beads and the Degussa P25 are composed of titania nanoparticles about 10-20 nm in size. The sulfide particles had more polyhedral shape resulting in triangular projections. The sizes of the sulfides particles were larger than their titania counterparts, in the range of 50-80 nm. For the mesoporous beads we saw the sulfides being deposited on the exterior of the spherical titania particles. Due to the thickness of the beads, it is difficult to determine their interior structure and composition. In the case of loaded Degussa P25 we saw, in contrary to loaded mesoporous beads, that the sulfide was surrounded by the titania particles, which should lead to a good physical and electronic contact between the two. An additional TEM image, in which two different phases (TiO_2 and $Cd_{0.5}Zn_{0.5}S$) can be identified based on the crystal lattice spacing, is given in appendix D.2.

			XPS				ICP	
Support	Loading	E_g(eV)	Cd%	Zn%	(Cd+Zn)/S	Cd/Zn	Wt% (nom.)	Wt% (exp.)
Meso. beads	Hydrot.	2.75	49.2	50.8	1.5	1.00	50	45.6
	IWI Hydrot.	2.69	52.2	47.8	1.3	1.00	25	20.0
	IWI H_2S	2.44	33.8	66.2	1.5	1.01	25	20.8
Degussa P25	Hydrot.	2.69	48.7	51.3	1.6	N/A	50	N/A
	IWI Hydrot.	2.68	46.6	53.4	1.3	N/A	25	N/A
	IWI H_2S	/	23.8	76.2	13.8	0.92	25	6.3
$Cd_{0.5}Zn_{0.5}S$ Hydrot. 180 °C Ref.		2.58	0.53	0.47	1.3	N/A	/	/

Table 5: Band gap of loaded titania supports, surface, and overall composition determined by XPS and ICP respectively.

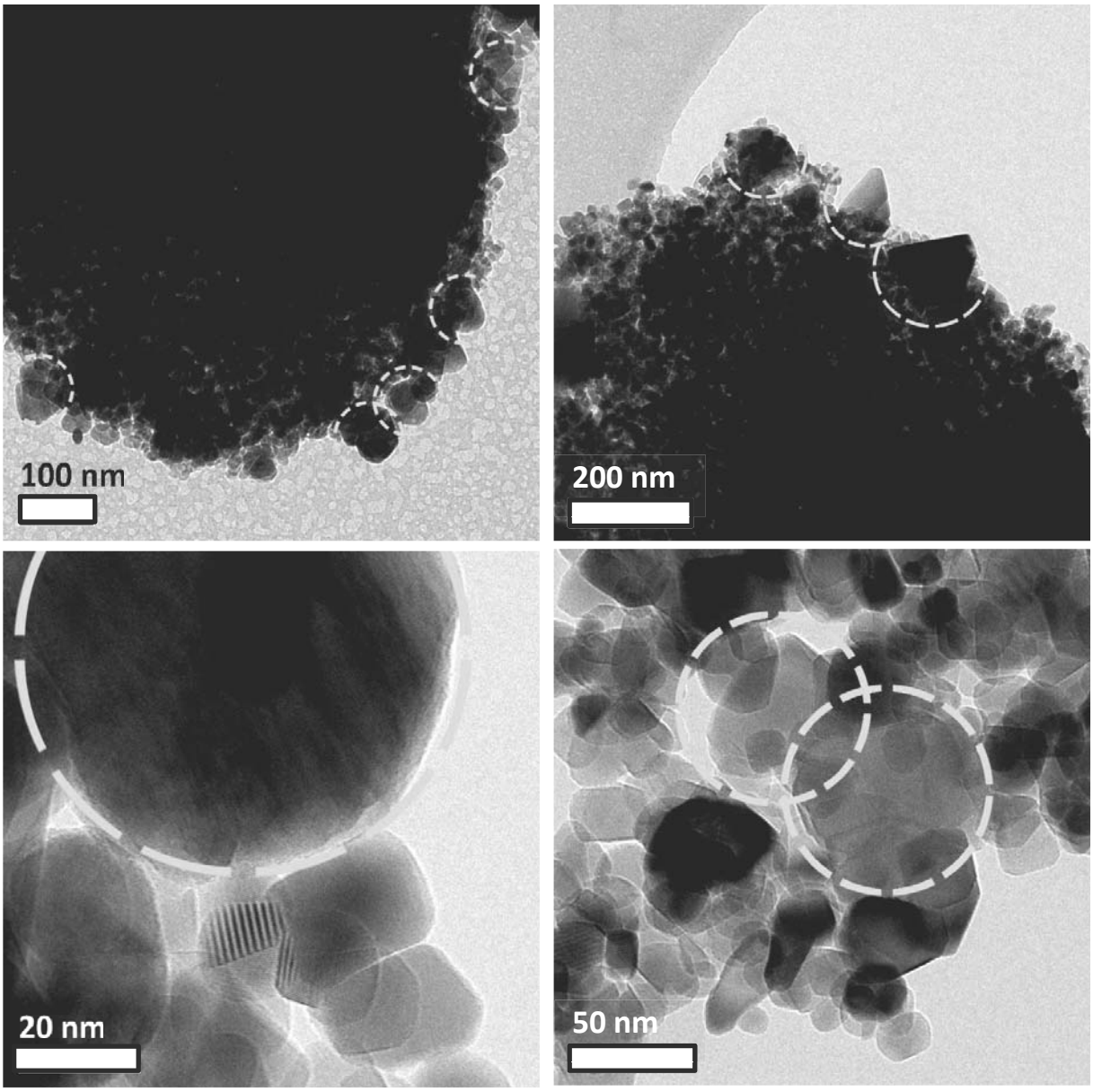

Figure 31: TEM images of loaded titania by: (left top) Hydrothermal @ mesoporous beads, (right top) IWI hydrothermal @ mesoporous beads, (left bottom) Hydrothermal @ Degussa P25, and (right bottom) IWI Hydrothermal @ Degussa P25.

In contrary to the (IWI) hydrothermal synthesis, the reflections of the sulfides made by means of the "IWI H_2S" procedure did not align well with the 2θ angles of $Cd_{0.5}Zn_{0.5}S$. For the sulfides loaded on the mesoporous beads we saw the shift of the reflection towards lower angles, which indicated the formation of a cadmium-rich phase. This was in a good agreement with the band gap values determined from the diffuse reflectance spectra. A band gap of 2.44 eV was found, close to the value of 2.4 eV reported for pure CdS.[44-46] The cadmium to zinc ratio of the sulfide was found to be 1 by mean of ICP. Comparison of this value with the data obtained from UV/VIS DRS and XRD indicated that a cadmium rich crystalline phase was formed together with amorphous zinc rich phase or crystalline zinc rich phase with very small crystallites. Loading of the sulfides on P25 impregnated with the metal salts via the H_2S route resulted in the sample which had no reflections that could be

ascribed to the Cd-Zn sulfide in the XRD pattern. The relative intensities of the first and second reflection – anatase (101) and rutile (110) – for both Degussa P25 and IWI H_2S@Degussa P25 are equal which means that the reflection at 2θ 27.5° did not originate from the sulfide phase but only from rutile present in P25 support. This was consistent with the diffuse reflectance spectroscopy data as no signal originating from a sulfide phase could be found. Determination of the sulfide loading on the Degussa P25 by ICP provided the reason for the absence of the reflections in XRD and the sulfide band gap. As only 6.3 wt% (on the basis of sulfide) was deposited on the titania, which could be not enough for the detection of the sulfide phase by XRD and UV/VIS DRS. A very strong signal of sulfur in higher oxidation state (+4 or +6) was also observed in the XPS spectrum of this sample.

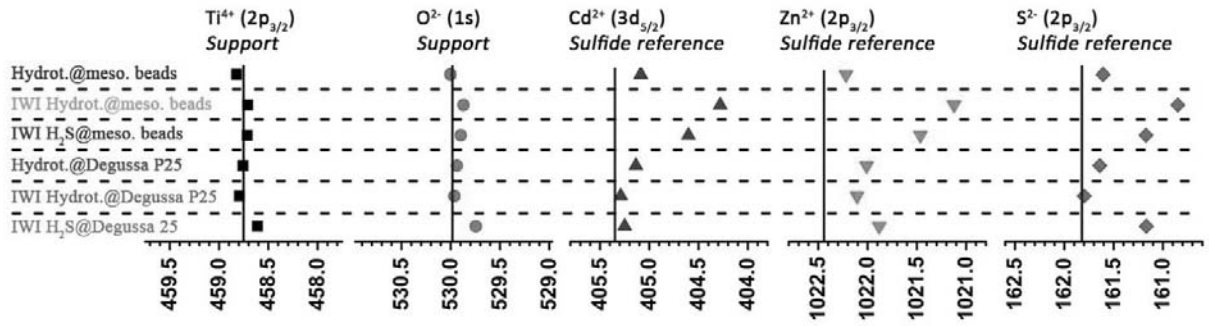

Figure 32: XPS binding energy positions of elements in the loaded titania supports. Vertical lines represent the binding energy of the elements found in either the bare support (Ti and O) of the unsupported mixed Cd-Zn solid solution (Cd, Zn, and S)

The XPS results, initially used to determine the surface composition, revealed that the binding energies of the Cd, Zn, and S peaks did not match those found for the unsupported sulfide, see Figure 32. We determined the binding energies of Ti and O in the bare titania support and ones of the Cd, Zn, and S in the unsupported sulfide these values are represented by the vertical lines. These values were compared with the values obtained for the loaded titania support, which are shown by the solid symbols. We found that the binding energies of Ti and O remained close to those of the bare supports but the Cd, Zn, and S were substantially lower in comparison to the values found for the unsupported sulfide. The lowering of the binding energy could not be unambiguously ascribed to a possible particle size effect. Mahamuni and co-workers studied ZnS quantum dots and found that the particle size had no effect on the binding energies of the Zn and S.[124] Similarly, the results obtained by Bowen Katari and co-workers also did not show any correlation between the binding energies of Cd and the size of CdSe quantum dots.[125] An explanation of the negative shift was suggested by Li and co-workers.[126] They loaded CdS quantum dots on titania nanotubes and observed a decrease in the Cd binding energy in comparison to the unsupported CdS quantum dots. This effect was explained by the formation of an electronic contact between the CdS and TiO_2, i.e. the heterojunction. Similarly, hybrid systems of CdS and PdS, and $Cd_{0.5}Zn_{0.5}S$ and titania nanotubes also displayed the decrease of the Cd binding energy.[68, 83] Therefore we can assume, based on the XPS results, that we have not only deposited the sulfide phase on the titania support but also formed an electronic junction between the two. This heterojunction could facilitate the charge carrier separation.

5.1.3 Photocatalytic activity

The photocatalytic activity towards the HER of the titania supports loaded with Cd-Zn sulfides was tested. In the tests the composite was dispersed in 50 ml of a 0.25M Na_2S, 0.35M Na_2SO_3 sacrificial solution to achieve the loading of 0.2 g/l of $Cd_{0.5}Zn_{0.5}S$ based on the nominal loading. The dispersion was illuminated with a Hg(Xe) DC arc lamp with the UV component being removed by a longpass filter to test the activity under visible light only. The initial hydrogen production rates are shown in Figure 33.

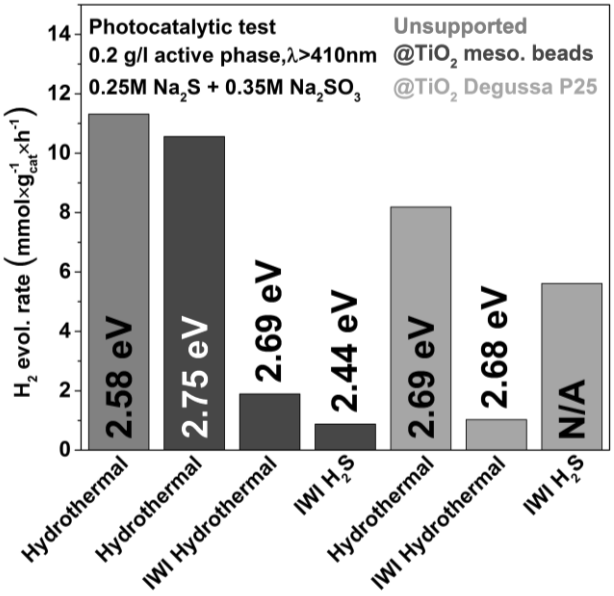

Figure 33: Photocatalytic activity of unsupported sulfide (hydrothermal, 180°C, 24h), loaded mesoporous beads, and loaded Degussa P25 titania. The hydrogen evolution rates are normalized to the mass of the sulfide based on the loading determined by ICP (50wt% for (IWI) hydrothermal, 21wt% for IWI hydrothermal and mesoporous beads loaded by IWI H_2S, and 6.3% for Degussa P25 loaded by IWI H_2S).

We observed a reduced photocatalytic activity compared to the unsupported photocatalyst, see Figure 33. The sulfide loaded on the mesoporous beads or Degussa P25 by the hydrothermal treatment was about 7% and 28% less active than the unsupported one. This finding was in contrast to our expectations because in literature the synergetic effect of the combination of TiO_2 and $Cd_xZn_{1-x}S$ has been reported.[69, 89, 91, 92] Characterization of the hydrothermally deposited sulfide with ICP and XPS confirmed that all the metal precursor was converted into the sulfide as the cadmium to zinc ratio was close to 1 and the experimental loading was close to the nominal 50 wt%, see Table 5. The XRD pattern and UV/VIS DRS further confirmed that a mixed Cd-Zn sulfide was formed as the reflections of the sulfide and the band gap match well with the values found for the unsupported $Cd_{0.5}Zn_{0.5}S$, see Figure 30 and Table 5. Deposition of the sulfide on the support by the IWI hydrothermal method resulted in even lower photocatalytic activities towards the HER, the values are 1.1 and 1.9 $mmol_{H2}\times g_{cat}^{-1}\times h^{-1}$ for loaded Degussa P25 and mesoporous beads respectively. This was unexpected as the band gaps, XRD patterns, ICP, and XPS data match very well with the hydrothermally loaded supports. The very low activity of the mesoporous beads loaded by the IWI H_2S method – 0.9 $mmol_{H2}\times g_{cat}^{-1}\times h^{-1}$ – can be explained similarly to the SBA-15 loaded with the IWI H_2S method described in the previous chapter. ICP indicated that all metal precursors were deposited as the ratio of cadmium to zinc was close to 1 and the experimental loading close to the

nominal one, see Table 5. The XRD pattern indicated that only cadmium-rich phase was formed as the reflection were shifted towards lower 2θ values, in good agreement with the band gap of 2.44 eV found determined from the UV/VIS DRS, see Figure 30 and Table 5. The surface was found to be zinc-enriched based on XPS. Thus we can assume that a crystalline cadmium rich core is formed and an amorphous zinc rich phase was deposited around it. Possibly the zinc rich phase was crystalline but composed of small crystallites, not visible in XRD. Nonetheless this phase separation resulted in a lower photocatalytic activity as the cadmium-rich phase is not very active towards the HER as its conduction band is placed too positively. The zinc rich phase on its turn is also not active as its band gap lies in the UV region, which is removed by a longpass filter. The origin of the higher activity – 5.6 $mmol_{H2} \times g_{cat}^{-1} \times h^{-1}$ – of the Degussa P25 loaded by the IWI H_2S can also be found in the ICP results, see Table 5. The H_2 evolution rates are given after normalization to the mass of the sulfide photocatalyst. The loading determined by ICP indicated that only 6.3 wt% was deposited, thus normalization yields a large value compared to the other.

The lower photocatalytic activities of the sulfides loaded on the titania support was unexpected because loading of both supports via these methods – except the H_2S method – resulted in the formation of the sulfide phases very similar to the more active unsupported sample. The wide angle XRD patterns, band gap and surface composition determined by XPS of the sulfide on the supports coincide well with the data obtained for the unsupported sulfide. Therefore this loss in activity must originate from the introduction of the titania.

Titania has a high refractive index – 2.4 to 2.9 depending on wavelength and crystalline phase – resulting in strong scattering of the incident light.[127] We can assume that this light shedding lowered the activity as part of the incident photons got reflected back from the test cell decreasing the light utilization efficiency. This hypothesis agrees well with the lower activity of the loaded titania supports by the IWI hydrothermal loading procedures as these samples contained only 25 wt% of sulfide in comparison to 50 wt% for normal hydrothermal loading. The lower loading results in a larger amount of titania being present in the system, as the total amount of sulfide was kept constant. These phenomena can also explain the lower activity of the Degussa-P25-supported sulfides, with the exception of the "IWI H_2S" route. The Degussa P25 is composed of individual nanoparticles (~20 nm in size) while the mesoporous beads consist of larger aggregates (0.7-1 μm in size). The dispersions of the Degussa P25 are optically much denser compared to their mesoporous beads counterpart. Therefore the Degussa P25 dispersion can scatter light more effectively and thereby lower the activity.

Another possible explanation of the detrimental effect of the combination of Cd-Zn sulfide and TiO_2 is based on the electronic interaction between the titania support and sulfide. The photogenerated electrons could either be effectively injected into the titania conduction band but cannot reduce water to hydrogen. Two hypotheses are therefore established. The first one, hereafter referred to as hypothesis 1, can be formulated as follows: "The titania support scatters the incident light so efficiently that photons are reflected before they can be absorbed, thereby lowering the efficiency of the overall process". The second, hereafter referred to as hypothesis 2, can be formulated as follows: "Electrons generated on the sulfide are effectively injected into the titania conduction band but cannot be used to reduce water to hydrogen, thereby lowering the efficiency of the overall process." We have to note that neither of the two assumptions excludes the other. Both hypotheses are artistically represented in the form of cartoons in Figure 34.

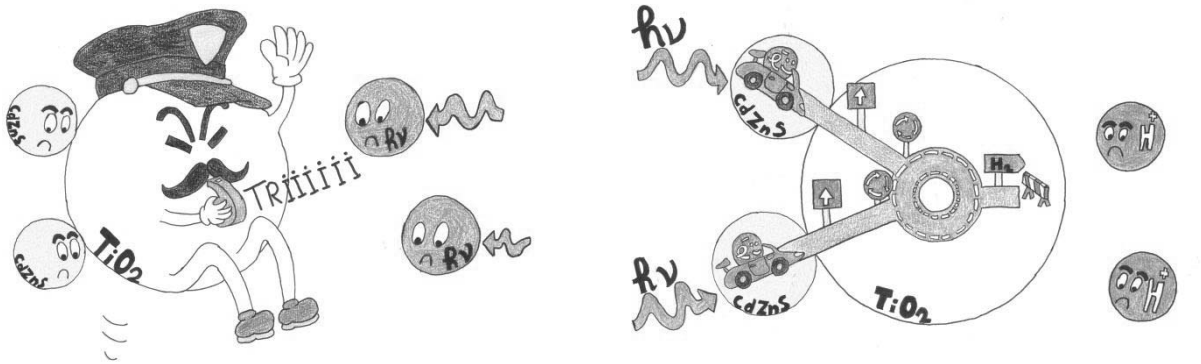

Figure 34: (left) Cartoon representation of hypothesis 1. Incident photons are effectively scattered by the titania, thereby lowering their absorption by the sulfide and the photocatalytic activity. (right) Cartoon representation of hypothesis 2. Electrons are injected into the conduction band of titania but cannot reach the solid/liquid interface. The electrons will recombine before they can be used, which lowers the efficiency of the process and thereby the photocatalytic activity.

To improve the photocatalytic activity of the supported sulfides, it is desirable to elucidate which phenomenon is at play and thus which hypothesis is true. Accurate measurement of the amount of reflected light is difficult due to the lack of the suitable equipment; therefore we first focused on the hypothesis 2. We used photoplatinization of the titania supports (0.4 wt% loading) to create active sites for the hydrogen evolution on the surface of the titania particles. These active sites should provide the injected electrons with an efficient pathway for water reduction and raise the photocatalytic activity of the composite.

We found that platinization of titania prior to the deposition of the sulfide by hydrothermal treatment substantially lowers the photocatalytic activity, see Figure 35 left. We suspected that poisoning of the platinum by the sulfur during the deposition of the sulfide was the reason for this loss in activity. Therefore determining the oxidation state of the platinum by means of XPS was desirable. The loading of the platinum was only 0.4 wt% and cannot be measured by means of XPS. Therefore photoplatinization was repeated with 4 wt% platinum loading. After deposition of sulfide on the platinized titania support (4 wt% Pt), XPS analysis was carried out to determine the chemical state of the platinum. The XPS signal was weak even for this sample but several components could be clearly distinguished, see Figure 35 right. We found that the ratio of areas of the two peaks which can be ascribed to the $4f_{5/2}$ to $4f_{7/2}$ lines of Pt^0 was about 1.2 (1598/1364) while the value of 0.75 is expected from the multiplicity of these states. This means that the peak positioned at the higher binding energy was an overlap of the two components: $4f_{5/2}$ of Pt^0 and $4f_{7/2}$ of Pt^{n+}. This indicated the oxidation (likely sulfidation) of platinum during the loading onto the support. Due to the weak signal it is difficult to say whether platinum was sulfidized by the excess of H_2S (i.e. PtS and/or PtS_2), or forms oxygenated species (PtO, PtO_2, and/or $Pt(OH)_2$). We found that the ratio of the amount of oxidized platinum species Pt^{n+} to the metallic platinum Pt^0 was 0.42. Therefore the lowered activity of the sulfide deposited on the platinized supports most likely originated from the poisoning of the hydrogen evolution sites on titania. Another reason of this loss of the photocatalytic activity could be light absorption by the support because after platinization the appearance of the titania support changed from white into brownish.

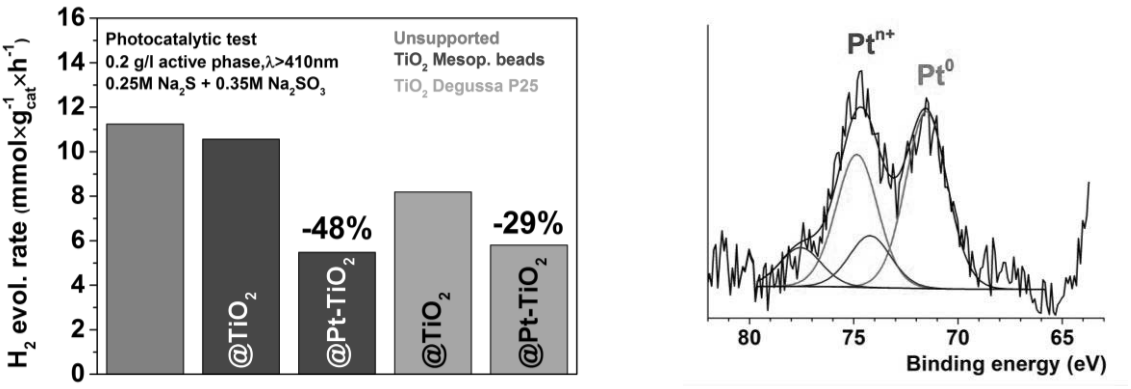

Figure 35: (left) Photocatalytic activity of sulfides loaded on (un)platinized titania supports by hydrothermal synthesis. (right) Pt 4f XPS region of Pt(4 wt%)-TiO_2 mesoporous beads hydrothermally loaded with $Cd_{0.5}Zn_{0.5}S$.

The deposition of platinum on the support prior to the sulfide loading lowered the activity of the composites, see Figure 35 left. Therefore we carried out the photoplatinization of the samples after the deposition of the sulfide on titania. The loading of the Pt was normalized to the active phase (sulfide) and was kept at 0.8 wt%. The photodeposition of Pt was carried out for 2 hours. Then the HER rate was measured in cycles of 30 minutes and between cycles the evolved hydrogen was removed from the system. The results are shown in Figure 36 left.

We expected that platinization of the composites would result in more active photocatalysts than the unsupported samples. However we found that the platinized unsupported sulfide still had the highest activity towards the HER. Interestingly, the platinized mesoporous beads composite was found to be less active in comparison with the loaded Degussa P25, see Figure 36 left. We found the mesoporous beads to be a more active photocatalyst on itself than Degussa P25, see Figure 29 left. This disproves out hypothesis 2 which states that electrons injected in the CB of titania could not be used to reduce water, thus titania acted as an electron sink/trap. If it was true, one could expect the platinized composite with the mesoporous beads to be more active than Degussa P25 which disagrees with our observations. We think that electrons were not transferred from the sulfide to the CB of titania. Probably, these phases do not exchange charge carriers, which could be caused by a mismatch of the conduction band potentials of the semiconductors: at pH 7 -0.7 V for TiO_2 (anatase) and -1.4 V for $Cd_{0.5}Zn_{0.5}S$.[61] In this case $PtCl_6^{2-}$ species could be reduced only on the HER sites of the sulfide under visible light. To confirm the lack of the electron transfer between sulfide and oxide phases we carried out the photodeposition of Pt on the Degussa P25 composite under UV illumination and tested its activity under visible light illumination. Under these experimental conditions platinum should have been reduced primarily on titania. The photocatalytic activity of this sample was found to be equal to the activity of the unplatinized composite. This finding let us conclude that hypothesis 2 was incorrect and that there was no vectorial transport of the electrons in the composite ($CB_{Cd0.5Zn0.5S} \rightarrow CB_{TiO2} \rightarrow Pt$) despite the electronic interaction evident from the XPS spectra. We suppose that this originated from a mismatch of the energy levels of the CBs, which is about 0.7 V.[61]

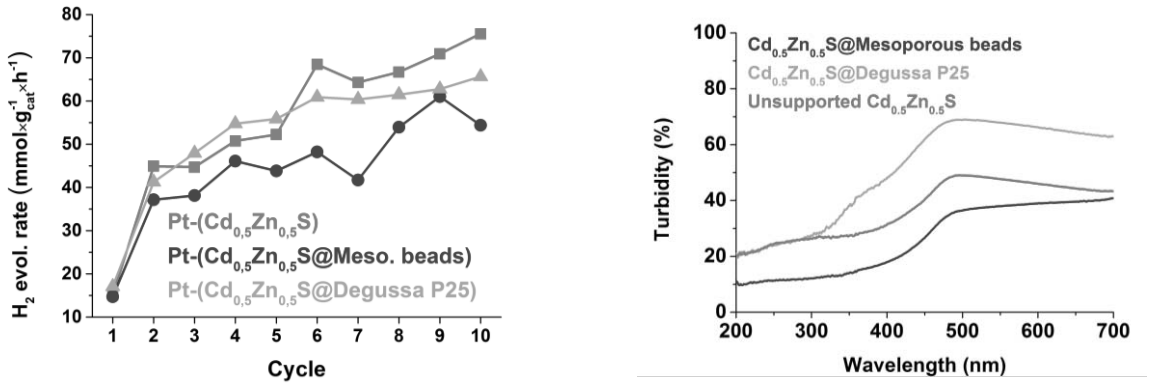

Figure 36: (left) Photocatalytic activity of platinized (un)supported sulfides. The produced hydrogen was removed between cycles. (right) Turbidity of dispersions of the (un)supported sulfides. The concentrations of the suspensions were equal to those used in the photocatalytic test.

Based on the results described above we arrived to a conclusion that the light scattering by TiO_2, formulated in hypothesis 1, is the origin of the lower photocatalytic activity or the mixed sulfide loaded on TiO_2 supports. To check this assumption we measured and compared turbidity of the dispersions of (un)supported sulfides of the same concentration which was used for the photocatalytic tests, see Figure 36 right. The turbidity value here is the ratio (T_d/T_t) of the diffuse transmitted light (T_d) to the overall transmittance (T_t) and can be used as a measure of the scattering properties of dispersions. For the comparison of the turbidity of the dispersions we used the spectral region λ>520nm because the active phase ($Cd_{0.5}Zn_{0.5}S$) does not absorb at these wavelengths. One can see that the dispersion of the Degussa P25 composite had the highest turbidity, which explained why this sample had the lowest photocatalytic activity without the co-catalyst. The lower turbidity of the loaded mesoporous beads in comparison with the unsupported and loaded Degussa P25 samples can originate from the difference in sizes of the particles. In the case of the loaded mesoporous beads the system is composed of the large spherical particles with metal sulfide being anchored on them (beads of the size 0.7-1.0 µm), while the unsupported and Degussa-P25-supported sulfides consist of individual crystallites (20-100nm) or small aggregates (100-300 nm). In this work we normalized loading of the samples on the amount of the active phase which required 10 mg of unsupported sulfide or 20 mg of a composite in 50 ml. In this case the number of individual particles of the mesoporous beads composite in the suspension is substantially lower than in the case of unsupported sulfides or composited with P25. This results in the least dense suspension for the mesoporous beads. For the unplatinized samples the photocatalytic activity of the sulfide deposited on the mesoporous beads was higher than the activity of the loaded Degussa P25 but lower than one of the unsupported sulfide. The unsupported sulfide was the most active one even though its turbidity was relatively high. This is likely due to the fact that light scattering properties of bare sulfide are different from those of the composites with TiO_2 due to the difference in the refraction coefficients of these materials and strong optical absorption of Cd-Zn sulfide in the visible spectrum.

The reason why among the platinized samples the composite with Degussa P25 was more active than the loaded mesoporous beads is unclear. If we assume that the light scattering is the main factor lowering the photocatalytic activity, one would expect the platinized mesoporous beads composite to be the most active sample in contrast to the experimental results. A possible explanation of this phenomenon could be that part of the sulfide particles was incorporated in the mesostructure of the beads, which lowers the area of the sulfide exposed to the electrolyte.

Strong light scattering can explain the lower photocatalytic activity of the samples prepared with the IWI methods and sulfides deposited on platinized titania as well, see Figure 33 and Figure 35 left. The samples prepared by the IWI methods contained a higher amount of titania (75 wt%) and more turbid dispersions were used for the photocatalytic tests as the sulfide concentration was kept constant (0.2 g/l). Light absorption by the platinized titania could be the reason why the sulfides deposited on platinized support were less active than ones deposited on bare titania, as the appearance of the support changed from white to brownish upon photodeposition of Pt.

We observed that the hydrogen evolution rate increased after each cycle for all the samples, see Figure 36. Many authors reported in literature that the photoplatinization of CdS, ZnS, or $Cd_xZn_{1-x}S$ was carried out within one hour.[53, 75, 90, 128] However we found that the platinization of the (un)supported sulfides was not completed within the initial two hours. ICP results indicated that even after 6.5 hours of the photocatalytic test only 0.1 wt% Pt out of 0.8 wt% of the precursor was deposited.

In summary, we conclude that the decrease of the photocatalytic activity of the sulfides loaded on titania originated mainly from the high refraction index of the supports which results in strong light scattering lowering the amount of the incident photons absorbed by the photocatalyst. In the present work we did not find solid evidences of the injection of the photogenerated electrons from the sulfide into the CB of titania despite the fact that based on XPS analysis binding energies of the sulfide shifted towards lower values upon loading on TiO_2 which indicates electronic interaction with the support. The absence of the charge carrier transfer from the sulfide to the titania phase may originate from the mismatch of the energy levels of the CBs. The platinization of the (un)supported sulfides resulted in a substantial increase of the HER rate.

Chapter 6: Conclusions and future prospects

In the present work we studied $Cd_{0.5}Zn_{0.5}S$ nanoparticles supported on silica-based and titania-based materials, to address the issue of the aggregation of the unsupported photocatalysts, which lowers their activity.

Model materials (i.e. SBA-15 and MCM-41) were chosen for the silica-based supports because of their well-defined mesostructure and high surface area. The best improvement of the photocatalytic activity, by 93% in comparison with the unsupported samples, was achieved by co-precipitation of the sulfides on the MCM-41 support. The SBA-15 and MCM-41 act as a mere physical support because no charge carrier transfer between the photocatalyst and the dielectric support can occur. This meant that the increased photocatalytic activity of the silica-supported $Cd_{0.5}Zn_{0.5}S$ must originate from physical immobilization and spatial separation of the photocatalyst phase on SiO_2. Unfortunately the chosen silica-based supports were incompatible with the harsh hydrothermal conditions required for the synthesis of highly active sulfides. The loading at room temperature retained the mesostructure of the supports but resulted in the formation of the sulfide phases with varying crystallinity, band gap and photocatalytic activity. In contrary to the findings of Macías-Sánchez and co-workers,[64] our results indicated that the silica-based supports were unstable in the sacrificial solution (0.25M Na_2S, 0.35M Na_2SO_3) and the support's mesostructure was deteriorated during the photocatalytic test.

Mesoporous beads and Degussa P25 were chosen as the titania-based supports. The choice of titania was determined by its high chemical stability making it compatible with the harsh synthetic conditions. This material is reported in literature to enhance the activity of the $Cd_xZn_{1-x}S$ photocatalysts forming with it a heterojunction, which improves the charge carrier separation. [69, 89, 91, 92] This was in contrast with our results as all titania supported sulfides had lower photocatalytic activity than the unsupported samples. In principle a positive effect of the physical anchoring on the support, also seen in the case of the silica-supported sulfides, could be expected if an electronic interaction between both phases did not improve the photocatalytic activity. However we found that the high refractive index of the titania resulted in a strong scattering of the incident light therefore lowering the photocatalytic activity of the titania-supported sulfides. An electronic interaction between the sulfide and titania phases was found by XPS analysis but it seemed that no electrons generated on the sulfide were injected into the CB of titania. This could be caused by a mismatch of the energy levels of the conduction bands of the sulfide and titania phases. Platinization of the (un)supported sulfides was found to increase their photocatalytic activity up to 5.2-8 times (depending on the samples), but the deposition of Pt was not complete even after 6.5 hours.

The development of a viable (supported) $Cd_xZn_{1-x}S$ photocatalyst for the reduction of water still requires a large research effort. In this thesis we have shown that addressing the aggregation of the $Cd_xZn_{1-x}S$ photocatalyst particles can increase the photocatalytic activity of the sulfides and that the properties of the support play an important role. For instance, silica-based supports are instable at high pH and under hydrothermal conditions. For the future work with silica-based supports we suggest to replace the model mesoporous materials like SBA-15 and MCM-41 by non-structured silica. The majority of the sulfide is deposited on the exterior and not inside the pores and the mesostructure is corrupted during photocatalytic tests. The synthesis of SBA-15 or MCM-41 requires substantial time but their mesoporous properties seem not to play an important role in the

photocatalytic activity of the supported sulfides. The composites of the titania-based support and sulfide require further research of their electronic interaction. We speculate that the difference of the electric potentials between the conduction bands of titania and the sulfide phases might be too large – 0.7V for $Cd_{0.5}Zn_{0.5}S$ and TiO2 (anatase) at pH 7 – for the efficient charge transfer.[61] Thus lowering the zinc content in the sulfide phase could overcome this problem and improve the activity as for the composites of CdS and TiO_2 the difference between both conduction band edges is only 0.2 V and this system has been frequently reported in literature to be more active than unsupported CdS.[61, 68, 69, 89] Another route could be a use of a thin film of titania decorated with the sulfide. In this geometry, the incident light passes the sulfide phase first before being scattered by the titania phase.

References

1. T. Hirai, H. Okubo and I. Komasawa, *Journal of Colloid and Interface Science*, 2001, 235, 358-364.
2. T. Hirai, M. Nanba and I. Komasawa, *Journal of colloid and interface science*, 2003, 268, 394-399.
3. S. Macias-Sanchez, R. Nava, V. Hernandez-Morales, Y. Acosta-Silva, L. Gomez-Herrera, B. Pawelec, S. Al-Zahrani, R. Navarro and J. Fierro, *International Journal of Hydrogen Energy*, 2012, 37, 9948-9958.
4. M. Skocaj, M. Filipic, J. Petkovic and S. Novak, *Radiology and Oncology*, 2011, 45, 227-247.
5. C. Minero, F. Catozzo and E. Pelizzetti, *Langmuir*, 1992, 8, 481-486.
6. S. Wendt, P. T. Sprunger, E. Lira, G. K. Madsen, Z. Li, J. Ø. Hansen, J. Matthiesen, A. Blekinge-Rasmussen, E. Lægsgaard and B. Hammer, *Science*, 2008, 320, 1755-1759.
7. A. Sieminski, *International energy outlook 2013*, 2013.
8. N. S. Lewis and D. G. Nocera, *Proceedings of the National Academy of Sciences*, 2006, 103, 15729-15735.
9. BP, *British Petroleum Statistical Review of World Energy June 2013*, 2013.
10. BP, *British Petroleum Energy Outlook 2035*, 2014.
11. N. S. Lewis and G. Crabtree, *Sciences Workshop on Solar Energy Utilization, April 18-21*, 2005.
12. R. van de Krol and M. Grätzel, *Photoelectrochemical hydrogen production*, Springer, 2011.
13. G. Kopp and J. L. Lean, *Geophysical Research Letters*, 2011, 38.
14. X. Zong, G. Wu, H. Yan, G. Ma, J. Shi, F. Wen, L. Wang and C. Li, *The Journal of Physical Chemistry C*, 2010, 114, 1963-1968.
15. G. Liu, L. Zhao, L. Ma and L. Guo, *Catalysis Communications*, 2008, 9, 126-130.
16. G.-S. Li, D.-Q. Zhang and J. C. Yu, *Environmental science & technology*, 2009, 43, 7079-7085.
17. J. M. Herrmann, J. Disdier and P. Pichat, in *Studies in Surface Science and Catalysis*, ed. C. N. B. Imelik, G. Coudurier, H. Praliaud, P. Meriaudeau, P. Gallezot, G. A. Martin, J. C. Vedrine, Elsevier, 1982, vol. 11, pp. 27-35.
18. G. A. Olah, *Angewandte Chemie International Edition*, 2005, 44, 2636-2639.
19. F. Joó, *ChemSusChem*, 2008, 1, 805-808.
20. I. Chorkendorff and J. W. Niemantsverdriet, *Concepts of modern catalysis and kinetics*, John Wiley & Sons, 2006.
21. J. M. Ogden, *Annual Review of Energy and the Environment*, 1999, 24, 227-279.
22. EPA, *Technical support document for hydrogen production: proposed rule for mandatory reporting of greenhouse gases*, 2008, 1-25.
23. J. B. S. Haldane, *Daedalus or Science and the Future*, EP Dutton, 1924.
24. G. Centi and S. Perathoner, *Greenhouse Gases: Science and Technology*, 2011, 1, 21-35.
25. W. Leitner, *Angewandte Chemie International Edition in English*, 1995, 34, 2207-2221.
26. T. Brunner, *BMW Clean EnergyFuel Systems*, 2006.
27. R. P. O'Hayre, S.-W. Cha, W. Colella and F. B. Prinz, 2006.
28. S. Enthaler, *ChemSusChem*, 2008, 1, 801-804.
29. J. J. Romm, *Issues in science and technology*, 2004, 74-81.
30. C. S. Enache, *Characterization of Thin Film Photoanodes for Solar Water Splitting*, 2012.
31. Chemical Composition of Natural Gas, https://www.uniongas.com/about-us/about-natural-gas/chemical-composition-of-natural-gas, Accessed 22th of December, 2014.
32. J. Rostrup-Nielsen, in *Catalysis*, eds. J. Anderson and M. Boudart, Springer Berlin Heidelberg, 1984, vol. 5, ch. 1, pp. 1-117.
33. Natural Gas Reforming, http://energy.gov/eere/fuelcells/natural-gas-reforming, Accessed 22nd of December, 2014.
34. I. Dybkjær, *Int. J. Hydrocarb. Eng.* , 1997/98, 3, 56.
35. J. D. Holladay, J. Hu, D. L. King and Y. Wang, *Catalysis Today*, 2009, 139, 244-260.

36. A. Rodrigues, J. C. Amphlett, R. F. Mann, B. A. Peppley and P. R. Roberge, *Energy Conversion Engineering Conference, 1997. IECEC-97., Proceedings of the 32nd Intersociety*, 1997, DOI: 10.1109/IECEC.1997.660236, 768-773 vol.762.
37. B. Sørensen, *Hydrogen and fuel cells: emerging technologies and applications*, Academic Press, 2012.
38. S. Dunn, *International Journal of Hydrogen Energy*, 2002, 27, 235-264.
39. A. B. Murphy, P. R. F. Barnes, L. K. Randeniya, I. C. Plumb, I. E. Grey, M. D. Horne and J. A. Glasscock, *International Journal of Hydrogen Energy*, 2006, 31, 1999-2017.
40. Y. Zhang, Doctoral Thesis, Technische Universiteit Eindhoven, 2014.
41. R. Krishnan, in *Encyclopedia of Electrochemistry*, Wiley-VCH Verlag GmbH & Co. KGaA, 2007, DOI: 10.1002/9783527610426.bard060001.
42. C. A. Grimes, O. K. Varghese and S. Ranjan, *Light, water, hydrogen: the solar generation of hydrogen by water photoelectrolysis*, Springer, 2007.
43. A. Kitai, *Principles of solar cells, LEDs and diodes: the role of the PN junction*, John Wiley & Sons, 2011.
44. D. Lincot and G. Hodes, *The Electrochemical Society*, 2006.
45. O. Zelaya-Angel, J. J. Alvarado-Gil, R. Lozada-Morales, H. Vargas and A. Ferreira da Silva, *Applied Physics Letters*, 1994, 64, 291-293.
46. T. L. Chu, S. S. Chu, J. Britt, C. Ferekides and C. Q. Wu, *Journal of Applied Physics*, 1991, 70, 2688-2693.
47. G. Conibeer, M. Green, E.-C. Cho, D. König, Y.-H. Cho, T. Fangsuwannarak, G. Scardera, E. Pink, Y. Huang, T. Puzzer, S. Huang, D. Song, C. Flynn, S. Park, X. Hao and D. Mansfield, *Thin Solid Films*, 2008, 516, 6748-6756.
48. A. L. Linsebigler, G. Lu and J. T. Yates, *Chemical Reviews*, 1995, 95, 735-758.
49. J. T. Yates, *Surface Science*, 2009, 603, 1605-1612.
50. K. Kalyanasundaram, E. Borgarello, D. Duonghong and M. Grätzel, *Angewandte Chemie International Edition in English*, 1981, 20, 987-988.
51. E. Borgarello, K. Kalyanasundaram, M. Grätzel and E. Pelizzetti, *Helvetica Chimica Acta*, 1982, 65, 243-248.
52. I. B. Rufus, V. Ramakrishnan, B. Viswanathan and J. C. Kuriacose, *Langmuir*, 1990, 6, 565-567.
53. J. F. Reber and K. Meier, *The Journal of Physical Chemistry*, 1984, 88, 5903-5913.
54. S. Sain, S. Patra and S. Pradhan, *Journal of Physics D: Applied Physics*, 2011, 44, 075101.
55. M. Liu, L. Wang, G. M. Lu, X. Yao and L. Guo, *Energy & Environmental Science*, 2011, 4, 1372-1378.
56. R. Traill and R. Boyle, *American Mineralogist*, 1955, 40, 555-559.
57. M. Liu, D. Jing, Z. Zhou and L. Guo, *Nat Commun*, 2013, 4.
58. A. Breithaupt, *Annalen der Physik*, 1840, 127, 507-510.
59. B. Gilbert, B. Frazer, H. Zhang, F. Huang, J. Banfield, D. Haskel, J. Lang, G. Srajer and G. De Stasio, *Physical Review B*, 2002, 66, 245205.
60. G. Nabiyouni, R. Sahraei, M. Toghiany, M. M. Ara and K. Hedayati, *Rev. Adv. Mater. Sci*, 2011, 27, 52-57.
61. S. Kohtani, E. Yoshioka and H. Miyabe, *Intech*, 2012.
62. P. Cherin, E. L. Lind and E. A. Davis, *Journal of The Electrochemical Society*, 1970, 117, 233-236.
63. Y. Wang, J. Wu, J. Zheng, R. Jiang and R. Xu, *Catalysis Science & Technology*, 2012, 2, 581-588.
64. S. Macías-Sánchez, R. Nava, V. Hernandez-Morales, Y. Acosta-Silva, B. Pawelec, S. Al-Zahrani, R. Navarro and J. Fierro, *International Journal of Hydrogen Energy*, 2013, 38, 11799-11810.
65. A. Litke, J.P. Hofmann and E. J. M. Hensen, Paper in work.
66. X. Zong, J. Han, G. Ma, H. Yan, G. Wu and C. Li, *The Journal of Physical Chemistry C*, 2011, 115, 12202-12208.

67. M. Nguyen, P. D. Tran, S. S. Pramana, R. L. Lee, S. K. Batabyal, N. Mathews, L. H. Wong and M. Graetzel, *Nanoscale*, 2013, 5, 1479-1482.
68. Y. Chen and L. Guo, *Journal of Materials Chemistry*, 2012, 22, 7507-7514.
69. J. ChuláKim, Y. BokáLee, J. HoonáHong, J. InáLee, J. WookáYang, W. InáLee and N. HwiáHur, *Chemical communications*, 2006, 5024-5026.
70. W. Zhang, Z. Zhong, Y. Wang and R. Xu, *The Journal of Physical Chemistry C*, 2008, 112, 17635-17642.
71. L. Yuliati, M. Kimi and M. Shamsuddin, *Beilstein Journal of Nanotechnology*, 2014, 5, 587-595.
72. L. Liao and C. W. Ingram, *Applied Catalysis A: General*, 2012, 433–434, 18-25.
73. Y. Li, M. Ma, W. Chen, L. Li and M. Zen, *Materials Chemistry and Physics*, 2011, 129, 501-505.
74. K. Zhang, D. Jing, Q. Chen and L. Guo, *International Journal of Hydrogen Energy*, 2010, 35, 2048-2057.
75. Y. Wang, Y. Wang and R. Xu, *The Journal of Physical Chemistry C*, 2012, 117, 783-790.
76. J. Zhensheng, L. Qinglin, F. Liangbo, C. Zhengshi, Z. Xinhua and X. Chanjuan, *Journal of Molecular Catalysis*, 1989, 50, 315-332.
77. S. Trasatti, *Journal of Electroanalytical Chemistry and Interfacial Electrochemistry*, 1972, 39, 163-184.
78. B. E. Conway and B. V. Tilak, *Electrochimica Acta*, 2002, 47, 3571-3594.
79. B. E. Conway, H. Angerstein-Kozlowska and F. C. Ho, *Journal of Vacuum Science & Technology*, 1977, 14, 351-364.
80. J. Tafel, *Z. phys. Chem*, 1905, 50, 641.
81. Volmer M. and Erdey-Gru T., *Z. Physik. Chem.*, 1930 150, 203-213.
82. X. Zong, H. Yan, G. Wu, G. Ma, F. Wen, L. Wang and C. Li, *Journal of the American Chemical Society*, 2008, 130, 7176-7177.
83. J. Meng, Z. Yu, Y. Li and Y. Li, *Catalysis Today*, 2014, 225, 136-141.
84. H. Liu, K. Zhang, D. Jing, G. Liu and L. Guo, *International Journal of Hydrogen Energy*, 2010, 35, 7080-7086.
85. W. Zhang and R. Xu, *International Journal of Hydrogen Energy*, 2009, 34, 8495-8503.
86. W. Zhang, Y. Wang, Z. Wang, Z. Zhong and R. Xu, *Chem. Commun.*, 2010, 46, 7631-7633.
87. H. Weiß, A. Fernandez and H. Kisch, *Angewandte Chemie International Edition*, 2001, 40, 3825-3827.
88. Y. J. Zhang and L. Zhang, *J. Inorg. Mater.*, 2008, 23, 66-70.
89. J. Li, L. Wu, L. Long, M. Xi and X. Li, *Applied Surface Science*, 2014, 322, 265-271.
90. H. Park, W. Choi and M. R. Hoffmann, *Journal of Materials Chemistry*, 2008, 18, 2379-2385.
91. S. Qian, C. Wang, W. Liu, Y. Zhu, W. Yao and X. Lu, *Journal of Materials Chemistry*, 2011, 21, 4945-4952.
92. N. Serpone, P. Maruthamuthu, P. Pichat, E. Pelizzetti and H. Hidaka, *Journal of Photochemistry and Photobiology A: Chemistry*, 1995, 85, 247-255.
93. D. Chen, L. Cao, F. Huang, P. Imperia, Y.-B. Cheng and R. A. Caruso, *Journal of the American Chemical Society*, 2010, 132, 4438-4444.
94. D. Zhao, J. Feng, Q. Huo, N. Melosh, G. H. Fredrickson, B. F. Chmelka and G. D. Stucky, *science*, 1998, 279, 548-552.
95. D. Zhao, Q. Huo, J. Feng, B. F. Chmelka and G. D. Stucky, *Journal of the American Chemical Society*, 1998, 120, 6024-6036.
96. Y. Guan and E. J. M. Hensen, *Applied Catalysis A: General*, 2009, 361, 49-56.
97. E. B. Celer and M. Jaroniec, *Journal of the American Chemical Society*, 2006, 128, 14408-14414.
98. A. Benhamou, M. Baudu, Z. Derriche and J. P. Basly, *Journal of Hazardous Materials*, 2009, 171, 1001-1008.
99. A. Sayari and Y. Yang, *The Journal of Physical Chemistry B*, 2000, 104, 4835-4839.

100. H. Meléndez-Ortiz, L. García-Cerda, Y. Olivares-Maldonado, G. Castruita, J. Mercado-Silva and Y. Perera-Mercado, *Ceramics International*, 2012, 38, 6353-6358.
101. R. F. Egerton, *Physical principles of electron microscopy*, Springer, 2005.
102. W. H. Bragg and W. L. Bragg, *Proc. R. Soc. Lond. A*, 1913, 88, 428-438.
103. Shimadzu, *XRD-6000*, 2014.
104. J. B. Condon, *Surface area and porosity determinations by physisorption: measurements and theory*, Elsevier, 2006.
105. S. Brunauer, P. H. Emmett and E. Teller, *Journal of the American Chemical Society*, 1938, 60, 309-319.
106. E. P. Barrett, L. G. Joyner and P. P. Halenda, *Journal of the American Chemical Society*, 1951, 73, 373-380.
107. S. Kelly, D. Hesterberg and B. Ravel, *Soil Science Society of America: Madison, WI*, 2008, 444.
108. Shimadzu, *Measurements of Band Gap in Compound Semiconductors - Band Gap Determination frm Diffuse Reflectance Spectra-*, 2014.
109. J. Tauc, R. Grigorovici and A. Vancu, *physica status solidi (b)*, 1966, 15, 627-637.
110. C. D. Wagner, L. E. Davis, M. V. Zeller, J. A. Taylor, R. H. Raymond and L. H. Gale, *Surface and Interface Analysis*, 1981, 3, 211-225.
111. C. B. Boss and K. J. Fredeen, *Concepts, instrumentation and techniques in inductively coupled plasma optical emission spectrometry*, Perkin Elmer Norwalk, 1999.
112. W. Sangchoom and R. Mokaya, *Journal of Materials Chemistry*, 2012, 22, 18872-18878.
113. C.-Y. Chen, H.-X. Li and M. E. Davis, *Microporous Materials*, 1993, 2, 17-26.
114. A. Katiyar, S. Yadav, P. G. Smirniotis and N. G. Pinto, *Journal of Chromatography A*, 2006, 1122, 13-20.
115. D. Zhao, J. Sun, Q. Li and G. D. Stucky, *Chemistry of Materials*, 2000, 12, 275-279.
116. F. Hoffmann, M. Cornelius, J. Morell and M. Fröba, *Angewandte Chemie International Edition*, 2006, 45, 3216-3251.
117. M. Birkholz, *Thin film analysis by X-ray scattering*, John Wiley & Sons, 2006.
118. D. Zhao, Y. Wan and W. Zhou, *Ordered mesoporous materials*, John Wiley & Sons, 2012.
119. Solubility product constants, http://www4.ncsu.edu/~franzen/public_html/CH201/data/Solubility_Product_Constants.pdf , Accessed 19 november, 2014.
120. J. M. Macak, M. Zlamal, J. Krysa and P. Schmuki, *Small*, 2007, 3, 300-304.
121. S. Chen, M. Paulose, C. Ruan, G. K. Mor, O. K. Varghese, D. Kouzoudis and C. A. Grimes, *Journal of Photochemistry and Photobiology A: Chemistry*, 2006, 177, 177-184.
122. X. Wang, J. C. Yu, C. Ho, Y. Hou and X. Fu, *Langmuir*, 2005, 21, 2552-2559.
123. A. Fujishima and K. Honda, *Nature*, 1972, 238, 37-38.
124. S. Mahamuni, A. A. Khosravi, M. Kundu, A. Kshirsagar, A. Bedekar, D. Avasare, P. Singh and S. Kulkarni, *Journal of applied physics*, 1993, 73, 5237-5240.
125. J. B. Katari, V. L. Colvin and A. P. Alivisatos, *The Journal of Physical Chemistry*, 1994, 98, 4109-4117.
126. G. Li, L. Wu, F. Li, P. Xu, D. Zhang and H. Li, *Nanoscale*, 2013, 5, 2118-2125.
127. C. R. Tubío, F. Guitián, J. R. Salgueiro and A. Gil, *Materials Letters*, 2015, 141, 203-206.
128. L. Ge, F. Zuo, J. Liu, Q. Ma, C. Wang, D. Sun, L. Bartels and P. Feng, *The Journal of Physical Chemistry C*, 2012, 116, 13708-13714.
129. P. Babelon, A. S. Dequiedt, H. Mostéfa-Sba, S. Bourgeois, P. Sibillot and M. Sacilotti, *Thin Solid Films*, 1998, 322, 63-67.
130. A. M. Nymark, Master Thesis Master Thesis, Norwegian University of Science and Technology, 2012.
131. L. Li, J. Ding and J. Xue, *Chemistry of Materials*, 2009, 21, 3629-3637.

Appendix A: Additional details on the synthesis and characterization

A.1 Loading by IWI H_2S

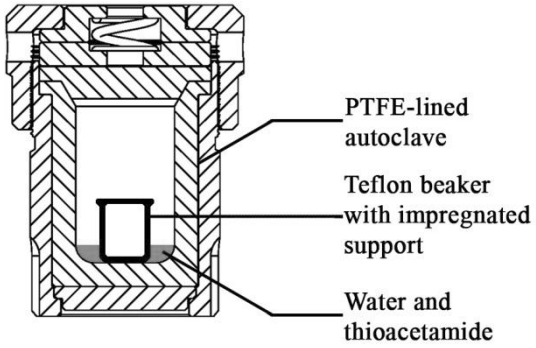

Figure 37: Schematic of sulfidation of the impregnated support by the IWI H_2S procedure. H_2S is generated *in situ* by hydrolysis of the thioacetamide and heating to 100°C. The Cd^{2+} and Zn^{2+} precursor is converted into the sulfide by ion exchange with the H_2S.

A.2 XPS binding model of elements

The binding model of each element was constrained according to the following parameters: the area of the lower multiplicity state was constrained to the product of the area of the higher multiplicity state and 0.5 (p state), 0.666 (d state), or 0.75 (f state). [20] The Si 2p envelope was fitted using one component as the splitting constant is very small. The Ti 2p envelope was fitted by 4 components, Ti^{4+} $2p_{3/2}$, Ti^{4+} $2p_{1/2}$ (+5.72 eV), Ti^{3+} $2p_{3/2}$ (-1.4 eV), and Ti^{3+} $2p_{1/2}$ (+4.32 eV). The FWHM of the Ti^{3+} $2p_{3/2}$ and Ti^{3+} $2p_{1/2}$ peaks were constrained to the value of Ti^{4+} $2p_{3/2}$ and Ti^{4+} $2p_{1/2}$ respectively. The O 1s envelope was fitted by two components O^{2-} $1s_{fram}$ (four-coordinated oxygen in the framework) and O^{2-} $1s_{hydroxyl}$ (hydroxyl groups at the surface; +1.7 eV).[129, 130] The Cd 3d envelope was fitted with 2 components Cd^{2+} $3d_{5/2}$ and Cd^{2+} $3d_{3/2}$ (+5.4 eV), and FWHM of Cd^{2+} $3d_{3/2}$ constrained to the value of Cd^{2+} $3d_{5/2}$. The Zn 2p envelope was fitted with 2 peaks Zn^{2+} $2p_{3/2}$ and Zn^{2+} $2p_{1/2}$ (+22.97 eV), and FWHM of Zn^{2+} $2p_{1/2}$ constrained to the value of Zn^{2+} $2p_{3/2}$. Sulfur 2p was fitted with 2 components S^{2-} $2p_{3/2}$ and S^{2-} $2p_{1/2}$ (+1.18 eV), and FWHM of S^{2-} $2p_{1/2}$ constrained to the value of S^{2-} $2p_{3/2}$. The Pt 4f envelope was fitted with 3 components, Pt^0 $4f_{7/2}$, and Pt^0 $4f_{5/2}$ (+3.33 eV), and Pt^{n+} $4f_{7/2}$ (+3.33eV) and the FWHM of all components were constrained to the value of the Pt^0 $4f_{7/2}$ component.

Appendix B: Schematic of the photocatalytic setup

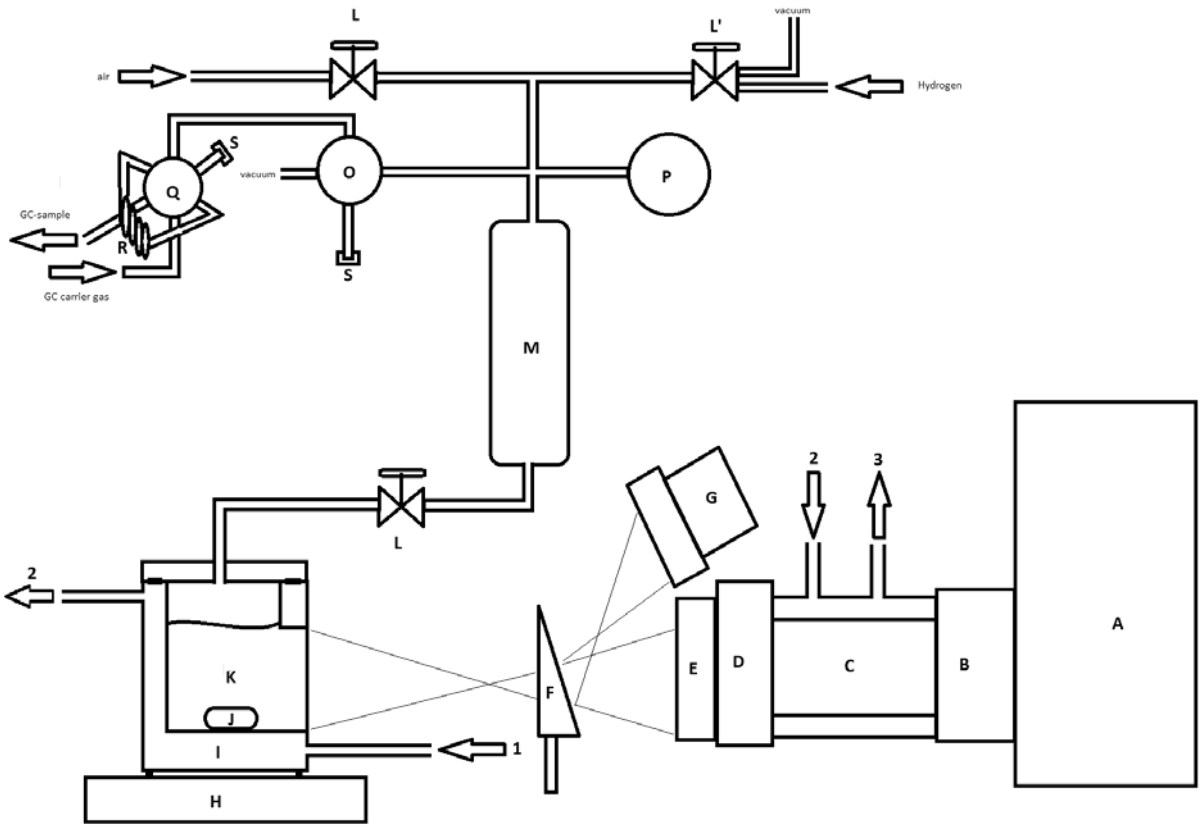

Figure 38: Schematical representation of the setup for testing the photocatalytic activity. The letters represent: (A) Light source(Xe/Hg lamp), (B) Collimated condenser, (C) IR-filter (water), (D) 420 nm high-pass filter, (E) convex lens (f=5cm), (F) Beam splitter, (G) Photo-sensor, (H) Stirring plate, (I) Reactor with cooling mantel, (J) Stirring magnet, (K) Liquid with sacrificial reagent and dispersed photocatalyst, (L)&(L') manual 2- and 3-way valves resp., (M) Headspace, (O) motorized 4-way valve, (P) Pressure gauge, (Q) motorized 6-way valve, (R) 1 mL loop of tubing and (S) end caps. The numbers represent cooling water: (1) from cooler/pump, (2) from reactor to IR-filter and (3) back to cooler/pump.

Appendix C: Additional data on $Cd_xZn_{1-x}S$ on silica supports

C.1 Hydrothermal stability test of SBA-15

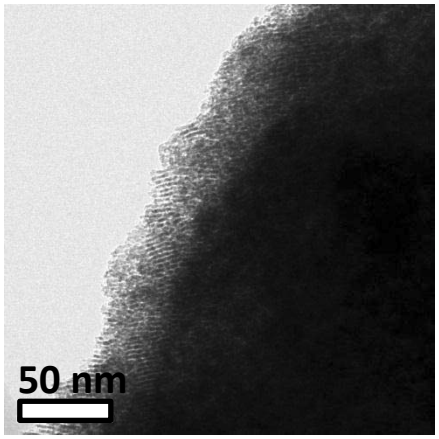

Figure 39: TEM image of hydrothermally treated SBA-15 (180°C, 1 day).

Treatment	Mean $Ø_{pore}$ (nm)	V_{BJH} (cm^3/g)	S_{BET} (m^2/g)
H_2O	30.5	0.73	208
H_2O + thioacetamide	N/A	0.18	63
1.0M NaAc	N/A	0.26	99
1.0M NaAc + thioacetamide	N/A	0.07	44

Table 6: Summary of nitrogen physisorption results of hydrothermally treated SBA-15. Mean pore diameters are determined from pore size distribution, pore volume by the Barret-Joyner-Halenda (BJH) method and surface areas by the Brunauer-Emmet-Teller (BET) method. The adsorption branch was used for all values.

C.2 Nitrogen adsorption-desorption isotherms of loaded SBA-15 and MCM-41

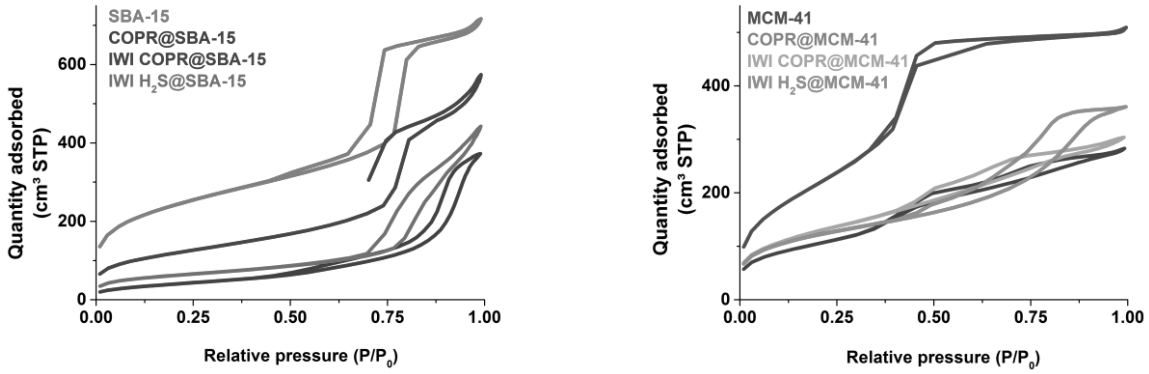

Figure 40: Nitrogen adsorption-desorption isotherms of (left) ***SBA-15***, ***COPR@SBA-15***, ***IWI COPR@SBA-15***, ***IWI H_2S@SBA-15 after 2 cycles*** and (right) ***MCM-41***, ***COPR@MCM-41***, ***IWI COPR@MCM-41***, and ***IWI H_2S@MCM-41***.

C.3 TEM images of SBA-15 loaded by hydrothermal synthesis of the sulfide

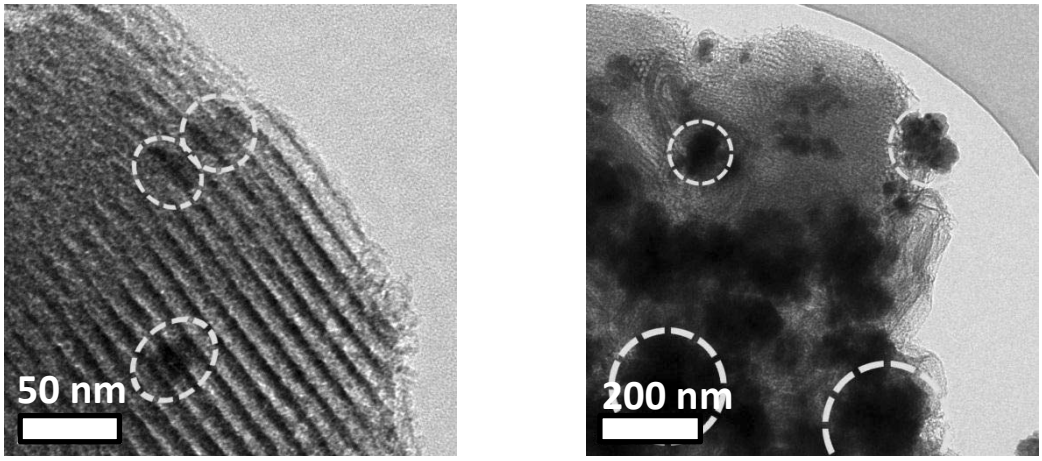

Figure 41: (Left) TEM images of SBA-15 loaded by hydrothermal synthesis (100°C, 5 days) of the sulfide. The yellow circles indicate the sulfide in the pores (left), while the darker regions indicate sulfide deposition on the silica support's exterior (right).

C.4 Spent photocatalysts

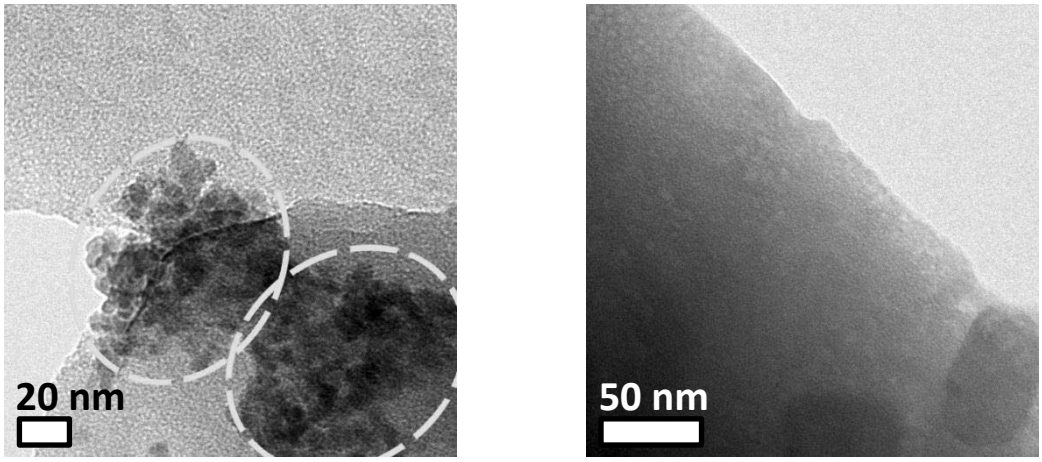

Figure 42: (Left) TEM image of SBA-15 loaded by co-precipitation after photocatalytic testing in a Na_2S (0.25M) and Na_2SO_3 (0.35M) sacrificial solution. Yellow circles indicate the sulfide phase. (Right) TEM image of MCM-41 loaded by co-precipitation after photocatalytic testing in a 10 vol% lactid acid sacrificial solution.

The left TEM image shows the loss of the SBA-15's mesostructure in the basic Na_2S sacrificial solution. Therefore the most active supported sulfide, i.e. MCM-41 loaded by co-precipitation, was dispersed in a 10 vol% lactic acid solution to omit the basic conditions and use an acidic one instead. The mesostructure was still lost during the photocatalytic test and the activity towards the HER also dropped from 5.59 to 1.29 $mmol_{H2} \times g_{cat}^{-1} \times h^{-1}$.

Appendix D: Additional data on $Cd_xZn_{1-x}S$ on titania supports

D.1 Nitrogen physisorption data of loaded titania supports

Support	Loading procedure	Loading fraction (wt %)	Mean $Ø_{pore}$ (nm)	V_{BJH} (cm^3/g)	S_{BET} (m^2/g)
Mesoporous beads	Hydrot.	50	20.8	0.159	50.6
	IWI Hydrot.	25	20.8	0.245	74.0
	IWI H_2S	25	19.8	0.187	72.2
Degussa P25	Hydrot.	50	/	0.118	35.5
	IWI Hydrot.	25	/	0.129	39.1
	IWI H_2S	25	/	0.130	47.5

Table 7: Physisorption data of loaded titania supports. Mean pore diameters are determined based on pore size distribution, pore volume was determined by the Barret-Joyner-Halenda (BJH) method and surface area was determined by the Brunauer-Emmet-Teller (BET) method. The adsorption branch was used for all values.

D.2 Additional TEM image

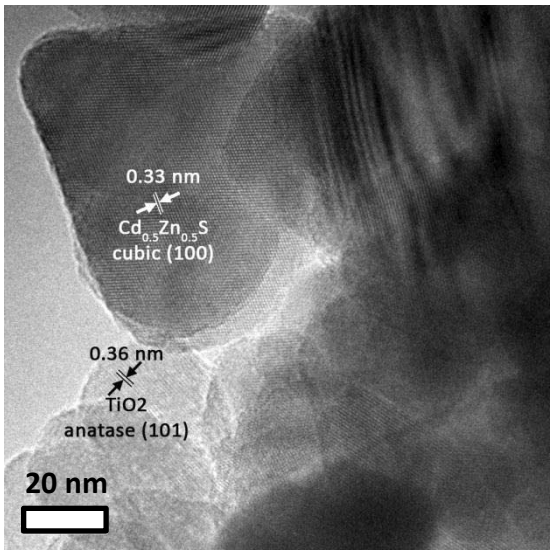

Figure 43: TEM image of hydrothermally deposited sulfide on the mesoporous beads support.

Appendix E: Raspberry SiO_2

During the course of this project, an additional silica support was synthesized but not loaded due to the lacking activity of its SBA-15/MCM-41 counterpart. The synthesis of a macroporous hollow silica was conducted to address the possible mass transfer limitation of the mesoporous SBA-15 and MCM-41. This macroporous hollow silica, further referred to as raspberry silica (SiO_2) due to its distinct shape, yielded very well defined nanostructured particles and is therefore given in the appendix.

E.1 Synthesis of the Raspberry SiO_2

Synthesis of raspberry silica was done in two steps according to procedures published in literature.[131] First a polystyrene template was synthesized. These templates were then used to prepare the silica support. Through an emulsion polymerisation, PVP-modified PS beads were prepared. Ethanol (22.5 g), styrene (5 g), polyvinylpyrrolidone (1.5 g; PVP), 4,4'-Azobis(4-cyanovaleric acid) (0.2 g; ABCVA) and demineralized water (5 g) were mixed under magnetic stirring in a three-necked flask. Oxygen was removed from the solution with N_2 bubbling for 30 minutes at room temperature. Subsequently the solution was heated to 70 °C and kept for 90 minutes in an oil bath under refluxing conditions. Then extra styrene (5 g) and ethanol (22.5 g) was added to the solution and stirred for 6 extra hours. The PS template beads were separated by centrifugation, and washed three times with ethanol. A PS bead stock dispersion was then prepared by dispersing the template in 175 ml of ethanol. Subsequently raspberry silica was prepared by transferring PS stock dispersion (10 ml), ethanol (30 ml), water (3 ml), and TEOS (1 ml) into a Teflon beaker while stirring. The dispersion was heated to 50 °C and 25% NH_3 solution (2.5 ml) was added quickly. The reaction was allowed for 25 minutes before termination. Again the SiO_2/PS particles were separated by centrifugation, washed three times with deionized water, once with ethanol and dried overnight in a vacuumed desiccator. The PS template was removed by calcination at 600 °C for 6 hours under He/O_2 flow. The powder was heated to 270 °C (5 °C/min) and kept for 2 hours. Then it was heated further to 600 °C (5 °C/min) and kept for 6 hours.

E.2 Characterization of the Raspberry SiO_2

E.2.1 SEM results of the PS template beads

Two batches of PS template beads were prepared to synthesize raspberry SiO_2. The second synthesized batch (now denoted as PS_2) seemed to be much more colloidally stable in ethanol in comparison to the first one (now denoted as PS_1). To verify whether the difference originated from the particle size, we carried out a rough particle size analysis based on the SEM images. Care has to be taken to these results as they were obtained from one single image each. For the first batch 223 particles were analyzed. For the second batch 402 were analyzed. We found that both distributions were quite monodisperse but the second synthesis yielded larger PS template beads. The first batch yields a smaller absolute standard deviation but both syntheses have a relative standard deviation of approx. 20%. Usually smaller particles form more stable dispersions due to the smaller influence of the gravity. This leads us to the conclusion that the difference in colloidal stability does not originate from a difference in particle size but rather from a more hydrophilic surface of the PS template beads in the second batch.

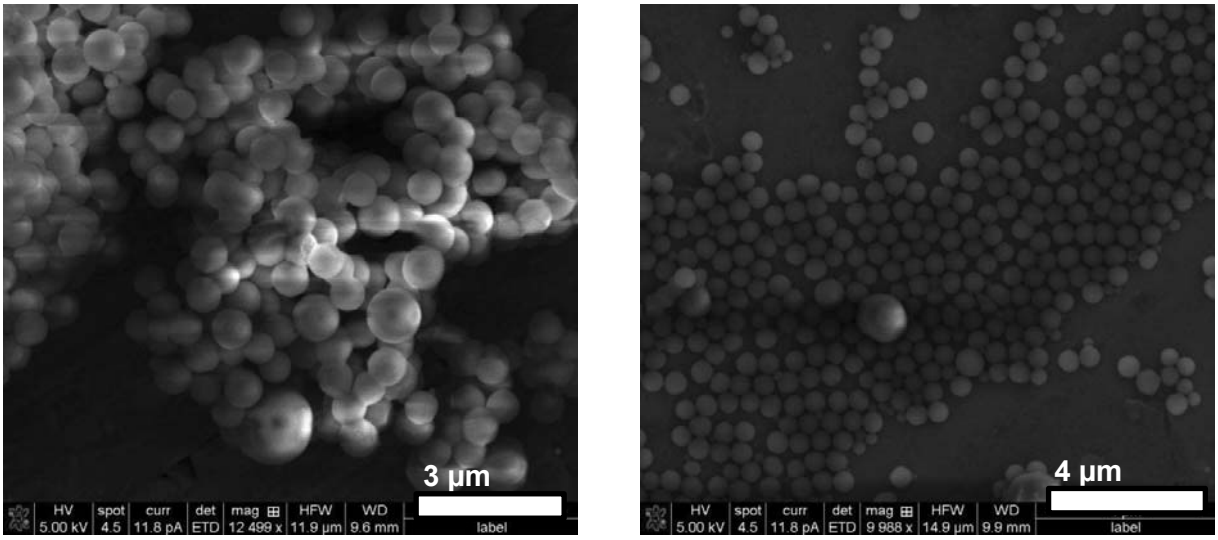

Figure 44: SEM images of (left) PS1 template beads and (right) PS2 template beads.

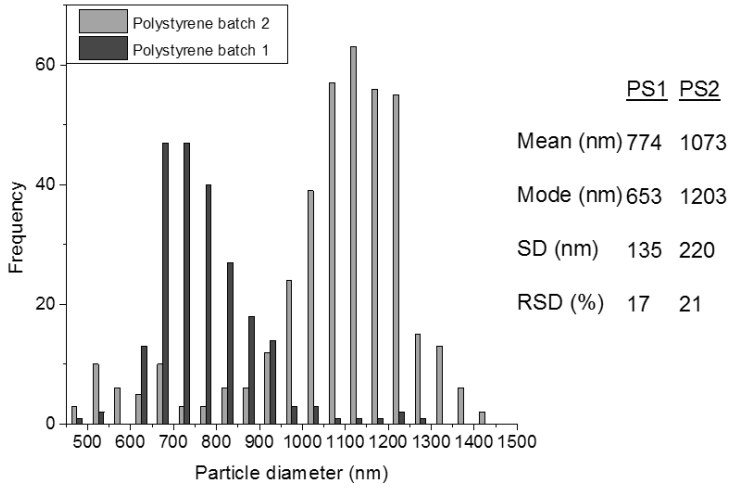

Figure 45: Particle size distribution of PS_1 (blue) and PS_2 (orange). In total 220 PS_1 beads and 403 PS_2 beads were counted.

E.2.2 TEM results

TEM images were taken to confirm the formation of the raspberry SiO_2. Before removal of the PS template we could clearly see the presence of the spherical beads and the silica nanoparticles on its surface. This confirms the success of the template to direct the nucleation and crystal growth. The synthesis parameters (time, temperature, concentration) were carefully chosen to obtain macroporous hollow silica as complete coverage of the PS beads would result in the loss of the interior surface.[131] Hollow macroporous silica was then obtained by calcination. TEM images indicated successful removal of the template as the contrast between the outer and inner sphere increased substantially. We can clearly see that the Raspberry particles were stable and did not collapse after calcination. Interconnection of individual silica particles edges maintained the overall nanostructure as a whole. The macroporosity originates from the space between the individual nanoparticles and incompletely formed shells.

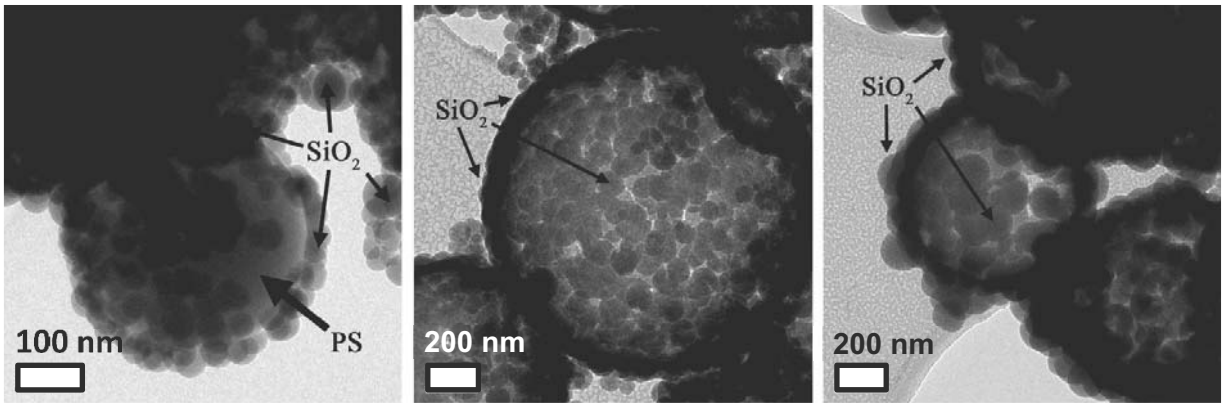

Figure 46: TEM images of (left) Raspberry SiO_2/PS_1, (middle) Raspberry SiO_2/PS_1/CALC (right) Raspberry SiO_2/PS_2/CALC.

E.2.3 N_2 physisorption results

Sample	Template removal	$Ø_{mean}$ (nm)	V_{BJH} (cm^3/g)	S_{BET} (m^2/g)
Raspberry-SIO_2/PS_2	/	/	0.004	8
Raspberry- SiO_2/PS_1	Calcination	/	0.06	65
		/	0.13	86
Raspberry- SiO_2/PS_2	Calcination	/	0.04	41

Table 8: Nitrogen physisorption results of uncalcined Raspberry (Raspberry-SiO_2/PS_2 by the second PS template batch), and calcined Raspberry SiO_2 by the first or second batch of PS template. Multiple rows indicate multiple batches.

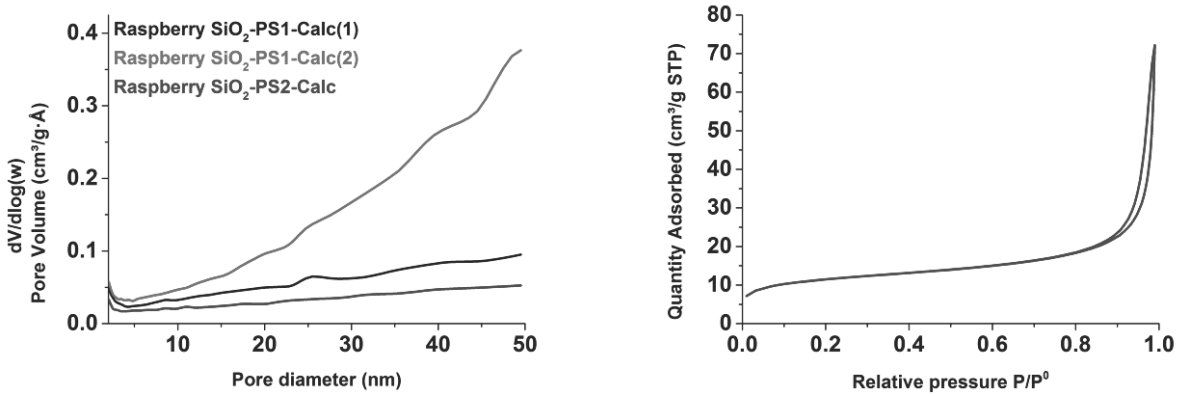

Figure 47: Nitrogen physisorption data of Raspberry SiO_2 supports. (left) Pore size distributions of two RASP SiO_2-PS_1-CALC batches and one RASP SiO_2-PS_2-CALC batch. (right) Adsorption isotherm of RASP SiO_2-PS_2-CALC showing a type II isotherm.

As can be seen from the TEM results, the raspberry SiO_2 primarily displays macropores that cannot be determined by nitrogen physisorption. The surface analysis does reveal that the uncalcined Raspberry-SIO_2/PS_2 sample indeed shows a lower pore volume and surface area than its calcined counterpart
(i.e. Raspberry- SiO_2/PS_2/CALC). This is in good correspondence with TEM results as it indicates removal of the PS template beads and allows N_2 adsorption on the raspberry SiO_2 particle's interior. All three calcined supports show a gradual increase of pore sizes toward the 50 nm border of the

mesopore range highlighting the macroporous nature of this support. The adsorption isotherm can be identified as type II. A typical isotherm for macroporous or non-porous materials with a high adsorption energy (as silica).[104] A small hysteresis loop can be seen at relative pressures P/P^0>0.85, indicative of capillary condensation in the small amount of mesopores present.

Acknowledgements

First and foremost, I want to thank Anton Litke for his patience and efforts to help and guide me through this research. Through the past year I have learned a great lot and became more confident thanks to his determined attitude towards teaching me. His guidance was not limited by theoretical and practical skills but he pointed out moments to be brushed up in my written communication. Besides that I gained some information not related to the research during late evening discussions, resulting in even later home-arrivals. Even though it was not always easy and pleasant, sometimes even very frustrating, I am thankful for the time and effort that he has invested in me. I would like to thank Dr. rer. nat. Jan Philipp Hofmann for the initial research proposal and his guidance throughout the project and the help at difficult crossroads of this research. And last but not the least appreciation goes to Prof. dr. ir. Emiel J.M. Hensen for offering me the opportunity to join his diverse group and the interesting discussions we had.

Furthermore, I would like to thank William van der Graaff for the help with the first nitrogen physisorption measurements. I also thank Adelheid Elemans-Mehring for the help with the first XRD measurements and ICP-AES analysis. I also want to express my gratitude towards Andrey Goryachev for the thorough discussions of the XPS data processing and fitting models, a technique that was very new to me. And at last I also want to thank Stefan Meskers for being a committee member of my Master thesis' defense.

Of course I will never forget the fun times I had with the IMC-student group, or shall I say the "*Come on, what is this OMG, hmm I don't care but fair enough*"? Thank you Ceylan for keeping me very updated of your life on the social media, leading to some funny situations. Than you Federica for the Italian touch, and of course for the spaghetti carbonara! And my big gratitude to Wilbert for not only being an office mate but also the technical help, "that's what men are for ?!?", with Endnote, Mathtype, TU/e bureaucracy and other stuff.

And lastly I want to thank all the other group members for the very fun time I had during my stay, not only in the lab but outside of it as well (e.g. Pasen, Sinterklaas and Christmas parties).